Stony Brook University

Phase separation and neighboring ground states of superconductivity in $K_xFe_{2-y}Se_2$

A Dissertation Presented

by

Hyejin Ryu

to

The Graduate School

in Partial Fulfillment of the Requirements

for the Degree of

Doctor of Philosophy

in

Physics

Stony Brook University

December 2014

Stony Brook University

The Graduate School

Hyejin Ryu

We, the dissertation committee for the above candidate for the

Doctor of Philosophy degree, hereby recommend

acceptance of this dissertation.

Cedomir Petrovic - Dissertation Advisor
Adjunct Professor, Department of Physics and Astronomy

Peter Stephens - Chairperson of Defense
Professor, Department of Physics and Astronomy

Jacobus Verbaarschot - Committee Member
Professor, Department of Physics and Astronomy

Syed Khalid - External Committee Member
Scientist, Brookhaven National Laboratory

This dissertation is accepted by the Graduate School.

Charles Taber
Dean of the Graduate School.

Abstract of the Dissertation

Phase separation and neighboring ground states of superconductivity in $K_xFe_{2-y}Se_2$

by

Hyejin Ryu

Doctor of Philosophy

in

Physics

Stony Brook University

2014

Iron-based superconductor $K_xFe_{2-y}Se_2$ has generated considerable attention having higher critical temperature ($\sim$ 31 K) [1] than previously reported FeSe series ($\sim$ 8 K) and showing a unique real space phase separation with Fe vacancy order. We investigate the effect of the chemical substitution and report various insulating ground states, for example superconductor-insulator transition (SIT) in high-magnetic field by substitution of Na on $K_xFe_{2-y}Se_2$ and magnetic spin glass by substituting Ni or Ag and Te on $K_xFe_{2-y}Se_2$.

The normal state in-plane resistivity below T_c and the upper critical field $\mu_0 H_{c2}$(T) for $K_{0.50}Na_{0.24}Fe_{2-y}Se_2$ are measured by sup-

pressing superconductivity in pulsed magnetic fields. The normal-state resistivity ρ_{ab} is found to increase logarithmically as $T/T_c \rightarrow 0$ with decreasing temperature similar to granular superconductors and Cu-based high-T_c superconductors. Our results suggest that SIT may be induced by the granularity in inhomogeneous superconductors, which is related to the intrinsic real space phase separation. We also present a ground state change of $K_xFe_{2-\delta-y}Ni_ySe_2$ ($0.06 \leq y \leq 1.44$) single crystal compound. Small amount of Ni ($\sim 4\%$) substitution suppresses superconductivity below 1.8 K and for higher Ni content insulating spin glass magnetic ground state is induced. Also, $K_{1.03(3)}Fe_{1.05(4)}Ag_{0.88(5)}Te_{2.00(4)}$ single crystal shows insulating spin glass behavior.

Contents

List of Figures

List of Tables

Chapter 1

Introduction

Since the discovery of the first superconductor, mercury, with superconducting transition temperature (T_c) 4.2 K in 1911 by Heike Kamerlingh Onnes [13], superconductivity is one of the most active studied area in condensed matter physics. Nowadays, a variety of elements, intermetallic compounds, alloys, and oxides show superconductivity with their maximum T_c = 138 K at ambient pressure. Some of the superconductors are already used not only in scientific instruments but also in our daily life such as superconducting quantum interference device (SQUID), nuclear magnetic resonance (NMR), magnetic levitation vehicles, and magnetic resonance imaging (MRI).

Hundreds of superconductors are discovered so far, and some of the significant discovery of superconductors with their T_c and the discovered year are shown on Fig. 1.1. Soon after the first discovery of mercury, lead was found to be a superconductor at 7 K in 1931, and niobium increased its superconducting T_c up to 9.5 K, the highest superconducting transition temperature among the elements superconductors. In 1941, niobium nitride was found to a superconducting compound with T_c = 16 K followed by the discoveries of Nb_3Sn and Nb_3Ge which increased superconducting transition temperature up

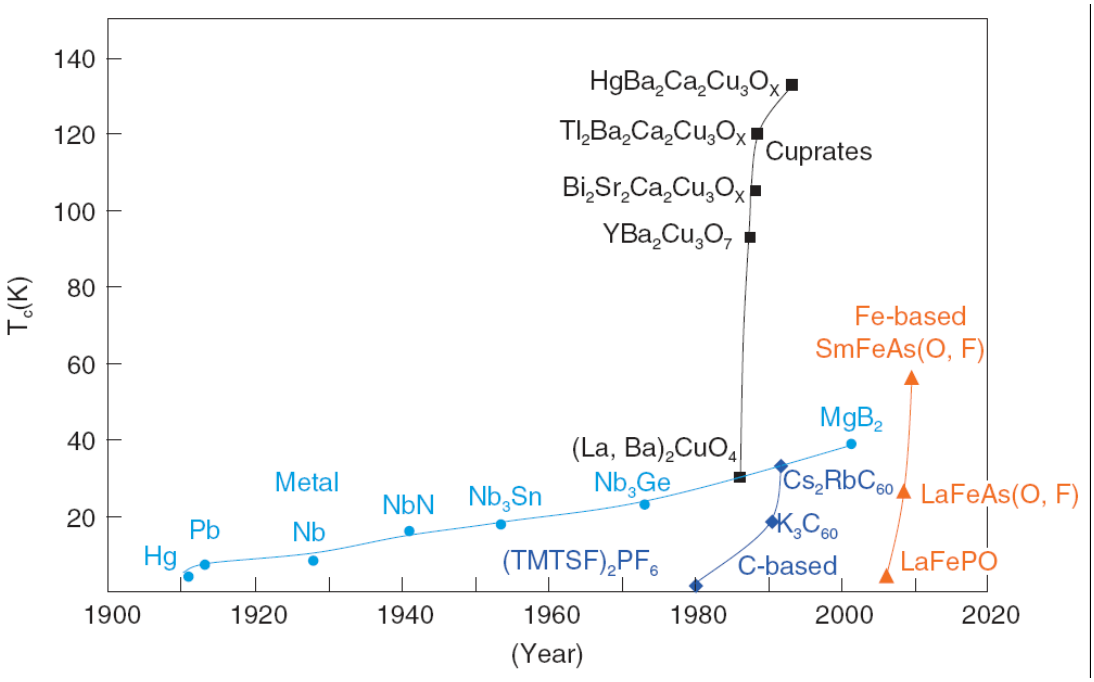

Figure 1.1: Discovery years and T_c of superconductors [2].

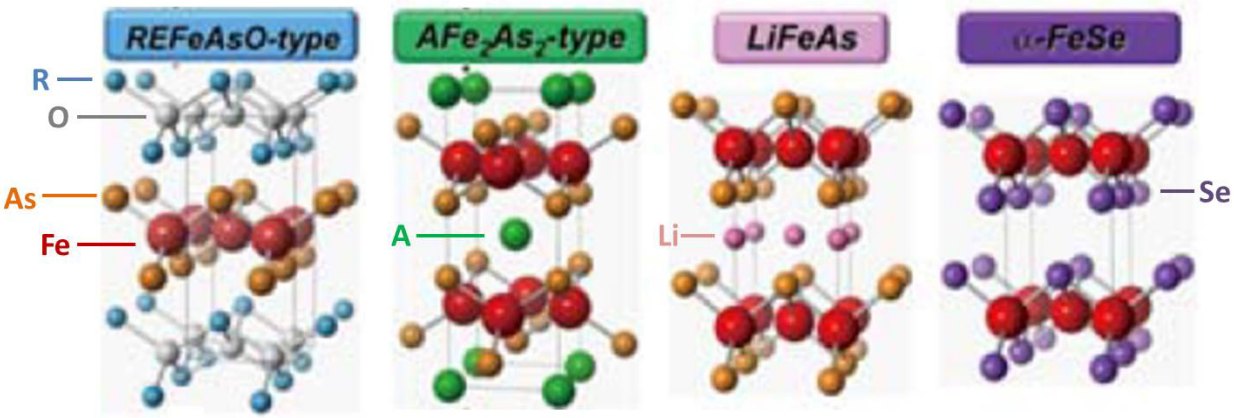

Figure 1.2: Crystallographic structures of the iron-based superconductors [3].

to 23 K.

Until 1986, physicists believed superconductivity with critical temperature above 30 K is impossible by BCS theory which describes superconductivity as a phonon-mediated condensation of Cooper pairs into a boson-like state [14]. However, this thought proved to be wrong by the discovery of barium-doped compound of lanthanum and cooper oxide, $(La_{1-x}Ba_x)CuO_4$, with T_c around 35 K by J. G. Bednorz and K. A. Müllers [15]. This discovery is the new start of high T_c superconductors. Nine month later, it was found by M. K. Wu and their collaborators that replacement of lanthanum with yttrium, $YBa_2Cu_3O_{7-\delta}$ increases T_c drastically up to 92 K [16]. This discovery is particulary significant since the critical temperature exceeds the boiling temperature of liquid nitrogen which allows the use of liquid nitrogen as a refrigerant, replacing liquid helium. This is of significant importance for the application since the liquid nitrogen can be produced inexpensively when compared to liquid helium. In 1988, superconducting T_c rose a bit more by discovery of bismuth

strontium calcium cooper oxide, $Bi_2Sr_2Ca_nCu_{n+1}O_{2n+6-\delta}$, with T_c around 95 K with $n = 1$ and 105 K with $n = 2$ [17]. In the same year, thallium barium calcium copper oxide, $Tl_2Ba_2Ca_{n-1}Cu_nO_{2n+4+x}$, was also discovered with T_c around 120 K when $n = 3$ [18]. Five years later, replacing thallium with mercury yields mercury barium calcium copper oxide, $HgBa_2Ca_{n-1}Cu_nO_{2n+2+\delta}$, which show T_c up to 133 K with n=3 [19], and by Tl substitution on Hg sites, T_c increases to 138 K which is the current record of the highest transition temperature at ambient pressure [20]. The highest critical temperature record under pressure is 164 K of $HgBa_2Ca_2Cu_3O_{8+\delta}$ at 31 GPa [21]. All these superconductor containing Cu anions, we call cuprate superconductors.

Cuprates were the only high temperature superconductor until 2008. After the discovery of $LaFeAsO_{1-x}F_x$ with $T_c = 26$ K when x = 0.11 in February 2008 by Y. Kamihara [22], new superconductor family, Fe-based superconductors, was added as another type of high temperature superconductors. $LaFeAsO_{1-x}F_x$ is not the first Fe-based superconductors. For instance, U_6Fe [23] and $Lu_2Fe_3Si_5$ [24] were discovered in the 20th century. However, these compound did not receive much attention due to the relatively low transition temperature which is below 10 K. Since the discovery of $LaFeAsO_{1-x}F_x$, Fe-based superconductor area starts to be actively studied. $LaFeAsO_{1-x}F_x$ shows even higher T_c which is 43 K under pressure of 4 GPa [25]. A month later, T_c increases up to around 56 K by replacing La by rare earth elements such as Ce, Pr, Nd, and Sm [26, 27]. This subset of Fe-based superconductor family is open referred to as the '1111-type' materials according to their chemical formula of the parent compounds.

In the same year of the discovery of 1111-type superconductors, 2008, an-

other subset of Fe-based superconductor 122-type family, $Ba_{1-x}K_xFe_2As_2$ with $T_c = 38$ K [28], and 111-type family, LiFeAs with $T_c = 18$ K were discovered [29]. By the various substitution of alkali metals and alkaline earth metals, T_c varies such as 32 K for $Sr_{0.6}K_{0.4}Fe_2As_2$ [30], 21 K for $Ca_{0.6}Na_{0.4}Fe_2As_2$ [30], and 26 K for $Sr_{0.6}Na_{0.4}Fe_2As_2$ [31]. Also, the 11-type superconductors were found such as FeSe which has $T_c = 8$ K at ambient pressure [32] and around 37 K under 8.9 GPa [33]. This family has the simplest structure among the Fe-based superconductor families and it consists stacked iron-chalcogenide tetrahedra layers. Locally, the Fe cations form $FeAs_4$-type tetrahedral structure with Se. Several different transition temperature were obtained by different Te and S substitution on Se sites, such as $Fe_{1.13}Te_{0.85}S_{0.1}$ with $T_c = 2$ K [34], $FeTe_{0.8}S_{0.2}$ with $T_c = 10$ K [35], and $FeTe_{0.5}Se_{0.5}$ with $T_c = 14$ K [36].

In 2010, J. Guo reports the discovery of $K_{0.8}Fe_2Se_2$ superconductor with T_c around 31 K which started the field of alkali metal iron selenides. The crystal structure of the $K_{0.8}Fe_2Se_2$ is shown in the inset of Fig. 1.3 (a). It has layers of K^+ ions which separate the FeSe tetrahedra layers by intercalation. Similar to other 122 structure, the FeSe tetrahera layers are the 'conducting layer' and K^+ ions provide charge carriers. Compared to FeSe, for $K_{0.8}Fe_2Se_2$, c axis lattice parameter is significantly increased while a axis lattice parameter is slightly increased which leads to the reduced dimensionality in $K_{0.8}Fe_2Se_2$. The x-ray diffraction pattern of $(00l)$ direction shown on Fig. 1.3 (b) suggests that the cleaved surface of platelike crystal is perpendicular to the crystallographic c axis.

The temperature dependence of in-plane resistance of $K_{0.8}Fe_2Se_2$ clearly shows superconductivity, shown in Fig. 1.4 (a). As temperature cools down,

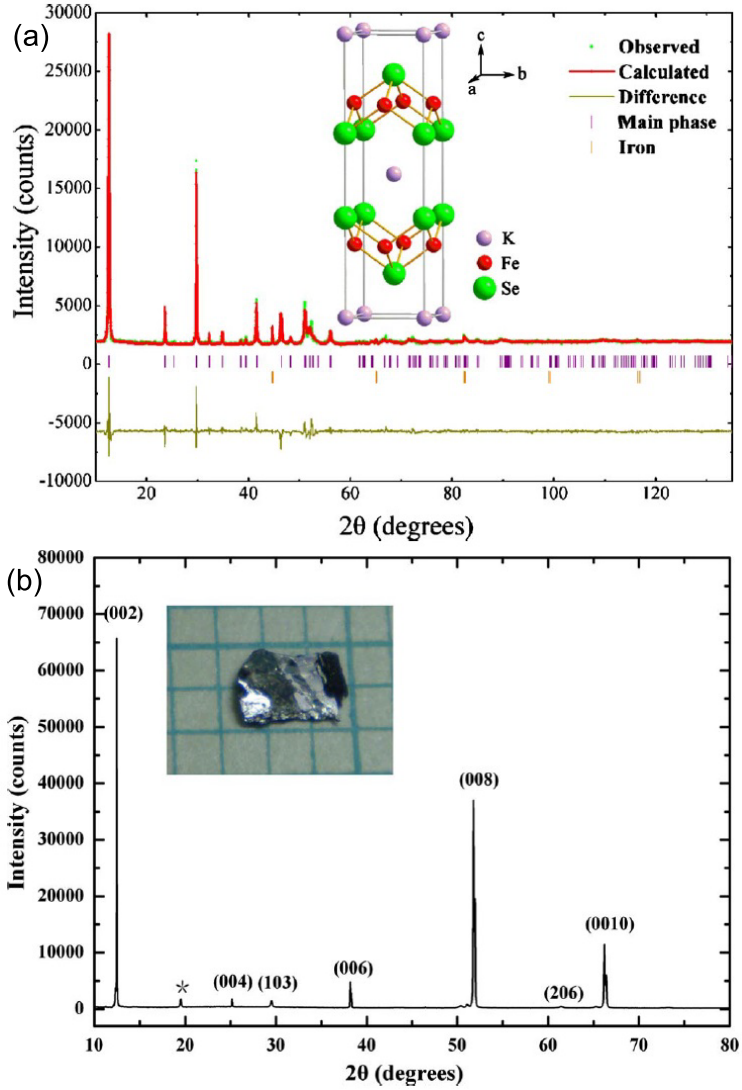

Figure 1.3: (a) Powder x-ray diffraction and Ritveld refinement of KFe_2Se_2. The inset shows schematic crystal structure. (b) The x-ray diffraction pattern of $K_{0.8}Fe_2Se_2$ crystal along $(00l)$ direction. The asterisk shows an unknown reflection. Inset show the photography of $K_{0.8}Fe_2Se_2$ crystal with length scale 1 mm [1].

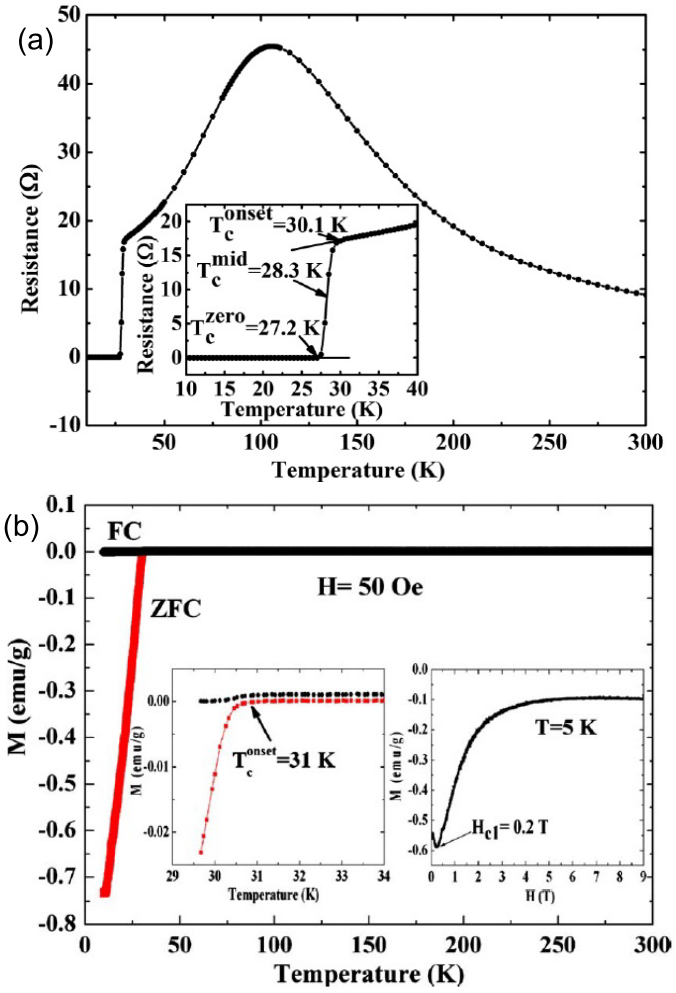

Figure 1.4: (a) Temperature dependence of the electrical resistance for the $K_{0.8}Fe_2Se_2$ crystal with inset containing magnification of the superconducting transition temperature region. (b) The temperature dependence magnetization of $K_{0.8}Fe_2Se_2$ compound for H$\|$c direction at H = 50 Oe. The left inset is the magnification around onset of the superconducting transition region. The right inset shows magnetic field dependence magnetization at 5 K [1].

increasing resistivity is observed followed by a broad hump around 100 K where a metallic behavior starts to show. As temperature is further decreased, the resistance drops at around 30 K which indicates superconducting transition. Above the onset transition temperature, the Zero-field cooled (ZFC) and field cooled (FC) magnetization curves are flat and temperature independent showing typical Pauli paramagnetic behavior of the sample. As shown on the left inset, clear diamagnetic signal appears around 30 K, indicating superconducting transition. This result is consistent with the resistance result discussed above. Right inset shows magnetic field dependence magnetization denoting a typical type-II superconductor behavior. Possible reasons of high superconducting critical temperature value of $K_{0.8}Fe_2Se_2$ when compared to FeSe (8 K) or Te-doped FeSe ($\sim$ 15 K), included the Fe-Se-Fe bond angle which is similar to the $FeSe_4$ tetrahedral shape and the large interlayer distance when compared to FeSe [1].

There are several prominent characteristics on this $K_{0.8}Fe_2Se_2$ compound such as absence of hole pocket which is supposed to be necessary for the theoretical picture of S$\pm$ pairing [37, 38] and the normal state resistivity showing a broad resistivity peak in the temperature around 200 K which moves to a different temperature depending on post annealing or applied pressure [39]. One of the prominent feature of this material is phase separation. It was reported that $K_{0.8}Fe_2Se_2$ compound has Fe vacancies and might be separated into an insulating antiferromagnetic $K_2Fe_4Se_5$ phase and a semiconducting and superconducting KFe_2Se_2. Fig. 1.5 shows the expected iron vacancy order for (a) KFe_2Se_2 and (b) $K_2Fe_4Se_5$. For the case of $K_2Fe_4Se_5$ with its $\sqrt{5} \times \sqrt{5}$ iron vacancy distribution, all Fe atoms have three Fe neighbors and Fe vacancies

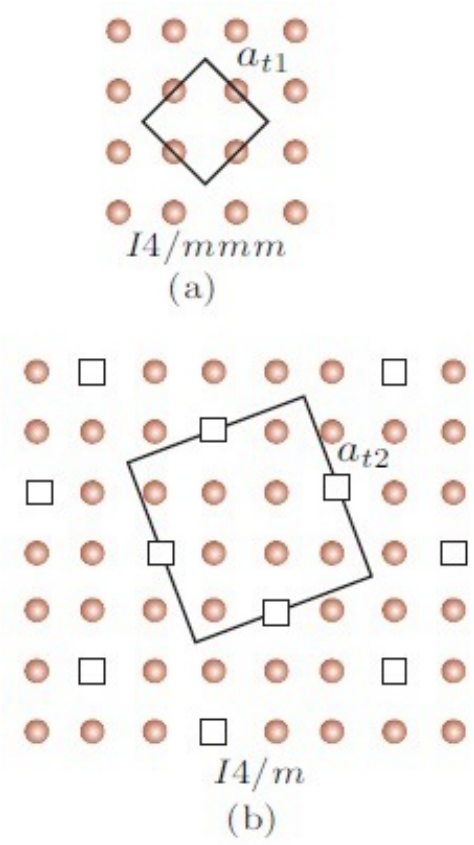

Figure 1.5: Iron atoms and vacancies order of (a) KFe_2Se_2 and (b) $K_2Fe_4Se_5$. The closed circles are Fe atoms and open squares are the Fe vacancies. The solid line marks the unit cell. [4].

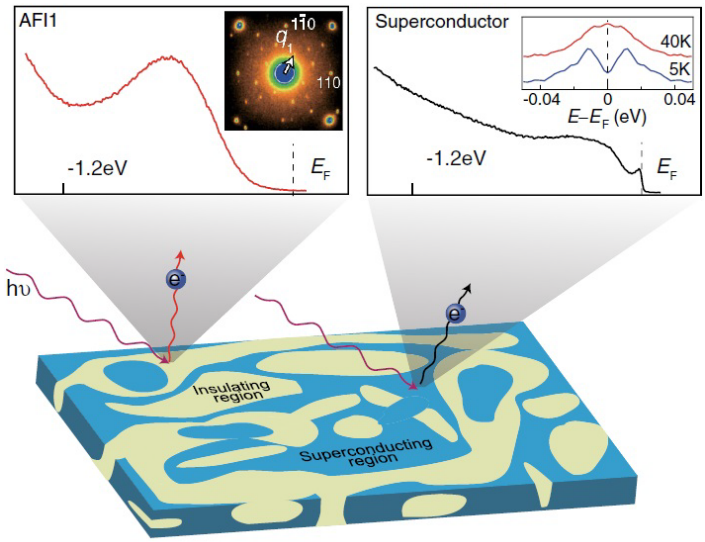

Figure 1.6: Cartoon of the phase separation in superconducting $K_xFe_{2-y}Se_2$ by the photoemission and TEM measurements. The photoemission data are shown on upper inset which consists of two regions, $\sqrt{5} \times \sqrt{5}$ vacancy order is shown in the left region while the density of state of a superconductor is shown in the right region [5].

have four nearest neighbor Fe vacancies with distance $\sqrt{5}$ of unit cell. It was suggested that arrangement of Fe vacancies on the lattice is important for high T_c superconductivity by modifying the Fermi Surface and altering the balance between competing tendencies [4].

Several evidences for the coexisting superconducting and antiferromagnetism and phase separation are reported. Resistivity and magnetic susceptibility studies on $A_xFe_{2-y}Se_2$ (A = Rb, K) reports the coexistence of superconductivity and antiferromagnetism [40]. It was also observed by muon-spin spectroscopy on $Cs_{0.8}(FeSe_{0.98})_2$ and $A_xFe_{2-y}Se_2$ (A = Rb, K) [41, 42]. Simultaneously, angle-resolved photoemission spectroscopy (ARPES) and muon-spin rotation (μSR) analysis of $Rb_{0.77}Fe_{1.61}Se_2$ provides additional evidence for

phase separation [43]. These study report macroscopic separation of metallic ($\sim$ 12%) and insulating and magnetic ($\sim$ 88%) phase. The metallic phase is fully stoichiometric $RbFe_2Se_2$ similar to KFe_2Se_2 [44] and the insulating phase is not relevant for the superconductivity. Raman scattering experiments on $A_{0.8}Fe_{1.6}Se_2$ suggest that the phase separation with mutual exclusion between insulating and superconducting states occurs at the micrometer scale [45, 46]. In addition, ARPES results on phase separation is shown on Fig. 1.6. It also suggests that the semiconducting phase without any vacancy is the parent phase that leads to the superconductivity what an increase of electron doping [5]. Transmission electron microscopy (TEM) on $K_{0.8}Fe_xSe_2$ and KFe_xSe_2 proposed the nanoscale physical phase separation between magnetic and superconducting phase, including the formation of stripe patterns at the micrometer scale (Fig. 1.7 (c)) [7]. Scanning electron microscope measurements also support the phase separation opinion by showing the brighter color and rectangular shape of micron size domains embedded in darker color matrix region (Fig. 1.7 (a,b)) [6]. Percolative scenarios due to the weakly coupled superconducting islands were also reported [47, 48]. Until now, despite of the intensive studies on the phase separation issue, it still remains unclear what is the precise composition and the iron vacancies structure of superconducting phase.

In this dissertation, we discuss various properties of $K_xFe_{2-y}Se_2$ compound with several substitutions which can not only dope an electron or hole to the parent compound but also tune the ground state properties. Also, the substitutions have a pressure effect by substituting ions with an isovalent but different atomic radius. We investigated local structure changes by post an-

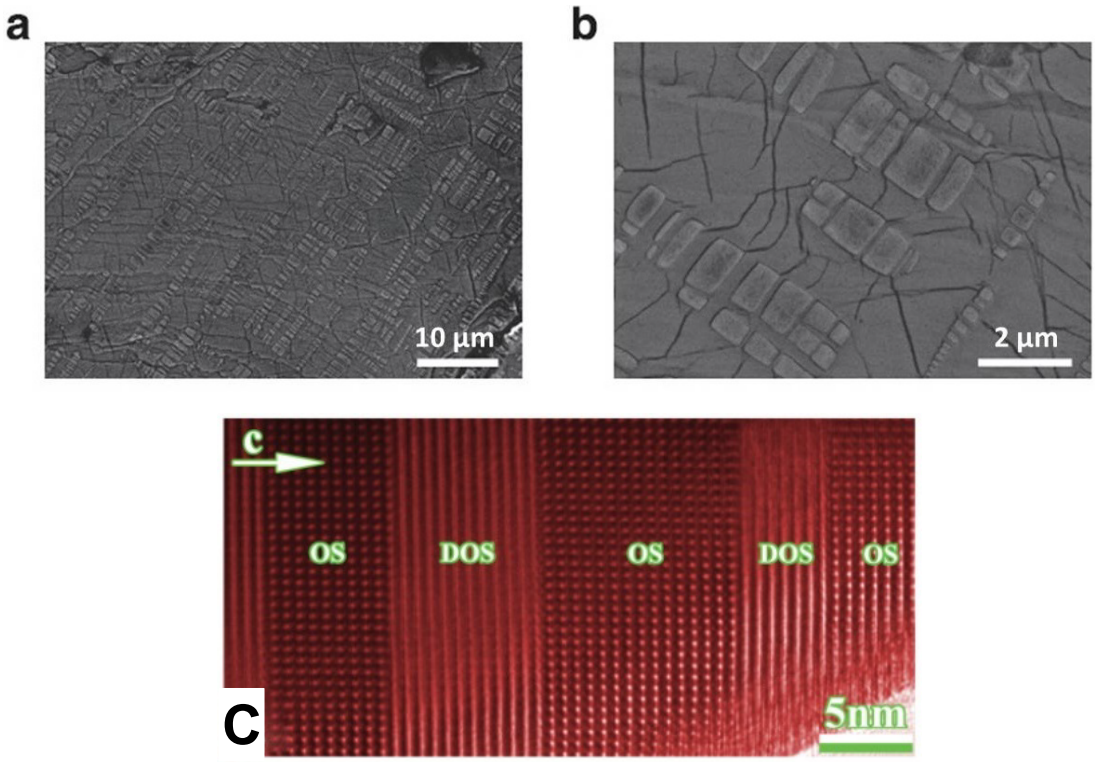

Figure 1.7: (a,b) Back-scattered electron images of SEM measurement of $K_xFe_{2-y}Se_2$. (c) TEM image of $K_xFe_{2-y}Se_2$ showing the phase separation along c-axis direction [6, 7].

nealing and the fast quenching process in the $K_xFe_{2-y}Se_2$ compound. We also observed a superconductor-insulator transition (SIT) in the $K_xFe_{2-y}Se_2$ compound with Na substitution on the K site for the first time. In addition, we report spin-glass behavior of the ground state of $K_xFe_{2-y}Se_2$ compound with Ni substitution on the Fe site and Ag and Te substitution on the Fe and Se site, respectively.

Chapter 2

Overview of superconductivity

2.1 Zero resistivity

One of the basic characteristic of superconductivity is zero resistivity. Heike Kamerlingh Onnes found DC resistivity of mercury dropped to zero at 4.2 K as temperature decreases.[13] Later, this phenomena was named superconductivity where the transition temperature or critical temperature is defined as T_c. Thus, superconducting materials are in normal state above T_c and in superconducting state below T_c.

2.2 Meissner effect

Another basic characteristic of superconductivity is the Meissner effect which is the expulsion of magnetic fields from a superconductor when it is in superconducting state. [49] Zero resistivity is not sufficient to describe the thermodynamic property of superconductivity since a perfect conductor has the same

property. The Meissner effect can distinguish superconductors with perfect conductors.

Two different cooling modes, zero field cooling (ZFC) mode and field cooling (FC) mode, can be used to measure the magnetization. A sample is cooled below T_c in zero external magnetic field for ZFC mode while a sample is cooled down below T_c under non-zero external magnetic field for FC mode. By the Maxwell's equation,

$$\nabla \times \mathbf{E} = -\frac{\partial \mathbf{B}}{c\partial t} \tag{2.1}$$

$$\mathbf{j} = \sigma \mathbf{E}, \tag{2.2}$$

where $\mathbf{E}$ is electric field, $\mathbf{B}$ is magnetic field, $\mathbf{j}$ is current density, c is speed of light, and σ is electrical conductivity. The zero resistivity below T_c, $\mathbf{B}$ should be a constant. For ZFC mode, the superconductor cools down below T_c with no external field, and then external field turns on. The $\mathbf{B}$ field was zero before the external field is on, $\mathbf{B}$ should be also zero after the external field is on due to the zero resistivity and Maxwell's equation which also happens to perfect conductors. For FC mode (Fig. 2.1), an external magnetic field is applied above T_c in which the superconductor is in a normal state. Thus, $\mathbf{B}$ is the non-zero due to non-zero resistivity value, and $\mathbf{B}$ needs to be at a non-zero value after the temperature decreases below T_c due to the zero resistivity and the Maxwell's equation. However, a superconductor shows zero $\mathbf{B}$ for FC mode. Therefore, this expulsion of magnetic field regardless of magnetic field history is the intrinsic property of superconductivity (Meissner effect).

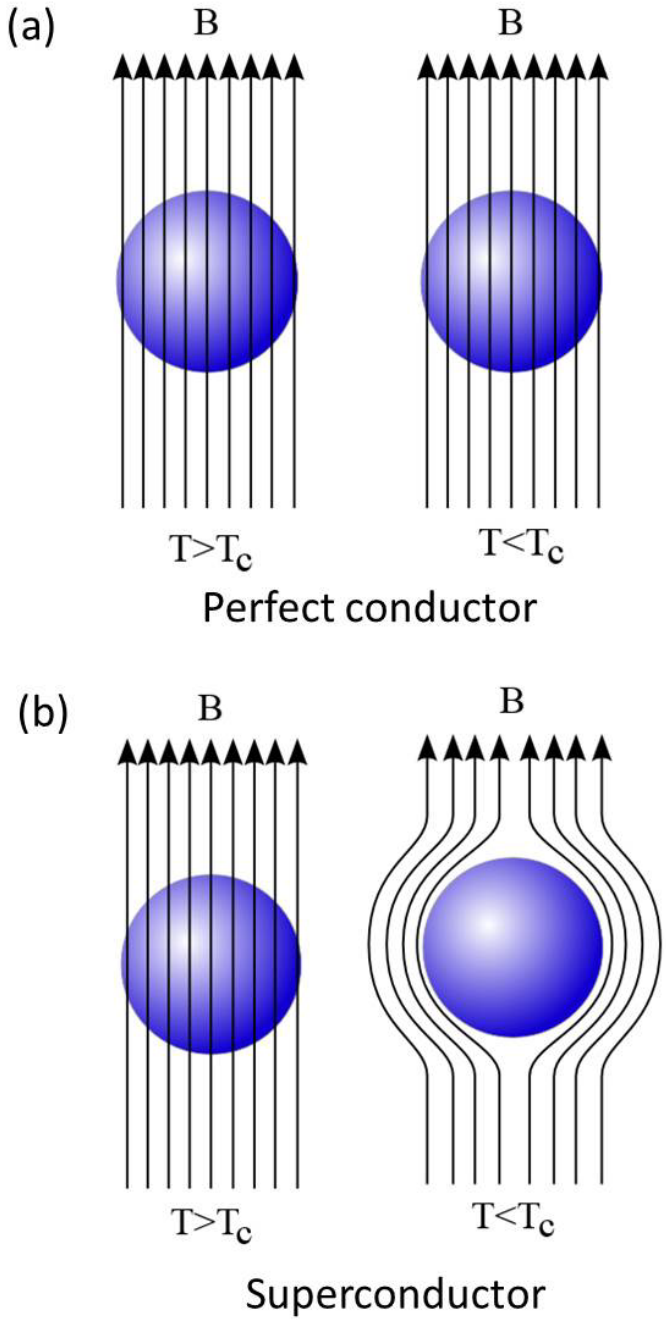

Figure 2.1: A comparision of the response of (a) a perfect conductor and (b) a superconductor to an external magnetic field for field cooling (FC) mode [8].

2.3 Ginzburg-Landau theory

Ginzburg-Landau theory explains superconductivity based on the Landau mean-field description of phase transition [50–52]. In this theory, two assumptions are made. First, the superconducting transition is a second order transition. Second, $\psi(\mathbf{r})$ is used as a superconducting order parameter and is a complex number describes a macroscopic quantum wave function $\psi(\mathbf{r}) = |\psi(\mathbf{r})|e^{i\phi}$.

The free energy of inhomogeneous superconductor in a magnetic field is

$$G_s(H) = G_n + \int dV \left[\frac{\hbar^2}{2m^*} \left| \nabla\psi - i\frac{e^*\mathbf{A}}{\hbar c}\psi \right|^2 + a(T)|\psi|^2 + \frac{b(T)}{2}|\psi|^4 + + \frac{B^2}{8\pi} - \frac{\mathbf{B}\cdot\mathbf{H}}{4\pi} \right] \quad (2.3)$$

where $\mathbf{A}$ is the magnetic vector potential, $\mathbf{B} = \nabla \times \mathbf{A}$ is the magnetic field, and H is the external as magnetic field. In the near T_c region, the parameters a and b can be written by

$$a(T) \approx a_0 \left(\frac{T - T_c}{T_c} \right), \quad b(T) \approx b_0 \quad (2.4)$$

By minimizing the free energy with respect to the order parameter ψ and the vector potential $\mathbf{A}$, information about the superconducting order parameter $\psi(\mathbf{r})$ and superconducting current can be obtained.

From the Ginzburg-Landau equation, two characteristic lengths can be obtained which are the coherence length ξ and the penetration depth λ. The coherence length is a distance over which the order parameter ψ can vary without any significant energy increase, given as

$$\xi = \sqrt{\frac{\hbar^2}{2m^*|a|}} \tag{2.5}$$

The penetration depth is a characteristic distance that the magnetic field can penetrate into the superconductor, given by

$$\lambda = \sqrt{\frac{m^* c^2 b}{4\pi (e^*)^2 |a|}} \tag{2.6}$$

The ratio of coherent length and penetration depth, λ/ξ is defined as the Ginzburg-Landau parameter κ.

Superconductivity is classified as type I superconductor and type II superconductor, by the Ginzburg-Landau parameter κ which determines the interface energy σ between the normal state and superconducting state.

type I superconductor: $K < \frac{1}{\sqrt{2}}$, then $\sigma > 0$

type II superconductor: $K > \frac{1}{\sqrt{2}}$, then $\sigma < 0$

We assume that there is a mixture of the normal domain and the superconducting domain under the external field H. If $\sigma > 0$, a superconducting state only exists in the region of $H < H_c$ while the normal state exists only in the region of $H < H_c$ since the formation of the interface is not energetically favorable. This is a type I superconductor. On the other hand, if $\sigma > 0$, there is a intermediate state between superconducting ($H < H_{c1}$) region and normal ($H < H_{c2}$) region, $H_{c1} < H < H_{c2}$ region which has a normal and a superconducting domain which are parallel to the external field. We call the

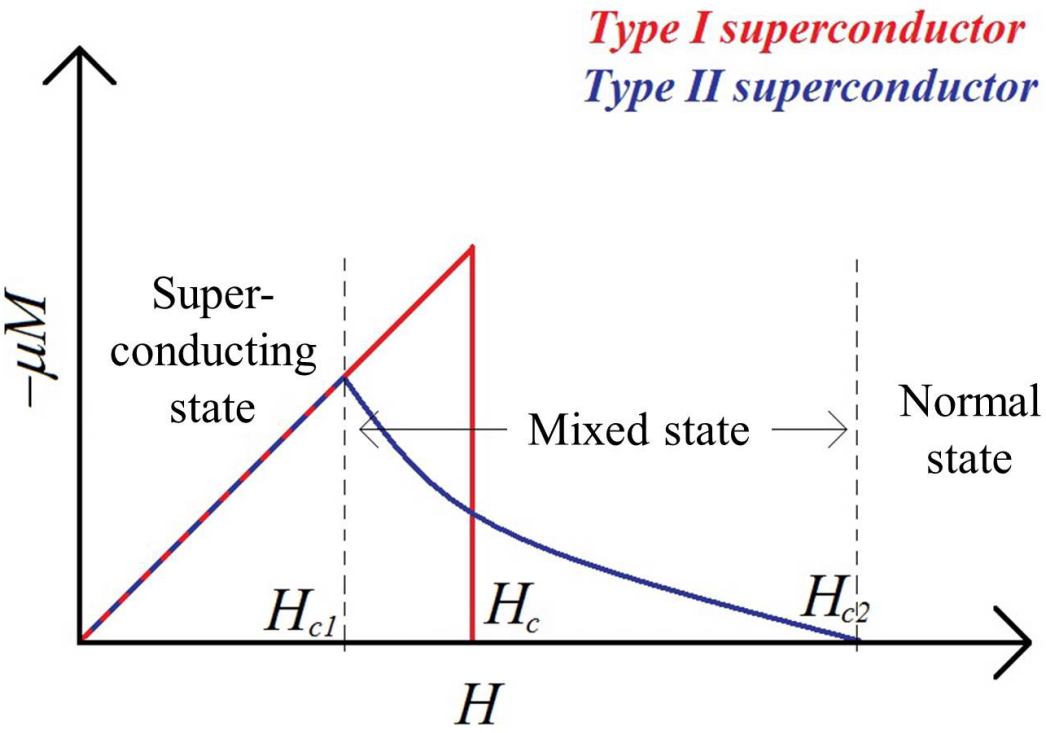

Figure 2.2: Magnetization for type I and type II superconductors [9].

normal domain a vortex which has radius in the order of ξ. As the magnetic field increases, the number of vortices increase and finally there is a transition to the normal state when $H > H_{c2}$.

2.4 BCS theory

BCS theory is the first theory which describes superconductivity as a microscopic effect, since its discovery in 1911. For this theory, several assumptions need to be made such as constant electron-phonon interaction and spherical Fermi surface. In BCS theory, the spherical Fermi surface becomes unstable if there exists an attractive interaction between electrons due to the electron-phonon coupling. The emerging ground state is superconducting consisting of Cooper pairs condensed into a macroscopic phase with broken gauge symmetry.

From the conventional electron-phonon coupling, there is an attractive interaction between the electrons having opposite spins and momentum. Cooper showed that this paring of electrons (Cooper pairs) lowers the total energy showing that the Fermi surface is unstable under the attractive interaction [53]. Since electrons follow Fermi-Dirac statistics, the symmetry of the paring wavefunction is dictated by the symmetry of the spin states if we ignore the spin-orbit coupling. For example for singlet pairing, the gap function has even parity having a total angular momentum $L = 0, 2, 4,$ whereas for spin triplet pairing, the gap function has odd parity with an odd value of angular momentum. The conventional BCS theory, the isotropic (s-wave) spin-singlet paring

is valid for simple metals with weak correlations.

For simplicity we consider a spherical Fermi surface with constant electron-phonon coupling defined as follows: $V_{kk'}$ = -V for $|\varepsilon_k| \leq \hbar\omega_D$, $|\varepsilon_{k'}| \leq \hbar\omega_D$, and $V_{kk'} = 0$ for otherwise, relative kinetic energy (ε_k) of the electron can be defined as

$$\varepsilon_{\mathbf{k}} = \frac{\hbar^2 k^2}{2m} - \frac{\hbar^2 k_F^2}{2m}. \tag{2.7}$$

The mean field solution of the total energy is given by

$$E_s = 2\sum_{\mathbf{k}} \varepsilon_{\mathbf{k}} \nu_{\mathbf{k}}^2 + \sum_{\mathbf{kk'}} V_{\mathbf{kk'}} \nu_{\mathbf{k'}} \mu_{\mathbf{k}} \nu_{\mathbf{k}} \mu_{\mathbf{k'}}, \tag{2.8}$$

where ν_k^2 is the probability that pair state (k, -k) is occupied. By minimizing Gibbs free energy ν_k^2 is obtained

$$\nu_{\mathbf{k}}^2 = \frac{1 - \varepsilon_{\mathbf{k}}/E_{\mathbf{k}}}{2}, \tag{2.9}$$

where

$$E_{\mathbf{k}} = \sqrt{\varepsilon_{\mathbf{k}}^2 + \Delta_0^2}. \tag{2.10}$$

Also,

$$\mu_{\mathbf{k}}^2 = \frac{1 + \varepsilon_{\mathbf{k}}/E_{\mathbf{k}}}{2}. \tag{2.11}$$

Δ_0 is an energy gap, and $2\Delta_0$ is required to break a Cooper pair. The gap become smaller as temperature increases due to more of pair-breaking, and once the temperature reaches to T_c the gap becomes zero. The temperature dependence of the gap can be expressed by the following equation:

$$1 = VD(0) \int_0^{\varepsilon_0} d\varepsilon \frac{\tanh(\sqrt{\varepsilon_{\mathbf{k}}^2 + \Delta^2}/2k_BT)}{\sqrt{\varepsilon_{\mathbf{k}}^2 + \Delta^2}} \tag{2.12}$$

When T = 0 K,

$$\Delta(0) = \frac{\hbar\omega_D}{\sinh(\frac{1}{D(E_F)V})}, \tag{2.13}$$

in the weak coupling limit, $D(E_f)V \leq 1$, $k_BT_c \leq \hbar\omega_D$

$$\Delta(0) \approx 2\hbar\omega_D \exp(-\frac{1}{D(E_F)V}), \tag{2.14}$$

in the strong coupling limit,

$$\Delta(0) \approx \hbar\omega_D D(E_F)V. \tag{2.15}$$

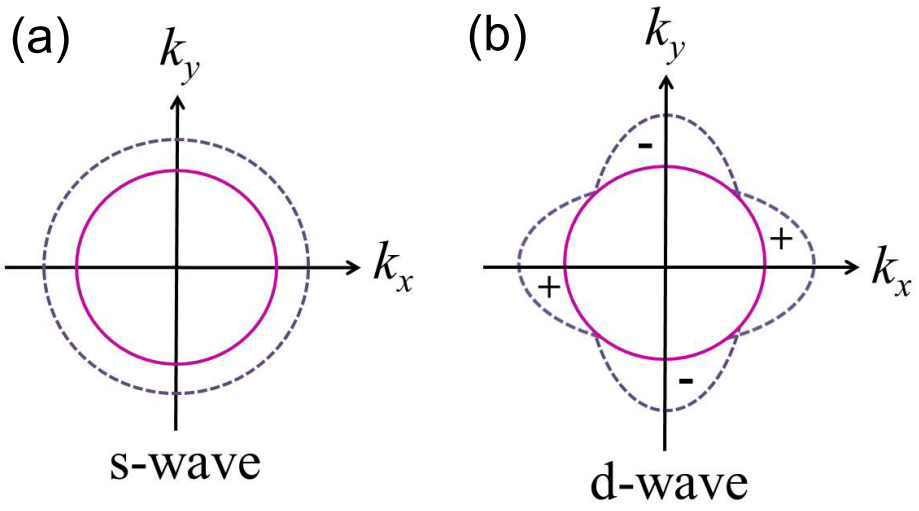

Figure 2.3: Superconducting gap in k space.

In the low temperature weak coupling limit, k_BT $\ll \triangle(0)$,

$$\Delta(T) \approx \Delta(0)\left[1 - \sqrt{2\pi k_B T/\Delta_0}\exp(-\Delta_0/k_B T)\right] \tag{2.16}$$

Also, near T_c in the weak coupling limit,

$$\Delta(T) = 3.06 T_c\sqrt{1 - T/T_c}. \tag{2.17}$$

By measuring superconducting gap, the pairing symmetry can be extracted. Fig. 2.3 (a) shows the isotropic s-wave with S=0 and L=0 which is for the original BCS theory. For 122-type Fe based superconductor S±-wave pairing is proposed in which the superconducting gap is fully gapped on both electron

and hole Fermi sheets with opposite signs [37, 54, 55] Fig. 2.3 (b) shows d-wave gap with L = 2 and S = 0. The cuprate superconductors have d-wave symmetry of the Cooper pair.

Several important thermodynamic properties are described below.

In the weak coupling limits, the ratio of $2\Delta(0)/k_BT_c$ is

$$k_BT_c \approx 1.14\omega_D \exp(-\frac{1}{D(E_F)V}), \quad \frac{2\Delta(0)}{k_BT_c} = 3.53, \tag{2.18}$$

while in the strong coupling limits, the ratio of $2\Delta(0)/k_BT_c$ is

$$k_BT_c \approx \hbar\omega_D D(E_F)V/2, \quad \frac{2\Delta(0)}{k_BT_c} = 4. \tag{2.19}$$

In the weak coupling limit, the discontinuity in specific heat at critical temperature in zero magnetic field can be expressed by

$$\left.\frac{C_s - C_n}{\gamma T}\right|_{T_c} = 1.43, \tag{2.20}$$

where

$$\gamma = \frac{2}{3}\pi^2 k_B^2 D(E_F). \tag{2.21}$$

The critical field in a weak coupling limit is described by

$$\left.\frac{dH_c}{dT}\right|_{T_c} = 4.4\sqrt{\gamma}, \tag{2.22}$$

where

$$C \propto \frac{\Delta(0)^{2.5}}{T^{1.5}} \exp\left(-\frac{\Delta(0)}{k_B T}\right). \tag{2.23}$$

Chapter 3

Experimental methods

In this dissertation, experimental techniques involving single crystal growth, crystal structure analysis, transport, magnetization, thermal and thermodynamic properties measurement at various temperature and magnetic fields were used. Here we describe a detailed procedure of sample preparation and their property measurements.

3.1 Sample preperation

Iron chalcogenide single crystals studied in this dissertation were grown by the self-flux method which is one type of solution growth. The grown crystals are cut and platinum wires were attached for the measurements.

3.1.1 Crystal growth

A single crystal is a material which is consist of only single grain without any grain boundaries. Single crystals are preferred in experiments since they have

less defects associated grain boundaries and impurities. In polycrystal materials, many of the physical properties are complicated due to the effect of grain boundaries. Moreover, single crystals allow to study anisotropic properties due to this property which can be clearly determined from their orientation. Therefore, high quality single crystals are often preferred for both basic science research and industrial applications.

There are several techniques for single crystal growth which can be classified as solid state growth, vapor transport growth, melt growth, and solution growth. The solid state growth mostly generates polycrystal materials which consists of micron size of grains containing phase segregation and grain boundary issues. The vapor transport growth can produce high quality crystals while the size of crystal is small due to the multiple nucleation sites in growth process. The melt growth is also called Czochralski method which is useful to produce large single crystal Si or Ge semiconductors. However, these techniques are only valid for the materials which melt congruently without decomposition at the melting point without any phase transition between melting and room temperature. On the other hand, solution growth allows both congruent and incongruent melting growth. Especially, high temperature solution growth is one of the most popular and widely used method [56, 57].

In this growth, all raw elements with designated ratio are heated in a container to the high soaking temperature in order to dissolve the materials into a uniform liquid. After several hours of soaking, the container is cooled down slowly. During cooling process, the desired compound forms as a crystal, and is separated by decanting off the excess liquid using a centrifuge. The liquid is referred to as a flux which has two different types, self-flux and non-self-flux.

For the self-flux method, the excess of one or more constituent elements of the desired material is used as a solvent while the elements other than the desired materials are used as a solvent for the non-self-flux method. The self-flux method is preferred since there is a less possibility to form extrinsic phases. However, this is possible only in limited cases due to several reasons such as high melting temperatures or vapor pressures. The non-self-flux method uses extrinsic solvents to decrease the melting temperature and to increase the solubility of the starting ingredients.

For the preparation of the $K_xFe_{2-y}Se_2$ single crystal which is used in this dissertation, the self-flux method is used. Prereacted FeSe and K pieces are weighed in the desired nominal ratio, mixed and placed in an alumina crucible which is located in a iron tube. The iron tube is inserted into a quartz tube which has quartz wool at the bottom to protect the quartz tube from cracking due to the different thermal expansion of between the quartz tube and the iron tube. Another inverted alumina crucible covers the bottom crucible and the iron tube is closed by screw top lid. The quartz tube is evacuated and sealed under argon atmosphere. The schematic diagram of the ampoule is shown on Fig. 3.1 (b). The sealed quartz tube is heated up to 1030 $^{\circ}C$ in 6 hours, soaked for 3 hours for complete mixing, and cooled down to 730 °C at a rate of 6 $^{\circ}C$/h. Platelike crystals up to 5×5×1 mm^3 are grown (Fig. 3.1 (a)). The obtained crystal is preserved in a vacuum due to the strong air sensitivity. As-grown $K_xFe_{2-y}Se_2$ single crystal surface shows a shiny golden color which turns to a black color as it oxidizes.

In this dissertation, several chemical substitutions were used to perturb the ground state of the parent compound $K_xFe_{2-y}Se_2$. By doping electron or

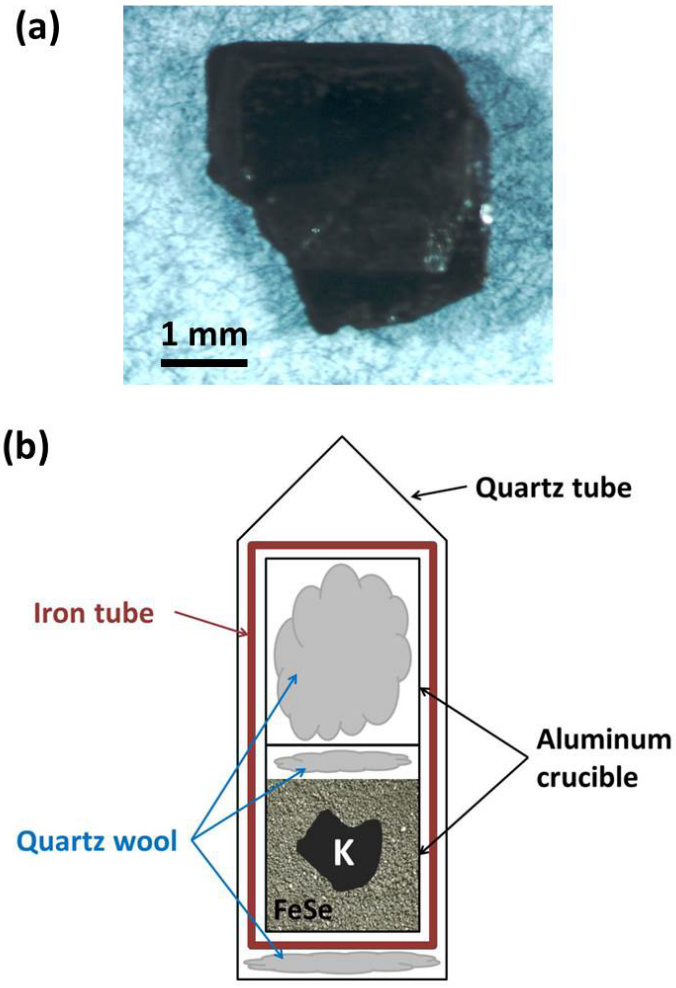

Figure 3.1: (a)As grown $K_xFe_{2-y}Se_2$ single crystal (b) Schematic diagram of the ampoule for $K_xFe_{2-y}Se_2$.

hole, we can cause chemical potential changes. Also, isovalence doping with the atoms having different ionic radius can induce positive or negative pressure to the parent compound.

3.1.2 Structure analysis

After the crystal growth, we need to determine the phase and lattice parameters to check whether the desired phase are formed or not. In this dissertation, X-ray diffraction (XRD) spectra are taken with Cu Ka radiation ($\lambda = 1.5418$ $\mathring{A}$) using a Rigaku Miniflex X-ray machine. Single crystals are ground to fine and homogeneous powder using mortar and pestle. The powder is pasted by a vacuum grease to the quartz disc which will be placed on the sample holder in a XRD machine. The lattice parameters are obtained by fitting the XRD spectra using RIETICA software [58].

Rietica software refines the crystal structure by Rietveld method. In the refinement,

$$S = \sum_i \frac{(y_{ci} - y_{oi})^2}{y_{oi}} \tag{3.1}$$

is minimized until the observed data profile, y_{oi}, is well matched with the calculated profile, y_{ci}. The Bragg reflection at any point i is

$$y_{ci} = y_{bi} + s \sum_K L_K |F_K|^2 \phi(2\theta_i - \theta_K) P_K A \tag{3.2}$$

where, y_{bi} is a background, s is a scale factor, K is a Miller index, $\phi(2\theta_i - \theta_K)$ is a peak shape function such as Gauss, Lorentz, and pseudo-Voigt), P_K is

preferred orientation function, and A is absorption factor.

By minimization, a set of normal equations which include derivatives of all y_{ci} with respect to x_j and soluble by inversion of the normal matrix with elements M_{jk}

$$M_{jk} = -\sum_i 2/y_{0i} \left[(y_{0i} - y_{ci}) \frac{\partial^2 y_{ci}}{\partial x_i \partial x_k} - \left(\frac{\partial y_{ci}}{\partial x_j} \right) \left(\frac{\partial y_{ci}}{\partial x_k} \right) \right] \tag{3.3}$$

Then,

$$\Delta x_k = \sum M_{jk}^{-1} \frac{\partial S}{\partial x_k} \tag{3.4}$$

which will provide an improved fitting model. This procedure will be repeated until the refinement result is stable with no change by repeating the procedure.

3.2 Transport measurement

In this dissertation, electric transport, thermodynamic and thermal measurements were performed by Quantum Design Physical Property Measurement System (PPMS). PPMS-9 which we used in this dissertation can perform the measurement in the temperature region from 1.9 K to 400 K and the magnetic field up to 9 Tesla. The data is recorded by MultiVu software which can conduct variety of measurement such as resistivity, and heat capacity.

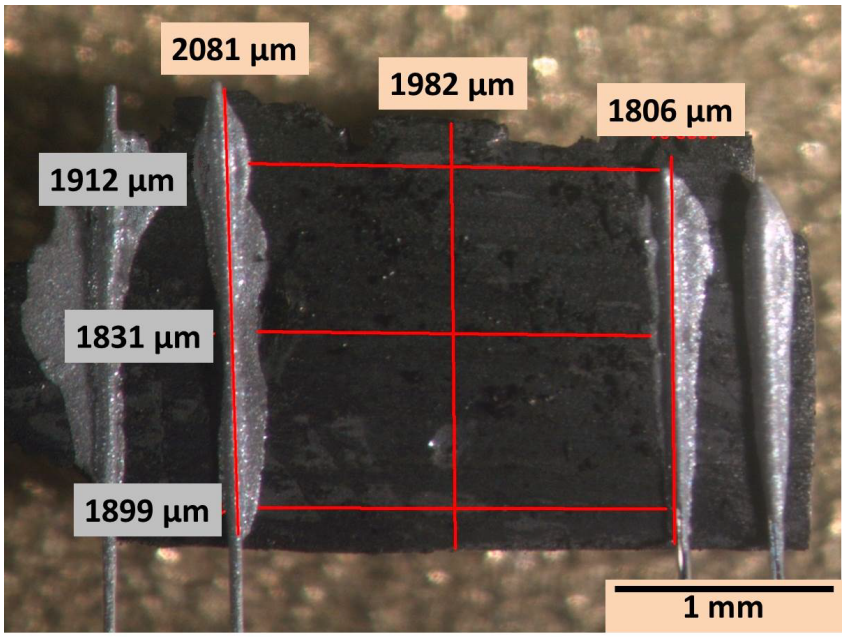

Figure 3.2: $K_xFe_{2-y}Se_2$ sample with four wire contacts.

3.2.1 Resistivity measurement

For the resistivity measurement, a four probe method is used to eliminate the contribution from the contact resistance. Four Pt wires are pasted on the sample surface in parallel using silver paste. The outer two Pt wires are for the current leads while the inner two Pt wires are for the voltage leads. The longer distance of the inner Pt wires gives the larger signal with less noise. The contact resistance is usually around 10 Ω. The geometric factor, A/L, needs to be measured to convert the measured raw data, resistance, into resistivity. A is the cross-sectional area of the sample and L is the distance between the two voltage leads. The geometry is measured by high precision optical microscope with 10 μm resolution (Fig. 3.2).

The resistivity measurement is performed using AC transport (ACT) mode

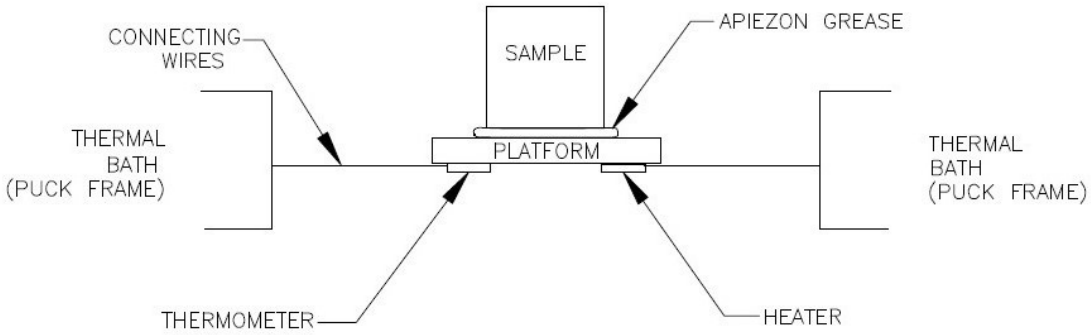

Figure 3.3: Sample platform diagram of PPMS for heat capacity option [10]

in PPMS. This option incorporates a precision current source which has a resolution of 0.02 μA and a maximum current of 2 A and a voltmeter which has similarly sized range. The resistance is measured by measuring the voltage drop across the voltage leads while the known current (0.3 $\sim$ 1 mA with frequency 16 Hz for the measurement performed in the dissertation) is applied through the current leads. In the ACT option, the AC bias current is from 1 Hz to 1 kHz, and this is more sensitive than DC measurement due to the signal filtering ability which can eliminating frequency dependent noise, DC offset, and instrumental drift.

3.2.2 Heat capacity measurement

For the heat capacity measurement, the mass of the sample needs to be around 10 mg with in-plane size of around $2 \times 2\, mm^2$. A platform heater and platform thermometer are attached to the bottom of the sample platform with attached small wires which provide the electrical connection in between and thermal and structural support for the platform. The sample is placed on the platform

with a thin layer of Apiezon grease which is applied for a good contact between sample and the platform (Fig. 3.3).

The PPMS we used in this dissertation measures the heat capacity at constant pressure which can be expressed by the equation,

$$C_p = (\frac{dQ}{dT})_p. \tag{3.5}$$

For the measurement, a known amount of heat is applied at constant power for a fixed time, and then it is followed by a cooling time of the same duration. The temperature change is monitored while the heat is added to and removed from the sample. The analysis is performed using a relaxation technique. Each cycle in which is heating period followed by a cooling period is fitted by the model that accounts for both the thermal relaxation of the sample platform to the bath temperature and the relaxation between the sample platform and the sample itself [59]. Two models can be used for the fitting, a simple model and the two-tau model. The simple model is the following:

$$C_{total}\frac{dT}{dt} = -K_w(T - T_b) + P(t), \tag{3.6}$$

where C_{total} is the total heat capacity of the sample and sample platform, K_W is the thermal conductance of the supporting wires, T_b is the temperature of the thermal bath (puck frame), and $P(t)$ is the power applied by the heater which will be P_0 for heating period and zero for cooling period. This simple model is generally used for addenda measurement and most of the samples. If the contact between the sample and the platform is poor, it produces a temperature difference between them, then the two-tau model is used. The

two-tau model equations are the following.

$$C_{platform}\frac{dT_p}{dt} = P(t) - K_w(T_p(t) - T_b) + K_g(T_s(t) - T_p(t)), \tag{3.7}$$

$$C_{sample}\frac{dT_s}{dt} = -K_g(T_s(t) - T_p(t)), \tag{3.8}$$

where $C_{platform}$ is the heat capacity of the sample platform, C_{sample} is the heat capacity of the sample, and K_g is the thermal conductance between the two due to the grease. $T_p(t)$ and $T_s(t)$ are the respective temperatures of the platform and sample.

3.2.3 Seebeck coefficient measurement

The Seeback effect is the conversion of temperature difference to electricity. The local current density can be expressed by

$$\mathbf{J} = \sigma(-\nabla V + \mathbf{E}_{emf}), \tag{3.9}$$

where V is the local voltage, σ is the local conductivity, and $\mathbf{E}_{emf}$ is the electromotive force which provides a description of Seebeck effect.

$$\mathbf{E}_{emf} = -S\nabla T, \tag{3.10}$$

where S is the Seebeck coefficient and ∇T is the temperature gradient.

The Seebeck coefficient measurement is performed in a PPMS with theramal transport option (TTO). The heat pulse is applied to one end of the sample by applying current through the heater and exit through the cold end

of the sample. The temperatures of hot end and the cold end of the sample are measured at the thermometer shoes. While the heat pulse is applied, the Seebeck voltage ($\Delta V = V_+ - V_-$) is measured. Thus, the temperature dependent of Seebeck coefficient can be extracted. The sample geometry needs to be long and thin like a needle shape to obtain accurate Seebeck coefficient.

3.3 Magnetization measurement

In this dissertation, the magnetization measurement is performed by Quantum Design Magnetic Property Measurement System (MPMS). MPMS XL 5 which we used in this dissertation can measure the temperature from 1.8 K to 400 K and the magnetic field up to 5 Tesla. The data is also recorded by MultiVu software.

The sample needs to be mounted in the center of a straw. The sample is placed in between the inner straw and the outer straw or between two cut inner straws. The one end of the straw which is pointing the bottom is covered by Teflon tape in order to prevent the contamination of the sample chamber from the dropping samples. Several small holes are made on the prepared straw by needle as a ventilation holes. The straw is plugged into the sample rod and slide down to the sample space after the purging interlock chamber.

The SQUID is one of the most sensitive instruments for measuring magnetic fields. For the measurement, as a sample moves through the gradiometer pick up coil, the dipole moment of sample induces an electric current in the detection coil. The SQUID connected to the detection coil convert the current

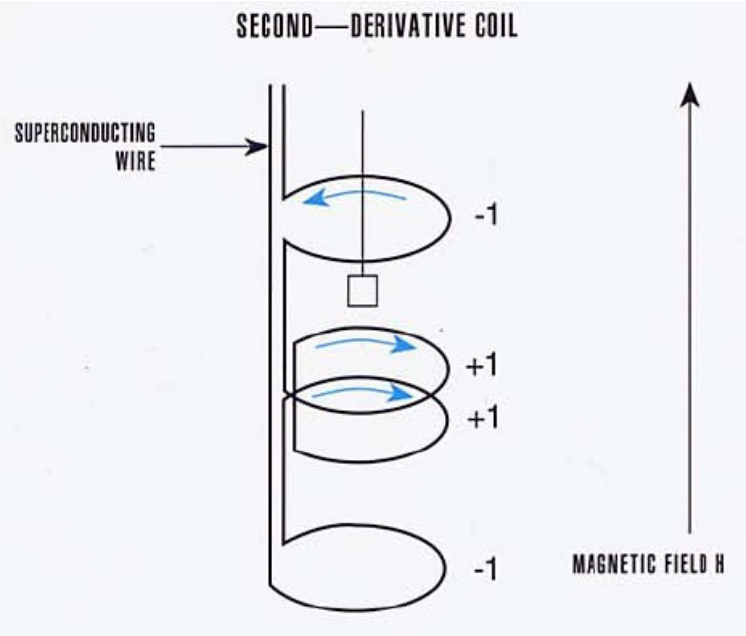

Figure 3.4: The configuration of the second-order gradiometer superconducting detection coil [11].

to voltage linearly. By fitting the response of the output voltage curve to the theoretical calculation of a point dipole moving through the gradiometer, the magnetic moment can be obtained.

The direction of the current between two end coils (up coil and bottom coil) and the center coils are opposite as shown in Fig. 3.4. Thus, the flux change of a uniform field in top and bottom coil will be canceled by the flux change of two center coils. The magnetic moment is measured by the center coils. The system is calibrated using the material which has known mass and magnetic susceptibility.

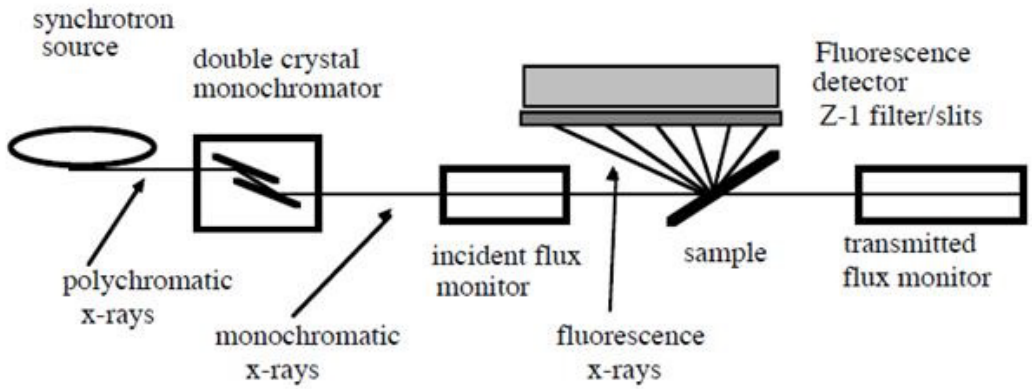

Figure 3.5: Schematic drawing of an EXAFS experimental setup

3.4 X-ray absorption spectroscopy

X-ray absorption spectroscopy (XAS) is one of the widely used technique at synchrotron radiation sources which provides the local structure information of a sample. A typical experimental setup for XAS is shown in Fig. 3.5. The X-rays goes through an ionization chamber to measure the number of incident X-rays (I_0), then through sample, and then through another ionization chamber to measure the number of transmitted X-rays (I_t). The X-ray absorption coefficient is determined by the equation,

$$I_t = I_0 e^{-\mu x} \tag{3.11}$$

$$\mu x = \ln(\frac{I_0}{I_t}) \tag{3.12}$$

where, μ is the absorption coefficient of the sample and x is the thickness of the sample. It also can be obtained by measuring the number of fluorescence

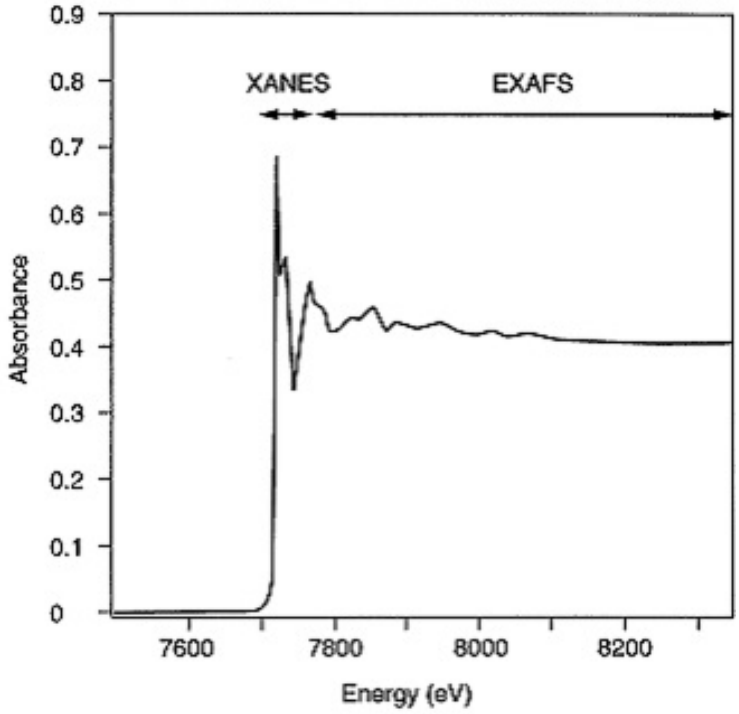

Figure 3.6: Co K-edge X-ray absorption spectrum of $CaCO_3$ showing the XANES and EXAFS regions. [12]

X-rays (I_f) by the equation

$$\mu x \propto \frac{I_f}{I_0}. \tag{3.13}$$

The typical results of XAS spectrum is shown on Fig. 3.6. The sample exposes to an incident monochromatic beam of synchrotron X-rays which is scanned over a range of the energies below and above the absorption edge of the element which we want to focus on in the sample. The absorption spectrum can be divided into two regions, the X-ray absorption near edge

structure (XANES) region and the extended X-ray absorption fine structure (EXAFS) region. XANES is the part of the absorption spectrum near an absorption edge, ranging from approximately -50 to +200 eV relative to the edge energy. EXAFS part of the spectrum is the normalized oscillatory part of the absorption coefficient above the absorption edge to approximately 1000 eV or higher. Analyses of XANES spectrum provides the excitation state of the element of interest while the analyses of EXAFS spectrum provides information on the types and numbers of atoms in coordination with absorber atoms, their interatomic distances, and the degree of local molecular bonding disorder.

The EXAFS spectrum can be understood by the EXAFS equation which can be written in terms of a sum of the contribution form all scattering paths of the photoelectron [60]:

$$\chi(k) = \sum_i \chi_i(k) \tag{3.14}$$

Each paths can be expressed by

$$\chi_i(k) = \frac{(N_i S_0^2) F_{eff_i}(k)}{k R_i^2} \sin\left[2kR_i + \varphi_i(k)\right] e^{-2\sigma_i^2 k^2} e^{-2R_i/\lambda(k)} \tag{3.15}$$

where,

$$R_i = R_{0i} + \Delta R_i, \tag{3.16}$$

$$k^2 = \frac{2m_e(E - E_0 + \Delta E_0)}{\hbar}, \tag{3.17}$$

N_i is the number of i atoms in shell, S_0^2 is amplitude reduction factor, $F_{effi}(k)$ is the effective scattering amplitude of the photoelectron, R_i is the distance to the neighboring atom, $\varphi_i(k)$ is the phase shift of the photoelectron, σ^2 is the the disorder in the neighbor distance, and $\lambda(k)$ is the mean free path of the photoelectron. Therefore, EXAFS equation allows us to determine, N_i, R_i and σ^2 by knowing the scattering amplitude, $F_{effi}(k)$ and the phase shift, $\varphi_i(k)$. The obtained data can be analyzed with the program Athena for background removal and Artemis for optimizing the theoretical model to the measured spectrum [61].

Chapter 4

Local structural disorder and superconductivity in $K_xFe_{2-y}Se_2$

4.1 Introduction

Recently discovered $K_xFe_{2-y}Se_2$ attracts many attentions due to the high superconducting $T_c \sim 31$ K and the phase separation characteristics. In addition, it is reported that the superconducting state can be obtained from an insulating state by post-annealing and fast quenching [62]. To understand superconductivity of $K_xFe_{2-y}Se_2$, it is important to find out how the post annealing and fast quenching process effects on superconducting granular phase and insulating magnetic matrix phase. In this chapter, we discuss post annealing and fast quenching process effects by investigating the temperature dependence of the local structures. We have exploited Fe and Se K-edge spectra using X-ray absorption fine structure (XAFS) of as-grown and quenched $K_{0.69(2)}Fe_{1.45(1)}Se_{2.00(1)}$ in order to examine the local lattice and elec-

tronic structure around the Fe and Se atoms. We show strong evidence that the superconducting volume fraction increase is intimately connected with the increased occupancy of the high symmetry Fe site, accompanied by the increased average Fe-Se distance and decreased average configurational (static) disorder in this distance.

4.2 Experiment

As-grown and quenched $K_{0.69(2)}Fe_{1.45(1)}Se_{2.00(1)}$ single crystals were prepared as described previously [63]. X-ray absorption experiments were completed at beamline X19A of the National Synchrotron Light Source. Temperature-dependent X-ray absorption data were collected in the transmission mode. Gas-filled ionization chamber detectors were used for incident, transmitted, and reference channels. A closed cycle He cryostat was used to cool the samples with temperature control within ± 1 K. A minimum of two scans were measured for each temperature for optimal signal to noise ratio. All XAFS spectra were analyzed using the Athena and Artemis software programs [61].

We compared several different modeling schemes in fitting FEFF6 theory to the experimental data in order to obtain structural information from XAFS analysis. The models compared were: 1) the multiple edge model, where we varied Fe and Se edge data concurrently, by constraining their bond lengths and their disorders to be the same at each temperature, 2) the model where we added a third cumulant to Fe-Se contribution of each data set, 3) the multiple data set model where we constrained the disorder parameter to follow the

Einstein model with static disorder (vide infra), and 4) the model where we added the Fe-Fe contribution to Fe edge fits. After comparing the fit qualities and inspecting the best fit results for their physical meaning, we chose the model (3) for presenting our results, although the main trends in the results remained the same across all models we tried. We found that adding a third cumulant to the final fit model did not change the results within the error bars, and the best fit values of the third cumulant were consistent with zero.

4.3 Results and Discussion

The superconducting volume fractions at 1.8 K of $K_{0.69(2)}Fe_{1.45(1)}Se_{2.00(1)}$ crystals increased by annealing and quenching process from $\sim$ 74.6% to $\sim$ 87.9% (Fig. 4.1 (a)). Moreover, the superconductivity in quenched sample is more homogeneous and sharper at $T_c \sim$ 30K than in as-grown samples (Fig. 4.1 (a)). In addition, there is a significant enhancement of susceptibility in the normal state after post-annealing and quenching process (Fig. 4.1 (b)).

The first nearest neighbors of Fe atoms are Se atoms located at about 2.4 Å distance, and the second nearest neighbors of Fe atoms are Fe atoms, at about 2.8 Å. The first nearest neighbors of Se atoms are Fe atoms with bond distances around 2.4 Å, and the second nearest neighbors are Se atoms, at about 3.9 Å. The peaks around 2 Å (Fig. 4.2) correspond to the Fe-Se and Fe-Fe bond distances (the peak positions are not corrected for the photoelectron phase shifts) for Fe K-edge data (Fig. 4.2 (a)) and only to the Fe-Se bond distances for the Se K-edge data (Fig. 4.2 (b)). The actual distance values

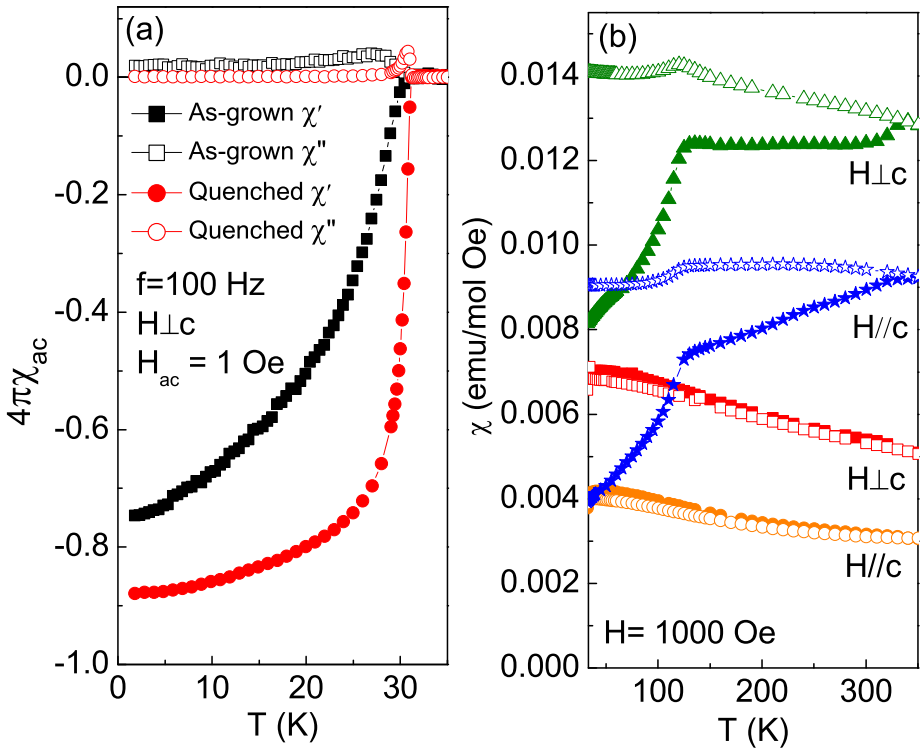

Figure 4.1: (a) Temperature dependence of ac magnetic susceptibility for as-grown (squares) and quenched (circles) $K_{0.69(2)}Fe_{1.45(1)}Se_{2.00(1)}$ taken in H=1 Oe. (b) Temperature dependence ZFC (filled symbols) and FC (open symbols) dc magnetic susceptibility for as-grown (squares and circles) and quenched (triangles and stars) $K_{0.69(2)}Fe_{1.45(1)}Se_{2.00(1)}$ in H=1000 Oe.

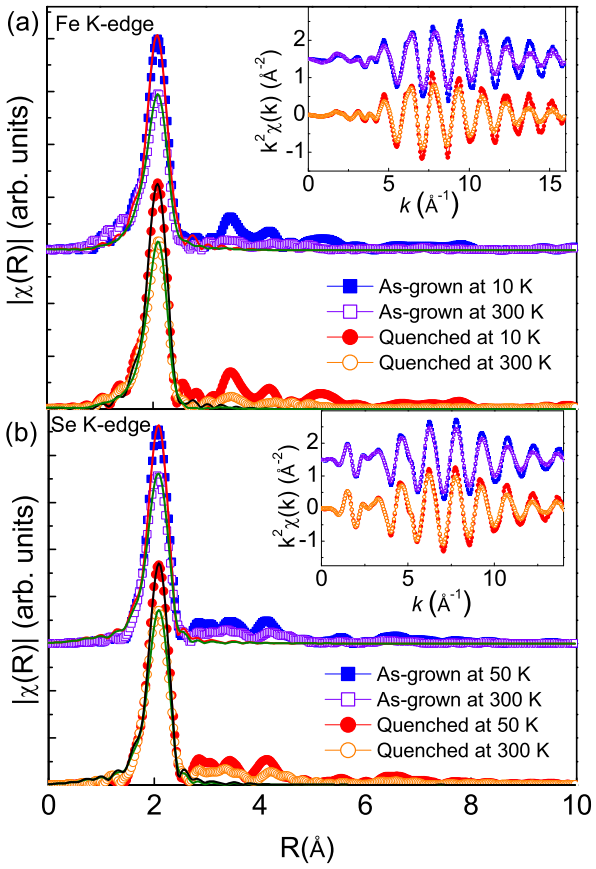

Figure 4.2: Representative Fourier transform (FT) magnitudes of EXAFS data. Fe K-edge results at 10 K and 300 K of as-grown and quenched $K_{0.69(2)}Fe_{1.45(1)}Se_{2.00(1)}$ samples are shown in (a), and Se K-edge results at 50 K and 300 K of both samples are shown in (b). Corresponding EXAFS oscillations are shown in the insets. The FTs are representing raw experimental data without correcting for the phase shifts. The theoretical fits are shown as solid lines.

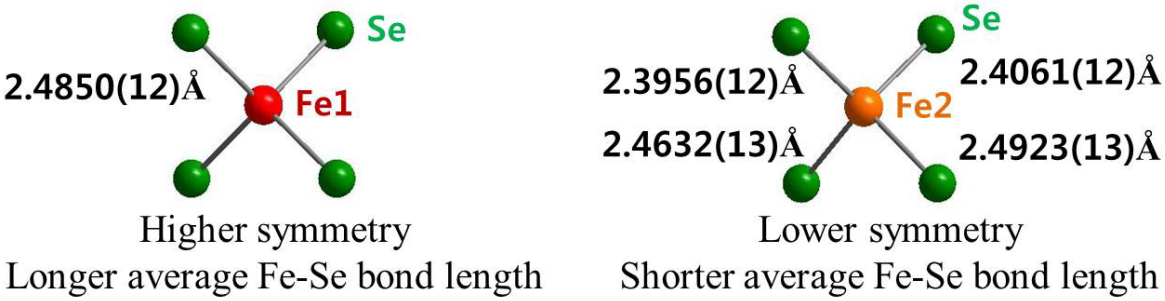

Figure 4.3: Diagram of two different Fe sites with Fe-Se bond distances

were extracted from the theoretical fits.

$K_{0.69(2)}Fe_{1.45(1)}Se_{2.00(1)}$ has two different Fe sites, Fe1 and Fe2 (Fig. 4.3). High symmetry Fe1 site has four Se as first nearest neighbors with identical Fe-Se distance, 2.4850(12) Å determined by the average structure [64]. In contrast, lower symmetry Fe2 site has four nearest neighbor Se atoms with four different Fe-Se bond lengths, 2.3956(12) Å, 2.4632(13) Å, 2.4061(12) Å, and 2.4923(13) Å[64]. Since XAFS probes all Fe sites, the ratio of higher symmetric site (Fe1) and lower symmetric site (Fe2) occupancies can be determined by the average theoretical Fe-Se bond length behavior if both sites are occupied. The average Fe-Se bond length as obtained by XRD is 2.44 Å (2.48 Å) when only lower (higher) symmetric site is occupied. Therefore, the average Fe-Se bond length will increase with the increased occupancy of the high symmetry site. The opposite trend is expected for the static bond length disorder. It is expected to be 0.0016 $Å^2$ with only low symmetry (Fe2) site is occupied, whereas it is 0 when only high symmetry (Fe1) is occupied. Hence, the disorder values should decrease with the increased occupancy of the high symmetry site.

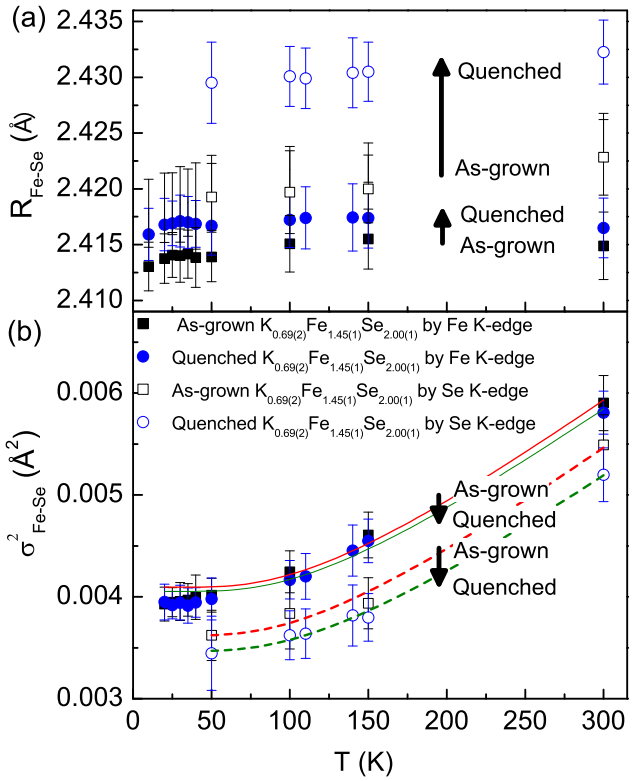

Figure 4.4: (a) Temperature dependence of the Fe-Se distances obtained from the Fe K-edge (filled symbols) and Se K-edge (open symbols) for as-grown (squares) and quenched (circles) $K_{0.69(2)}Fe_{1.45(1)}Se_{2.00(1)}$. (b) Mean square relative displacements σ^2 for the nearest neighbor Fe-Se shell derived from Fe K-edge analysis (filled symbols) and Se K-edge analysis (open symbols) for as-grown (squares) and quenched (circles) $K_{0.69(2)}Fe_{1.45(1)}Se_{2.00(1)}$. σ_s^2 decreases after quenching indicating more uniform nearest-neighbor Fe-Se shell after quenching. The arrows show the trend of change after post-annealing and quenching process.

The XAFS bond distance values are smaller than the Rietveld values. We note that the Fe-Se bond distance was measured from either Fe or Se edge by the Gaussian approximation for the distinct non-Gaussian bond length distribution. Most of the Fe-Se bond distances are distributed on the large distance side, including bond lengths with 2.4632(13) Å, 2.4850(12) Å, and 2.4923(13) Å. Nevertheless few still remain on the lower distance side, thus biasing (lowering) the Gaussian peak position. The Se K-edge Fe-Se bond distances appear larger when compared to the Fe K-edge bond distance (Fig. 4.4 (a)). Even though the XAFS bond distances are smaller when compared to Rietveld values, the relative change in static disorder extracted from the edge is still a reliable measure of relative structural changes. The Fe-Se bond distances increase after quenching (Fig. 4.4 (a)). This is consistent with the expected result that Fe and Se nearest neighbor distance is supposed to increase as Fe1 occupancy increases. In what follows we will focus on the relative change in the occupancies between Fe1 and Fe2 sites.

The mean square relative displacements (MSRD) describe distance-distance correlation function (correlated Debye-Waller factors). They include contributions from the temperature-independent term, σ_s^2, and the temperature-dependent term, $\sigma_d^2(T)$, i.e. $\sigma^2 = \sigma_s^2 + \sigma_d^2(T)$ [65]. The subscripts s and d mean static and dynamic, respectively. Temperature-dependent term is well described by Einstein model: [65]

$$\sigma_d^2(T) = \frac{\hbar}{2\mu\omega_E} \coth(\frac{\hbar\omega_E}{2k_BT}), \tag{4.1}$$

where μ is the reduced mass of the Fe-Se bond and ω_E is the Einstein frequency

related to the Einstein temperature $\theta_E = \hbar\omega_E/k_B$. The fitting curves for as-grown $K_{0.69(2)}Fe_{1.45(1)}Se_{2.00(1)}$ Fe K-edge (red solid line) and Se K-edge (red dotted line) give θ_E =(353 ± 22) K and θ_E = (355 ± 10) K, respectively. Similar analysis for the quenched sample yields θ_E = (359 ± 19) K and θ_E = (364 ± 4) K for Fe K-edge and Se K-edge, respectively. The results are identical within error bars. The relative difference between as-grown and quenched sample static disorder points to the possible rearrangement of Fe1 and Fe2 site occupancies. The static disorder σ_s^2 values obtained from the fits are 0.0020 ± 0.0002 Å^2 for Fe K-edge of both as-grown and quenched samples, and 0.00150 ± 0.00012 Å^2 and 0.00140 ± 0.00004 Å^2 for Se K-edge of as-grown and quenched samples, respectively. The local force constant k can be calculated from $k = \mu\omega_E^2$ [66]. For as-grown and quenched $K_{0.69(2)}Fe_{1.45(1)}Se_{2.00(1)}$ local force constants of Fe-Se bonds are 7.32 ± 0.29 eV/Å^{2}and 7.70 ± 0.12 eV/Å^2, respectively, indicating that the Fe-Se bond hardens after quenching. This is consistent with higher degree of bond order.

Experimentally measured behaviors of the Fe-Se distance (increases in the quenched sample) and its static disorder (decreases in the quenched sample) are consistent with the trends described above and thus can be attributed to the increased occupancy of the high symmetry site in the quenched sample of I4/m parts since I4/mmm has full occupancy as we discussed (Fig. 4.4 (a) and (b)). Also, the magnetic moment on quenched $K_{0.69(2)}Fe_{1.45(1)}Se_{2.00(1)}$ samples doubled (Fig. 4.1 (b)). These results provide clear evidence that Fe1 sites can be associated with much higher magnetic moment (more than five times larger) than Fe2 sites which is consistent with previous reports [67, 68].

What are the implications of our results on nanoscale phase separation and

vacancy disordered superconducting phase in $K_{0.69(2)}Fe_{1.45(1)}Se_{2.00(1)}$ [7, 69, 70]. Superconducting $K_xFe_{2-y}Se_2$ crystals are found for a partially broken iron vacancy order [71], corresponding to narrow region of Fe valence from 2 to about 1.94. This corresponds to deviation from ideal $K_{0.8}Fe_{1.6}Se_{2.00(1)}$ stoichiometry (or more general from $K_{1-x}Fe_{1.5+(x/2)}Se_2$) where Fe1 site is empty and Fe2 is completely occupied ($K_2Fe_4Se_5$ phase) [70–72]. Thus, superconducting crystals are found for $K_{0.8}$ and excess Fe content $Fe_{1.6+x}$ (x >0) [7, 71] suggesting broken vacancy order by some finite Fe1 occupancy, or for $K_{0.69(2)}$ and $Fe_{1.45(1)}$ stoichiometry suggesting broken vacancy order by deficiency on both K and Fe2 sites [64]. This is in agreement that the K content is rather important for superconductivity [71]. Since nominal stoichiometry in our as-grown superconducting crystals was $K_{0.69(2)}Fe_{1.45(1)}Se_{2.00(1)}$ with only Fe2 site occupied [64], the increased occupancy of Fe1 sites in quenched crystals implies further depletion of Fe2 sites and stronger deviation from vacancy ordered $K_{0.8}Fe_{1.6}Se_{2.00(1)}$ insulating phase [7]. Our results provide the first structural evidence that local structure disorder and Fe site occupancy in I4/m part of $K_xFe_{2-y}Se_2$ is the key structure factor for bulk and homogeneous superconductivity in high-T_c iron based superconductor $K_xFe_{2-y}Se_2$.

4.4 Conclusion

In summary, the temperature dependent XAFS study of Fe and Se K-edge spectra of as-grown and quenched $K_{0.69(2)}Fe_{1.45(1)}Se_{2.00(1)}$ samples indicates that the average Fe-Se bond distance increases after quenching due to the

increase in population of high symmetry Fe1 sites which have higher bond distance. For both samples, the temperature dependence of the MSRD of the Fe-Se bonds follows the Einstein model. The static disorder results (σ_s^2) show that the atoms are more ordered after post-annealing and quenching process, also pointing to the increase in Fe1 high symmetry site. Finally, based on the local force constant analysis, Fe-Se bonds become stronger after post-annealing and quenching. This is consistent with the above analysis. Increased occupancy of high symmetry Fe1 site coincides with the large increase in paramagnetic moment, indicating that I4/m phase is strongly magnetic. Simultaneously and surprisingly, superconductivity volume fraction is increased and superconducting T_c is much sharper, suggesting better connectivity of superconducting islands in agreement with conclusions based on SEM, transport and magnetic data [6].

Chapter 5

Multiband transport and non-metallic low-temperature state of $K_{0.50}Na_{0.24}Fe_{1.52}Se_2$

5.1 Introduction

After the discovery of $LaFeAsO_{1-x}F_x$ with $T_c = 26$ K [22] many efforts have been made to study the temperature dependence of the upper critical field, H_{c2}, of Fe-based superconductors since this provides valuable insight in the coherence length, anisotropy, electronic structure, and the pair-breaking mechanism. Binary β-FeSe and Fe_{1+y}(Te,Se) (FeSe-11 type) ans well as arsenic-deficient CuZrSiAs structure-type superconductors (FeAs-1111 type) feature a Pauli-limited H_{c2} and are well explained by the single-band Werthamer-Helfand-Hohenberg (WHH) model [73–76]. On the other hand, in most FeAs-1111 type, ternary pnictide (FeAs-122 type), and chalcogenide (FeSe-122 type)

Cu_2TlSe_2 Fe-based superconductors H_{c2} can only be described by two-band models [77–80]. Studies of the normal state below T_c in both Cu- and Fe-based high-T_c superconductors are rare since very high magnetic fields are required to suppress the superconductivity. Among the few exceptions are studies of $La_{2-x}Sr_xCuO_4$ and $Bi_2Sr_{2-x}La_xCuO_6$, where a logarithmic resistivity and a superconductor-insulator transition (SIT) have been observed in the normal-state region above H_{c2} and below T_c [81–83]. Similar studies in FeSe-122-type superconductors have not been available so far due to their air sensitivity and the demanding experimental conditions of pulsed-field experiments.

In this work, we report on results obtained for single-crystalline $K_{0.50}Na_{0.24}Fe_{1.52}Se_2$ with $T_c \approx 20$ K. $H_{c2}(T)$ is well described by a two-band model. Moreover, when superconductivity is suppressed in high magnetic fields, the in-plane sample resistance follows $R_{ab} \propto \ln(T)$ as $T \to 0$, suggesting a SIT, as commonly observed in granular superconductors.

5.2 Experiment

The $K_{0.50(1)}Na_{0.24(4)}Fe_{1.52(3)}Se_{2.00(5)}$ single crystals used in this study were synthesized and characterized as described previously with a nominal composition of starting materials K:Na:Fe:Se = 0.6:0.2:2:2 [64]. The as-grown crystals were sealed in a Pyrex tube under vacuum ($\sim 10^{-1}$ Pa), annealed at 400°C for 3 hours, and then quenched in air in order to increase the superconducting volume fraction [62, 84, 85]. Powder x-ray diffraction (XRD) spectra were taken with Cu K_α radiation ($\lambda = 0.15418$ nm) by a Rigaku Miniflex X-ray machine.

The lattice parameters were obtained by refining XRD spectra using the Rietica software [58]. The elemental analysis was done using a scanning electron microscope (SEM). Magnetization measurements were performed in a Quantum Design MPMS-XL5. The ac magnetic susceptibility was measured with an excitation frequency of 100 Hz and field of 1 Oe. Electrical-resistivity measurements were conducted using a standard four-probe method in a PPMS-14. Pulsed-field experiments were performed up to 62 T using a magnet with 150 ms pulse duration and data were obtained via a fast data acquisition system operating with AC current in the kHz range. Contacts were made on freshly cleaved surfaces inside a glove box.

5.3 Results and Discussion

The powder XRD data (Fig. 5.1 (a)) demonstrate the phase purity of our samples without any extrinsic peak present. The pattern is refined in the space groups $I4/mmm$ and $I4/m$ with fitted lattice parameters $a = 0.3870(2)$ nm, $c = 1.4160(2)$ nm and $a = 0.8833(2)$ nm, $c = 1.4075(2)$ nm, respectively, reflecting phase separation and small sample yield [7, 44, 69, 86–88]. With Na substitution, the lattice parameter a decreases while c increases when compared to $K_{0.8}Fe_2Se_2$, consistent with lattice parameters of $NaFe_2Se_2$ [1, 89]. The average stoichiometry was determined by EDX, measuring multiple positions on the crystal. The obtained composition $K_{0.50(1)}Na_{0.24(4)}Fe_{1.52(3)}Se_{2.00(5)}$ suggests vacancies on both K and Fe sites. FeSe-122 superconductors feature an intrinsic phase separation into magnetic insulating and supercon-

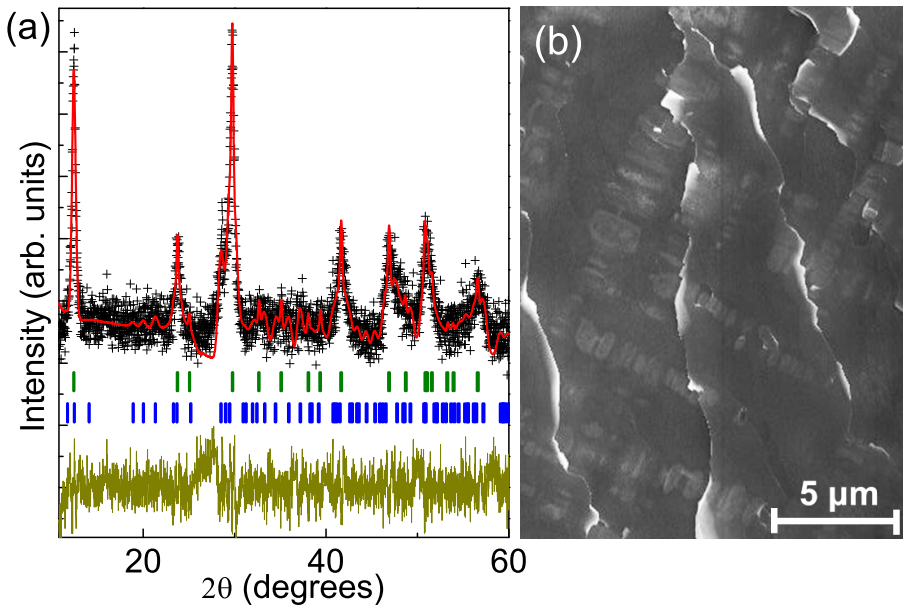

Figure 5.1: (a) Powder XRD pattern of $K_{0.50(1)}Na_{0.24(4)}Fe_{1.52(3)}Se_2$. The plot shows the observed (+) and calculated (solid red line) powder pattern with the difference curve underneath. Vertical tick marks represent Bragg reflections in the I4/mmm (upper green marks) and I4/m (lower blue marks) space group. (b) SEM image of the crystal.

ducting regions [7, 70, 86–88]. As shown in the SEM image of Fig. 5.1 (b), $K_{0.50(1)}Na_{0.24(4)}Fe_{1.52(3)}Se_2$ also exhibits a similar array of superconducting grains in an insulating matrix. The observed pattern is somewhat inhomogeneous [Fig. 5.1 (b)] with sizes ranging from about several microns to probably several tens of nanometers [7], below our resolution limit.

The investigated single crystal becomes superconducting at 20 K after and at 28 K before the annealing and quenching procedure [Fig. 5.2 (a) main part and inset, respectively] [84, 85]. For the quenched crystal, the superconducting volume fraction at 1.8 K increases significantly up to 72%, albeit with a reduction of T_c. The post-annealing and quenching process results in a surface oxidation of some crystals which then dominates the magnetization signal. However, Fe_3O_4 is not visible in either of our laboratory or synchrotron X-ray studies [62, 84, 85]. The magnetic hysteresis loops (MHL) of the quenched $K_{0.50(1)}Na_{0.24(4)}Fe_{1.52(3)}Se_2$ single crystal reflects the improvement in crystalline homogeneity since it is much larger and symmetric when compared to an as-grown sample (Fig. 5.2 (b)) due to stronger pinning forces and bulk pinning [90]. Also similar to $K_xFe_{2-y}Se_2$, there is an enhancement of the in-plane critical-current density calculated from the Bean model [91, 92]: $J_c^{ab}(\mu_0 H) = \frac{20\Delta M(\mu_0 H)}{a(1-a/3b)}$, where a, b, and c are the lengths of a rectangularly shaped crystal ($b > a > c$). In view of the improved volume fraction and homogeneity, further investigations of the electronic transport properties were performed on the quenched crystal.

The resistance of an inhomogeneous sample contains contributions from both metallic (R_m) and nonmetallic (R_i) regions. At $T < T_c$, due to superconductivity ($R_m = 0$) the insulating part of the sample is short-circuited. The

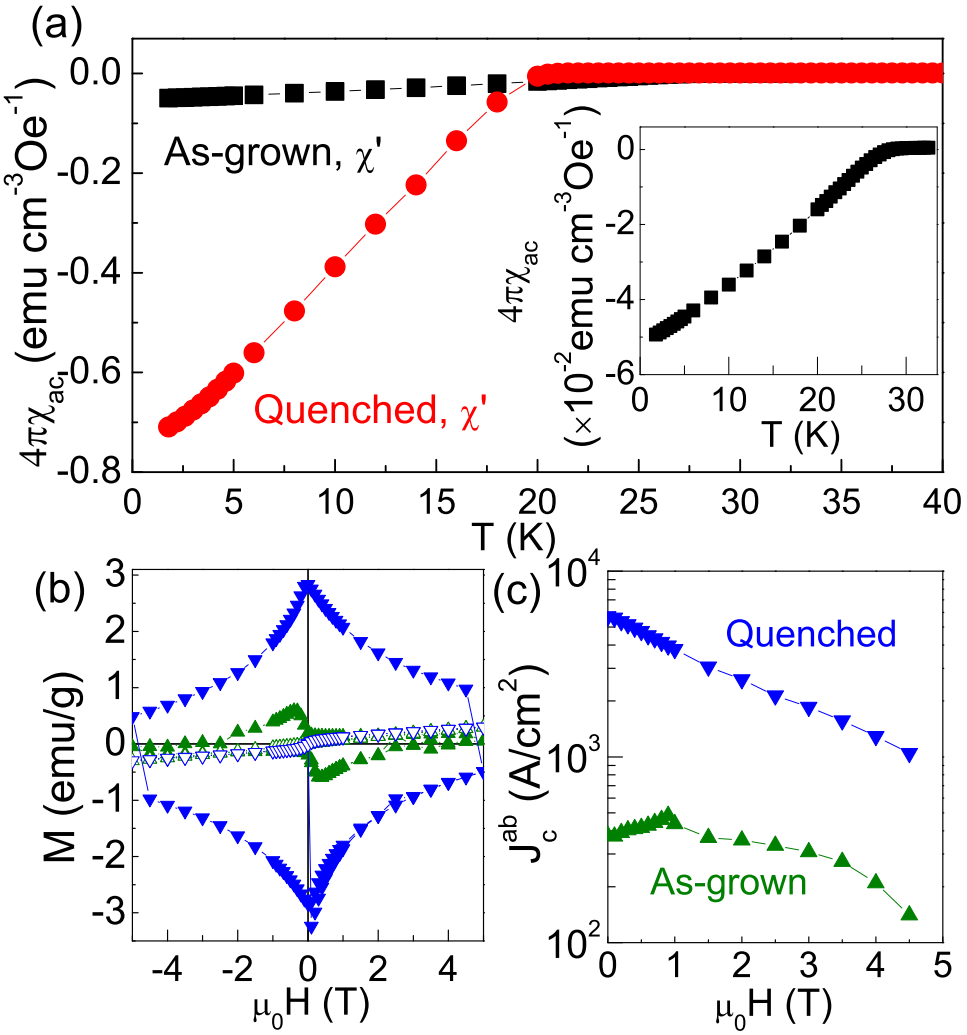

Figure 5.2: (a) Temperature dependence of the ac magnetic susceptibilities of as-grown (magnified in the inset) and quenched $K_{0.50(1)}Na_{0.24(4)}Fe_{1.52(3)}Se_2$. (b) Magnetic hysteresis loops of as-grown (triangles) and quenched (inverted triangles) samples at $T = 1.8$ K (closed symbols) and $T = 300$ K (open symbols) for $H \| c$. (c) Superconducting critical current densities, $J_c^{ab}(\mu_0 H)$, at $T = 1.8$ K.

insulating regions have a several orders of magnitude higher resistivity than the metallic part [93]; hence, around T_c and when $T \to 0$ in the high-field normal state $R(T) \approx R_m(T)$. This is similar to the resistance of a polycrystalline sample in the presence of grain boundaries and in agreement with the observation that insulating regions do not contribute to the spectral weight in angular resolved photoemission data in the energy range near E_F [94]. In what follows below, we focus on the temperature-dependent sample resistance, $R(T)$.

The superconducting transition in $R_{ab}(T)$ is rather wide and shifts to lower temperatures in applied magnetic fields [Figs. 5.3 (a) and (b)]. The shift is more pronounced for $H\|c$, which implies an anisotropic $\mu_0 H_{c2}$. The temperature-dependent upper critical fields shown in Fig. 5.3(c) were determined from the resistivity drops to 90%, 50%, and 10% of the normal-state value. It is clear that all experimental data feature a similar temperature dependence irrespective of the criteria used. All data for $H\|c$ are above the expected values for the single band Werthamer-Helfand-Hohenberg (WHH) model (dotted lines). We proceed our further analysis using the 10% values, similar as done for $LaFeAsO_{0.89}F_{0.11}$ [77]. The $H_{c2}(T)$ curves are linear for $H \perp c$ near T_c and show an upturn at low T for $H\|c$ [Fig. 5.3(d)]. The initial

Table 5.1: Superconducting parameters of the quenched $K_{0.50(1)}Na_{0.24(4)}Fe_{1.52(3)}Se_2$ single crystal.

	T_c (K)	$(d\mu_0 H_{c2}/dT)\|_{T=T_c}$ (T/K)	$\mu_0 H_{c2}(0)$ (T)	$\xi(0)$ (nm)
H⊥c	14.1(5)	-4.3(3)	150∼160	2.62∼2.95
H‖c	14.1(5)	-1.1(2)	38∼48	0.75∼0.79

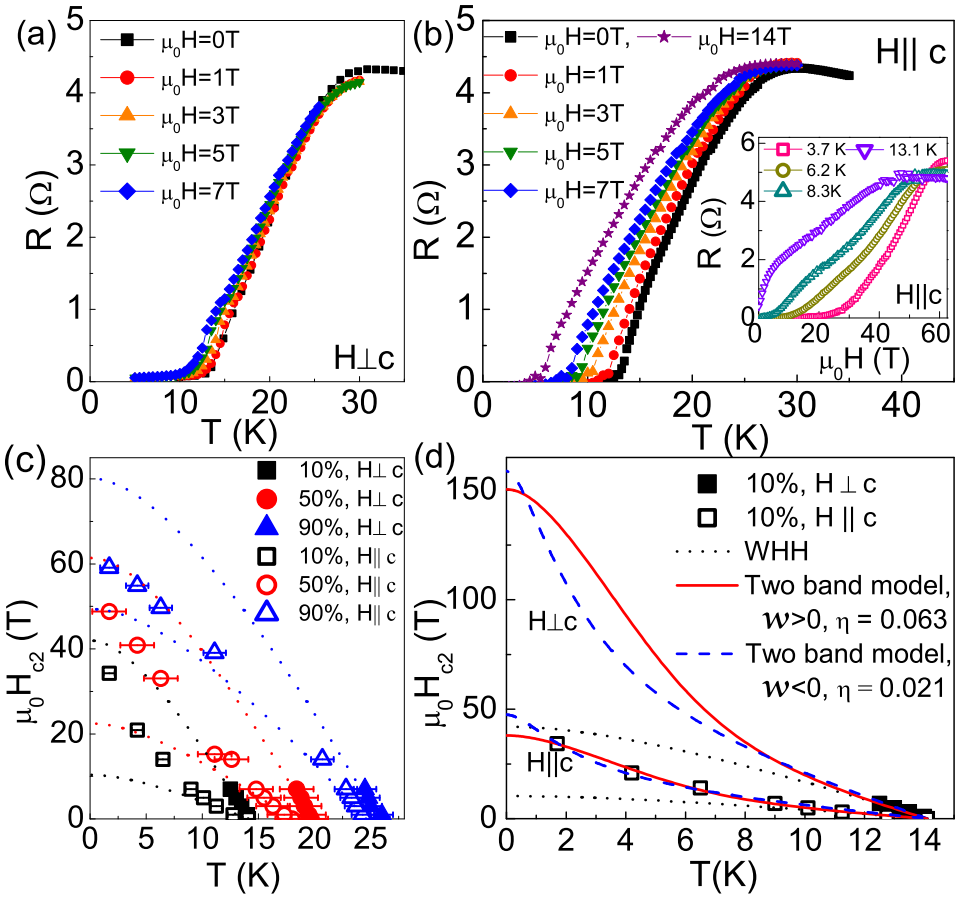

Figure 5.3: In-plane resistivity, $R_{ab}(T)$, of $K_{0.50(1)}Na_{0.24(4)}Fe_{1.52(3)}Se_2$ for (a) $H \perp c$ and (b) $H \| c$. The inset in (b) shows $R_{ab}(T)$ measured at various temperatures in pulsed magnetic fields up to 63 T. (c) Temperature dependence of the resistive upper critical field, $\mu_0 H_{c2}$, determined using three different criteria (10%, 50%, and 90% of the normal-state value). Dotted lines are the WHH plots. (d) Superconducting upper critical fields for $H \perp c$ (closed symbols) and $H \| c$ (open symbols) using Eq. (1) with different pair breaking mechanisms: (1) WHH (dotted line), (2) two-band model with $w > 0$, $\eta = 0.063$ (solid line), and (3) two-band model with $w < 0$, $\eta = 0.021$ (dashed line).

slope near T_c for $H \perp c$ is much larger than for $H \| c$ (Fig. 5.3(d) and Table 5.1). These slopes are similar to values for as-grown and quenched $K_xFe_{2-y}Se_2$ [64, 80].

There are two basics mechanisms of Cooper-pair breaking by magnetic field in a superconductor. Orbital pair breaking imposes an orbital limit due to the induced screening currents, whereas the Zeeman effect contributes to the Pauli paramagnetic limit of H_{c2}. In the single-band WHH approach, the orbital critical field is given by $\mu_0 H_{c2}(0) = -0.693 T_c (d\mu_0 H_{c2}/dT)|_{T=T_c}$ [95]. For $K_{0.50(1)}Na_{0.24(4)}Fe_{1.52(3)}Se_2$, this leads to 42(3) T for $H \perp c$ and 10(2) T for $H \| c$ [Fig. 5.3(d)]. On the other hand, the Pauli-limiting field is given by $\mu_0 H_p(0) = 1.86 T_c (1 + \lambda_{e-ph})^{1/2}$, where λ_{e-ph} is the electron-phonon coupling parameter [96]. Assuming $\lambda_{e-ph} = 0.5$, which is a typical value for a weak-coupling BCS superconductor [97], $\mu_0 H_p(0)$ is 32(1) T. This is larger than the orbital pair-breaking field for $H \| c$ estimated above, yet smaller than the value for $H \perp c$, which possibly implies that electron-phonon coupling is much stronger than for typical weak-coupling BCS superconductors.

The experimental data for $\mu_0 H_{c2}(0)$ lie above the expected values from WHH theory [Fig. 5.3(d)], suggesting that multiband effects are not negligible. In the dirty limit, the upper critical field found for the two-band BCS model with orbital pair breaking and negligible interband scattering is [98]:

$$a_0 [\ln t + U(h)] [\ln t + U(\eta h)] + a_2 [\ln t + U(\eta h)] + a_1 [\ln t + U(h)] = 0, \quad (5.1)$$

$$U(x) = \psi(1/2 + x) - \psi(1/2), \quad (5.2)$$

where $t = T/T_c$, $\psi(x)$ is the digamma function, $\eta = D_2/D_1$, D_1 and D_2 are diffusivities in band 1 and band 2, $h = H_{c2}D_1/(2\phi_0 T)$, and $\phi_0 = 2.07 \times 10^{-15}$ Wb is the magnetic flux quantum. $a_0 = 2w/\lambda_0$, $a_1 = 1 + \lambda_-/\lambda_0$, and $a_2 = 1 - \lambda_-/\lambda_0$, where, $w = \lambda_{11}\lambda_{22} - \lambda_{12}\lambda_{21}$, $\lambda_0 = (\lambda_-^2 + 4\lambda_{12}\lambda_{21})^{1/2}$, and $\lambda_- = \lambda_{11} - \lambda_{22}$. λ_{11} and λ_{22} are pairing (intraband coupling) constants in band 1 and 2, and λ_{12} and λ_{21} quantify interband couplings between band 1 and 2. For $D_1 = D_2$, Eq. (1) simplifies to the one-band model (WHH) in the dirty limit [95]. When describing our data by use of the two-band BCS model fitting, we consider two different cases, $w > 0$ and $w < 0$, which imply either dominant intraband or dominant interband coupling, respectively. The solid lines in Fig. 5.3(d) are fits using Eq. (1) for $\lambda_{11} = \lambda_{22} = 0.5$ and $\lambda_{12} = \lambda_{21} = 0.25$ which indicates strong intraband coupling [78, 90]. The extrapolated $\mu_0 H_{c2}(0)$ is ∼38 T for $H \| c$ and ∼150 T for $H \perp c$. Further, the dashed lines in Fig. 5.3(d) show fits with $\lambda_{11} = \lambda_{22} = 0.49$ and $\lambda_{12} = \lambda_{21} = 0.5$ for strong interband coupling [78, 90] that give $\mu_0 H_{c2}(0)$ ∼48 T for $H \| c$ and ∼160 T for $H \perp c$.

From these fits we obtain η values of 0.063 and 0.021 for dominant intraband ($w > 0$) and interband ($w < 0$) coupling, respectively, i.e., largely different D_1 and D_2 implying different electron mobilities in the two bands. The upward curvature of $\mu_0 H_{c2}(T)$ is governed by η; it is more pronounced for $\eta \ll 1$. The large difference in the intraband diffusivities could be due to pronounced differences in effective masses, scattering, or strong magnetic excitations [78, 98]. The fit results are not very sensitive to the choice of the coupling constants, yet they mostly depend on η. This indicates either similar interband and intraband coupling strengths or that their difference is beyond our resolution limit.

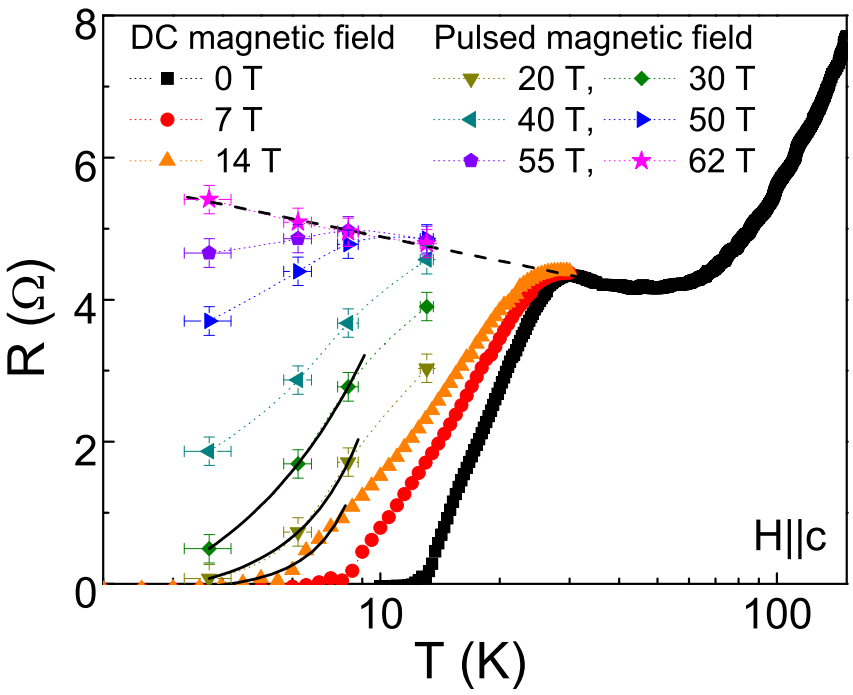

Figure 5.4: Temperature dependence of the resistance in several DC and pulsed magnetic fields for $H \| c$.

Due to the limited data points, it is difficult to unambiguously estimate $\mu_0 H_{c2}(0)$ for $H \perp c$. Based on results reported for similar Fe-based superconductors, $NdFeAsO_{0.7}Fe_{0.3}$ [78], $(Ba,K)Fe_2As_2$ [99], and $K_{0.8}Fe_{1.76}Se_2$ [80], $\mu_0 H_{c2}(0)$ shows a pronounced upward curvature for $H \| c$ while it tends to saturate for $H \perp c$. The real $\mu_0 H_{c2}(0)$ for $H \perp c$ might be smaller than we estimated. The calculated coherence lengths, using $\mu_0 H_{c2}^{\perp}(0) = \phi_0 / 2\pi \xi_{\perp}(0) \xi_{\|}(0)$ and $\mu_0 H_{c2}^{\|}(0) = \phi_0 / 2\pi \xi_{\perp}(0)^2$ based on the two-band BCS fit results, are similar to values obtained for as-grown and quenched $K_x Fe_{2-y} Se_2$ and are shown in Table 5.1 [74, 80].

Superconductivity in $K_{0.50(1)}Na_{0.24(4)}Fe_{1.52(3)}Se_2$ is completely suppressed above about 60 T for $H \| c$, allowing for a clear insight into the low-temperature electronic transport in the normal state (Fig. 5.4). Interestingly, we do not observe metallic transport below about 40 K implying that a superconductor-to-insulator transition (SIT) is induced in high magnetic fields. Kondo-type magnetic scattering is not very likely since a field of 62 T should suppress spin-flip scattering [81]. A thermally activated semiconductor-like transport or variable range hopping (VRH) as occurring for Anderson localization is unlikely since the resistance in 62 T cannot be fit by $\ln R \propto -1/T$, $\ln R \propto T^{-\beta}$, with $\beta = 1/2,\ 1/3,\ 1/4$, and $\ln R \propto \ln T$ [100–102]. Instead, the resistance increases logarithmically with decreasing temperature in the normal state at 62 T as shown with the dashed line in Fig. 5.4. Hence, the SIT might originate from the granular nature of $K_{0.50(1)}Na_{0.24(4)}Fe_{1.52(3)}Se_2$. In a bosonic SIT scenario, Cooper pairs are localized in granules [103, 104]. When $H > H_{c2}$, virtual Cooper pairs form, yet they cannot hop to other granules when $T \to 0$ which induces the increase in resistivity as temperature decreases. The grain size can be estimated from $H_{c2}^0 \sim \phi_0/L\xi$, where L is the average grain radius and $\xi \approx 0.77$ nm is the average in-plane coherence length. The obtained $L = 62$ nm is in agreement with the phase-separation distance. The bosonic SIT mechanism in granular superconductors predicts $R = R_0 \exp(T/T_0)$ ('inverse Arrhenius law') in the superconducting region near the SIT when $H < H_{c2}$ due to the destruction of quasi-localized Cooper pairs by superconducting fluctuations. Our data in 14, 20, and 30 T can be well fitted with this formula (solid lines in Fig. 5.4).

5.4 Conclusion

In summary, we reported the multiband nature of superconductivity in $K_{0.50}Na_{0.24}Fe_{1.52}Se_2$ as evidenced in the temperature dependence of the upper critical field and a SIT in high magnetic fields. Granular type-I but also copper-oxide superconductors are also intrinsically phase separated on the nanoscale [105–108]. Hence, a SIT in high magnetic fields seems to be connected with the intrinsic materials' granularity in inhomogeneous superconductors. This suggests that the insulating states found in cuprates as a function of magnetic field [81, 82] or doping [109] might involve Josephson coupling of nanoscale grains as opposed to quasi-one-dimensional metallic stripes bridged by Mott-insulating regions in the spin-charge separated picture [110].

Chapter 6

Insulating and metallic spin glass in $K_xFe_{2-\delta-y}Ni_ySe_2$ ($0.06 \leq y \leq 1.44$) single crystals

6.1 Introduction

Perturbation of the ground state in Fe-based superconductors by chemical substitutions is rather instructive. Ba doping on KFe_2As_2 increases T_c to 38 K [28], whereas S doping on KFe_2Se_2 suppresses superconductivity [64]. Equally interesting is substitution of transition metal with unpaired 3d electrons and with similar ionic radius on Fe site. For instance, superconductivity is induced by Co and/or Ni doping on LaFeAsO, CaFeAsF, $SrFe_2As_2$, and $BaFe_2As_2$ [111–115]. On the other hand, Co or Ni substitutions on Fe atomic positions in FeSe significantly suppress superconductivity [35].

In this work, we have investigated structure, transport, magnetic, and

optical properties of Ni substituted $K_xFe_{2-\delta}Se_2$ single crystal series, where δ is Fe vacancy. Superconductivity is suppressed with much faster rate when compared to crystallographic phase separation. We observe rich ground state phase diagram where insulating magnetic spin glass gives way to metallic with further Ni concentration.

6.2 Experiment

Single crystals of $K_xFe_{2-\delta-y}Ni_ySe_2$ used in this study were grown as described previously [64, 116]. The platelike crystals with typical size 5×5×2 mm^3 were grown. High energy synchrotron X-ray experiment at 300 K was conducted on X7B beamline of the National Synchrotron Light Source (NSLS) at Brookhaven National Laboratory (BNL). The setup utilized X-ray beam 0.5 mm × 0.5 mm in size with wavelength of 0.3196 $\mathring{A}$ (E = 38.7936 keV) configured with a focusing double crystal bent Laue monochomator, and Perkin-Elmer amorphous silicon image plate detector mounted perpendicular to the primary beam path. Finely pulverized samples were packed in cylindrical polyimide capillaries 1 mm in diameter and placed 377.81 mm away from the detector. Multiple scans were performed to a total exposure time of 240 s. The 2D diffraction data were integrated and converted to intensity versus 2θ using the software FIT2D [117]. Structural refinements were carried out using GSAS modeling program [118] operated by EXPGUI platform [119]. The average stoichiometry was determined by energy-dispersive x-ray spectroscopy (EDX) in an JEOL JSM-6500 scanning electron microscope. Magnetization measure-

ments, electric and thermal transport, and heat capacity were performed in a Quantum Design MPMS-XL5 and PPMS-9. Raman scattering measurements were performed on freshly cleaved samples using a JY T64000 Raman system in backscattering micro-Raman configuration. The 514.5 nm line of a mixed Ar^+/Kr^+ gas laser was used as an excitation source. The corresponding excitation power density was less than 0.2 kW/cm^2. Low temperature Raman measurements were performed using KONTI CryoVac continuous flow cryostat with 0.5 mm thick window.

The in-plane resistivity $\rho_{ab}(T)$ was measured using a four-probe configuration on cleaved rectangularly shaped single crystals with current flowing in the *ab*-plane of tetragonal structure. Thin Pt wires were attached to electrical contacts made of silver paste. Thermal transport properties were measured in Quantum Design PPMS-9 from 2 to 350 K using a one-heater two-thermometer method. The relative error was $\frac{\Delta\kappa}{\kappa}$ ~5% and $\frac{\Delta S}{S}$ ~5% based on Ni standard measured under identical conditions.

6.3 Results and Discussion

Obtained high energy synchrotron XRD results of $K_xFe_{2-\delta-y}Ni_ySe_2$ series can be fitted very well with $I4/m$ and $I4/mmm$ space groups when y≤0.73(0), while they are fitted by $I4/mmm$ space group only when y≥1.13(1) (Fig. 6.1 (a)). This implies $I4/m$ and $I4/mmm$ phases coexist when y≤0.73(0). There is small amount of SeO_2 due to the oxidization. To make quantitative comparison of average structure in the alloy series (Fig. 6.1 (b)) only $I4/m$

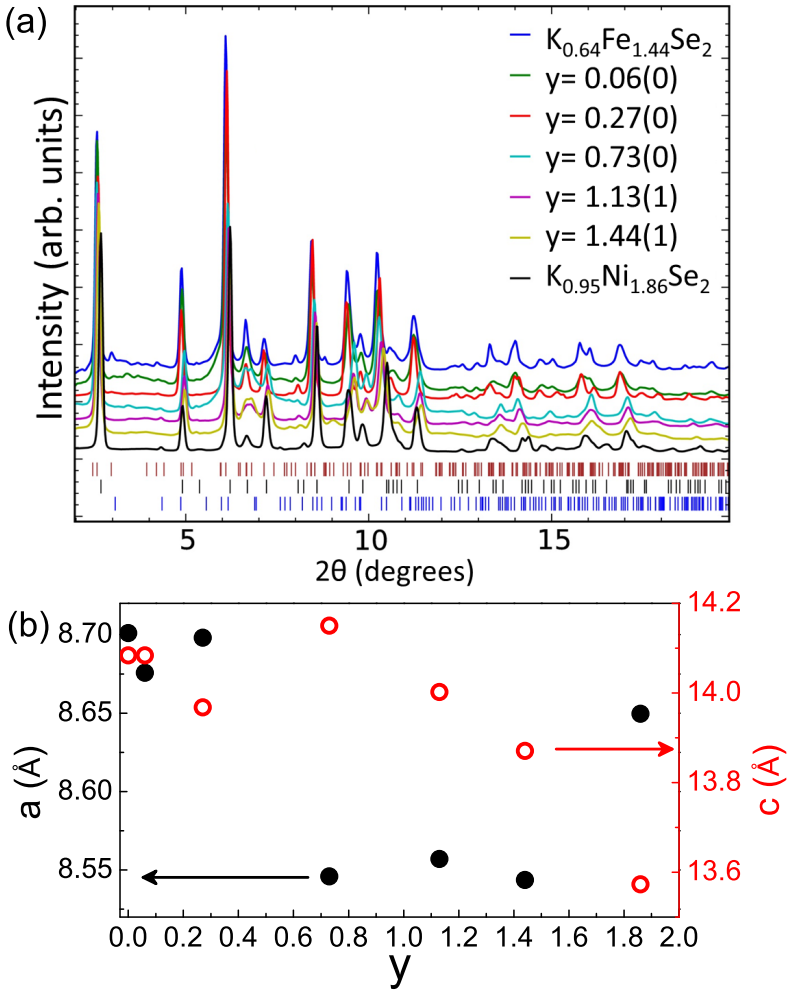

Figure 6.1: (a) High energy synchrotron X-ray diffraction data of $K_xFe_{2-\delta-y}Ni_ySe_2$ series. Upper, middle, and lower vertical tick marks are for $I4/m$ phase, $I4/mmm$ phase, and SeO_2 reflections, respectively. (b) Lattice parameters as a function of Ni content y in $K_xFe_{2-\delta-y}Ni_ySe_2$. Filled circles are for lattice parameter a and open circles are for lattice parameter c.

Table 6.1: Summary of measured stoichiometry of $K_xFe_{2-\delta-y}Ni_ySe_2$ samples. The first column shows nominal values used in synthesis process.

K:Fe:Ni:Se	K	Fe	Ni	Se
1:1.8:0.2:2	0.73(0)	1.37(1)	0.06(0)	2
1:1.4:0.6:2	0.87(2)	1.15(1)	0.27(0)	2
1:1:1:2	0.84(0)	0.85(0)	0.73(0)	2
1:0.6:1.4:2	0.83(0)	0.56(0)	1.13(1)	2
1:0.2:1.8:2	0.82(0)	0.26(1)	1.44(1)	2

space group is used for the refinements when y≤0.73(0), since this results in the same goodness-of-fit when compared to the refinements using both $I4/m$ and $I4/mmm$ space groups. For y≥1.13(1), $I4/mmm$ space group is used to determine the lattice parameters which are then converted into comparable numbers for $I4/m$ space group using the formula $I4/m = \sqrt{5}\ I4/mmm$ for a-axis lattice parameters. Notice that there are considerable changes in lattice parameter a around $y = 0.73(0)$ and $y = 1.44(1)$. On the other hand, the lattice parameter c starts to decrease when $y = 0.73(0)$ as the Fe/Ni sites are filled with Ni. Nonmonotonic evolution of lattice parameters highlights complex crystal structure and bonding in $K_xFe_{2-y}Ni_ySe_2$. Average atomic ratio of K, Fe, Ni and Se in crystals is shown in Table 6.1. Defects and deficiency of Fe(Ni) stoichiometry is commonly found in AFeCh-122 compounds [1, 120, 121]. As the Ni ratio increases, deficiency of K and sum of Fe and Ni decreases, consistent with results on KNi_2Se_2 single crystals [120].

$K_{0.8}Fe_2Se_2$ shows superconductivity below 30 K and metal to semiconductor transition at higher temperatures [1]. As shown in Fig. 6.2 (a), 4.2 % of Ni doping on $K_{0.8}Fe_2Se_2$ single crystal suppresses not only superconductivity but also conductivity and results in an insulating $\rho(T)$. However, as Ni substi-

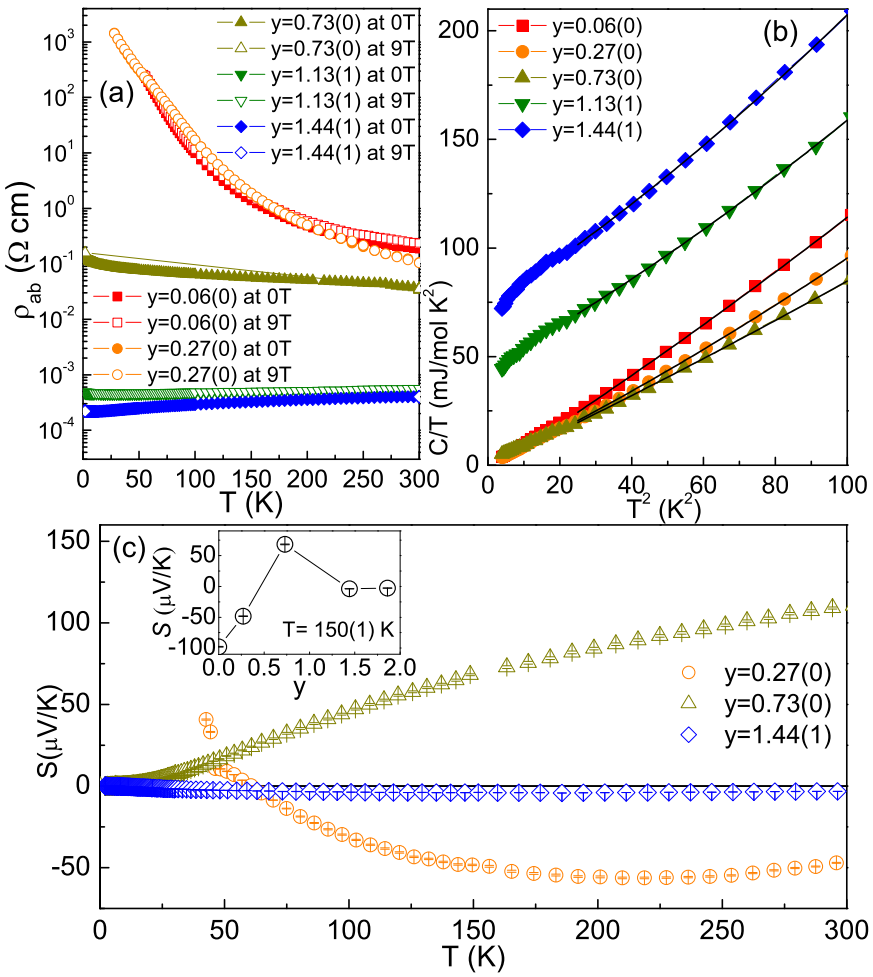

Figure 6.2: (a) Temperature dependence of the in-plane resistivity on $K_xFe_{2-\delta-y}Ni_ySe_2$ series at zero and 9 T field. (b) The relation between C/T and T^2 for $K_xFe_{2-\delta-y}Ni_ySe_2$ series at low temperature. The solid lines represent fits by the equation $C/T=\gamma+\beta_3T^2+\beta_5T^4$. (c) Temperature dependence of thermoelectric power S(T) for $K_xFe_{2-\delta-y}Ni_ySe_2$ series. The inset shows the thermoelectric power at T=150 K for different Ni concentrations with adding results for y=0 and y=1.86(2) from Ref. 38 and 31.

Table 6.2: Summary of γ values and Debye temperatures in $K_xFe_{2-\delta-y}Ni_ySe_2$

y	γ(mJ mol^{-1} K^{-2})	Θ_D(K)
0.06(0)	0.6(4)	210(3)
0.27(0)	0.3(2)	230(6)
0.73(0)	0.2(1)	232(2)
1.13(1)	45(7)	218(3)
1.44(1)	72(9)	208(5)

tutes for Fe further, conductivity increases up to the highest Ni concentration in $K_{0.95}Ni_{1.86}Se_2$, consistent with previous study [120].

Relation between C/T and T^2 also shows insulator to metal transition as Ni concentration increases, as shown in Fig. 6.2 (b). The electronic specific heat and Debye temperature are obtained by the fitting on C/T-T^2 curves from 5 K to 10 K region using the formula $C/T=\gamma+\beta_3T^2+\beta_5T^4$. The Debye temperatures are estimated by the formula $\Theta_D = (12\pi^4 NR/5\beta)^{1/3}$, where N is the atomic number in the chemical formula and R is the gas constant. The obtained γ values and Debye temperatures Θ_D for different Ni concentrations are listed in the Table 6.2. All samples in $K_xFe_{2-\delta-y}Ni_ySe_2$ series have similar Θ_D values which reflects no significant changes in atomic weight, structure and bonding. In addition, γ values are negligible for $y \leq 0.73(0)$ suggesting minute density of states at the Fermi level as expected for an insulator. Larger γ values for $y > 0.73(0)$ region reflect rapid pileup of the density of states $N(E_F)$ in the metallic region and possible heavy fermion-like behavior [116, 122].

Temperature dependence of thermoelectric power S(T) for $K_xFe_{2-\delta-y}Ni_ySe_2$ series is shown in the main part whereas S(y) at 150 K is presented in the inset of Fig. 6.2 (c). Large Fermi surface changes are evident around y=0.73(0); this coincides with the notable lattice parameter change in XRD results.

The changes are related to the metal insulator transition. It is interesting that the dominant carriers for end members of $K_xFe_{2-\delta-y}Ni_ySe_2$ (y=0 and y=1.86(2))[120, 123] are electrons at high temperature whereas they are holes for samples in the middle of the series.

Temperature dependent anisotropic magnetization for $K_xFe_{2-\delta-y}Ni_ySe_2$ series is shown in Fig. 6.3 (a) and (b). A pronounced irreversible behaviors between zero-field-cooling (ZFC) and field-cooling (FC) curves below 50 K is observed. The irreversibility implies a magnetic spin glass where the spins are locked or frozen into random orientations below a characteristic temperature T_f. Similar behavior has been reported in $TlFe_{2-x}Se_2$, $KFeCuS_2$, and $K_xFe_{2-\delta}S_2$ [120, 124, 125]. M-H loops in insets of Fig. 6.3 (a) and (b) also support glassy nature of the transition by presenting nearly linear field dependence with no hysteresis at 300 K or s-shape loop at 1.8 K [124]. Fig. 6.3 (c) shows the frequency dependent peak of the real part in ac susceptibility $\chi'(T)$. As the frequency increases, peak position moves to the higher temperature while magnitude decreases, another hallmark of the typical spin glass behavior [126]. Relation between T_f and frequency can be fitted by $K=\Delta T_f/(T_f \Delta \log f)$, and the obtained K value is 0.0050(2). This is in agreement with the values ($0.0045 \leq K \leq 0.08$) for a canonical spin glass [126]. Thermoremanent magnetization (TRM) is shown in Fig. 6.3 (d). The sample was cooled down from 100 K (above T_f) to 10 K (below T_f) in different magnetic fields, and kept there for $t_w = 100s$. Then, magnetic field was switched off and magnetization decay $M_{TRM}(t)$ was measured. At T = 10 K, $M_{TRM}(t)$ shows slow decay, so $M_{TRM}(t)$ has non-zero values even after several hours. The slow decay of $M_{TRM}(t)$ is another typical property of magnetic spin glass [126]. On the other hand,

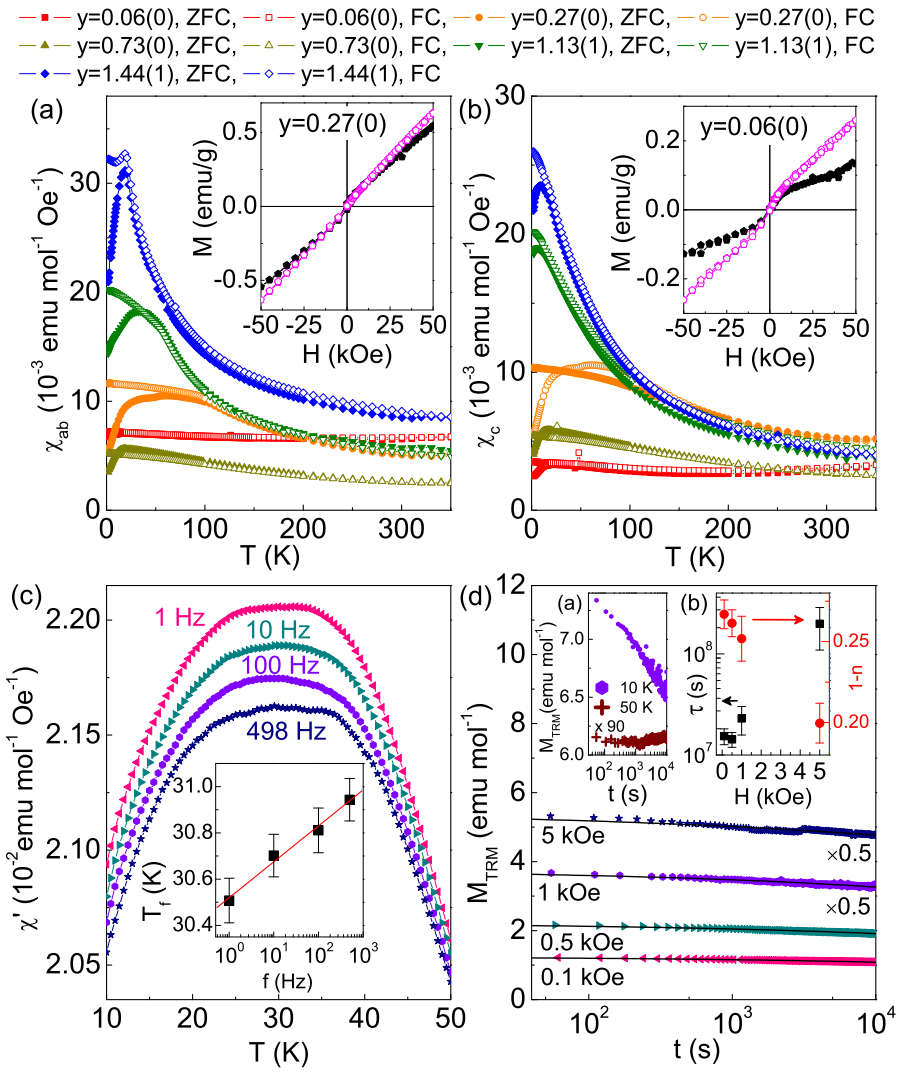

Figure 6.3: Temperature dependence of dc magnetic susceptibilities for $K_xFe_{2-\delta-y}Ni_ySe_2$ series for (a) H⊥c and for (b) H∥c at H=1 kOe in ZFC and FC. Inset figures of (a) and (b) are M-H loops for H⊥c and H∥c, respectively at 1.8 K (filled pentagon) and 300 K (open pentagon). (c) Temperature dependence of $\chi'(T)$ measured at several fixed frequencies for y=1.13(1) of $K_xFe_{2-\delta-y}Ni_ySe_2$. Inset is the frequency dependence of T_f with the linear fitting (solid line). (d) TRM versus time for y=1.13(1) of $K_xFe_{2-\delta-y}Ni_ySe_2$ at 10 K and $t_w = 100s$ with different dc field with fitting (solid lines). Inset (a) is M_{TRM} vs. t at 10 K and 50 K at H = 1 kOe and $t_w = 100s$. Inset (b) is H-field dependence $\tau(s)$ (filled square) and 1-n (filled circle).

at T = 50 K (above T_f), $M_{TRM}(t)$ decays rapidly in a short time and stays nearly constant, when compared to the data at T = 10 K as shown in Fig. 6.3 (d) inset (a). $M_{TRM}(t)$ decay in spin glass system is commonly explained by stretched exponential function, $M_{TRM}(t) = M_0 exp[-(t/\tau)^{1-n}]$, where M_0, τ, and 1-n are the glassy component, the relaxation characteristic time, and the critical exponent, respectively. We observe that τ is significantly increased while 1-n is slightly decreased in magnetic field (Fig. 6.3 (d) inset (b)). The value of 1-n is close to 1/3, as expected for a magnetic spin glass [127, 128].

According to symmetry considerations one can expect four Raman-active phonons for the $I4/mmm$ phase (A_{1g}, B_{1g} and $2E_g$) [129]. However, ordering of the vacancies, as reported for the $K_xFe_{2-\delta}Se_2$ [44], locally reduces the symmetry to $I4/m$. This leads to substantial increase in the number of Raman modes. Symmetry analysis predicts total of 27 Raman modes ($9A_g$, $9B_g$ and $9E_g$) originating from the vibrations within the $I4/m$ phase. When Raman spectra are measured from the *ab* plane of the sample, only two Raman modes can be seen for the $I4/mmm$ phase (A_{1g}+B_{1g}) and 18 for the $I4/m$ phase ($9A_g$+$9B_g$).

Fig. 6.4 (a) shows Raman scattering spectra measured at 100 K from the *ab* plane of $K_xFe_{2-\delta-y}Ni_ySe_2$ single crystal series. For the high concentration of Ni (y =1.44(1)) only two modes can be observed. These modes were previously assigned as A_{1g} (185 cm^{-1}) and B_{1g} (141 cm^{-1}) modes. We notice traces of an additional structure around 248 cm^{-1} for the $y = 1.13(1)$ crystal. The structure is present for all investigated samples $y \leq 1.13(1)$ but it is highly pronounced for the $y = 0.73(0)$ and $y = 0.27(0)$ samples. The origin of this structure is most likely related to crystalline disorder. Disorder breaks the

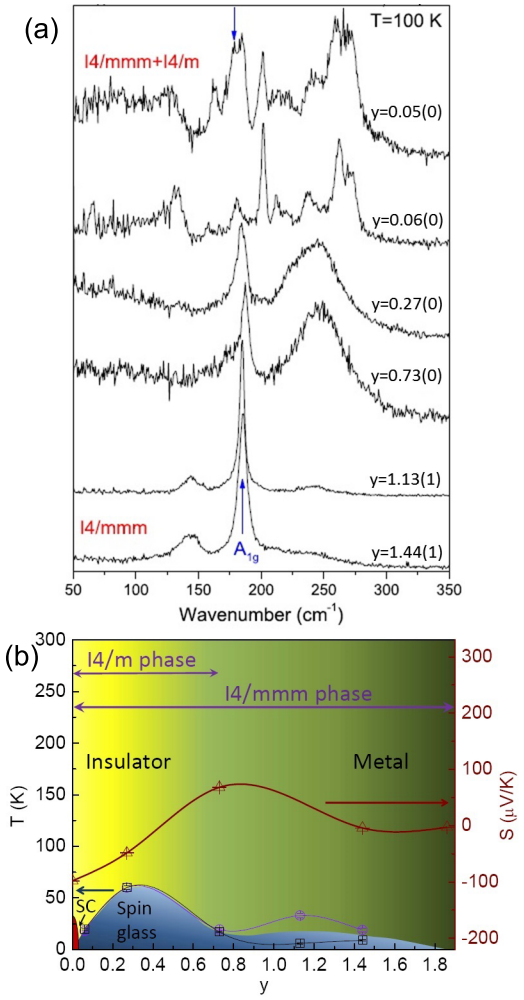

Figure 6.4: (a) Raman scattering spectra of $K_xFe_{2-\delta-y}Ni_ySe_2$ single crystal series measured from the *ab* plane at 100 K. (b) Magnetic, transport, and structural phase diagram. The purple circles are H⊥c and the black squares are for H||c, respectively.

conservation of the momentum during the Raman scattering process enabling contributions of finite wavevector phonons to Raman spectra. Another possibility is an appearance of new high symmetry phase. However this finding is not supported by XRD measurements. For the low concentrations of Ni the structure at around 248 cm^{-1} vanishes and the large number of vibrations of the $I4/m$ phase are observed, suggesting vibrations from vacancy ordered domains in the crystal. The A_{1g} mode (marked by arrow in Fig. 6.4 (a)), which represent the vibration of selenium ions in the $I4/mmm$ phase, persist for all Ni concentrations. This shows the presence of the $I4/mmm$ phase in all samples.

Our main results are summarized on Fig. 6.4 (b) phase diagram. As shown in the lower left corner of the phase diagram, superconducting (SC) phase disappears rapidly by y=0.06(1). The $I4/mmm$ space group is found for all $K_xFe_{2-\delta-y}Ni_ySe_2$ series whereas crystalline disordered $I4/m$ space group persists up to $y = 0.73$. Hence, Fe-based high temperature superconductivity in $K_xFe_{2-\delta-y}Ni_ySe_2$ does vanish before crystalline superstructure of Fe vacancies (crystalline ordered $I4/m$ phase) disappears when y is increased from 0. We note that in high pressure studies superconductivity vanishes simultaneously with $I4/m$ superstructure peak [130]. High degree of crystalline disorder in $I4/mmm$ and in $I4/m$ phase results in insulating or bad metal magnetic glass state that borders superconducting region, similar to copper oxides [131, 132]. In the insulating region of $K_xFe_{2-\delta-y}Ni_ySe_2$ single crystal alloys ground state phase diagram (Fig. 6.4 (b)), freezing temperatures T_f of the magnetic spin glass are higher ($\sim$ 60 K) when compared to metallic regions ($\sim$ 20 K) (y>1.13(1)).

The mechanism of the nonmetallic states in proximity to $K_xFe_{2-\delta}Se_2$ is of the great importance for the understanding of superconductivity [133, 134]. Intimate nanoscale mix of superconducting and insulating magnetic regions may also add states at interfaces [71, 135]. This makes interpretation of many, and in particular bulk measurements difficult. In $K_xFe_{2-\delta}Se_2$ nanoscale phase separation is found below $T_s = 560$ K [136], hence majority of conductivity changes at temperature below T_s should come from the metallic regions. This is supported by recent angle-resolved photoemission results where orbital-selective Mott transition in $K_xFe_{2-\delta}Se_2$ was observed above 150 K [94]. This temperature corresponds to metal - insulator crossover in bulk measurements, suggesting that conductivity changes in bulk measurements may not be simply due to the ratio of metallic and insulating regions in the crystal [1, 93]. Though only metallic nanoscale regions contribute to thermopower and metallic heat capacity (Fig. 6.2 (b,c)), the absolute values of resistivity and magnetization reflect the contribution of both ($I4/mmm$) and insulating parts of the crystal ($I4/m$). Assuming that Ni substitutes Fe in both space group, small Ni substitution therefore is likely to have strong effect on states associated with itinerant d_{xz}/d_{yz} orbitals, perhaps via localization effect in an orbital-selective Mott localization scenario [137, 138]. Further Ni substitution and disorder might enhance conductivity by raising chemical potential and enlarging electron pockets [139–141]. This is in agreement with our phase diagram.

6.4 Conclusion

We have investigated transport, magnetic and structure changes in $K_xFe_{2-\delta-y}Ni_ySe_2$ single crystal series. Small amount of Ni doping $y = 0.06$ suppressed Fe-based high temperature superconductivity. The suppression of superconductivity is more sensitive to Ni substitution than crystalline superstructure of Fe vacancies. Further Ni substitution results in insulating and bad metal magnetic spin glass ground state. However, when Ni concentration in the lattice is higher than Fe, metallic ground state with relatively large density of states at the Fermi level emerges. Similar to copper oxides, insulating/bad metal spin glass is found in proximity to superconducting state. However, in Ni substituted in $K_xFe_{2-\delta}Se_2$ the spin glass state covers nearly all y values, from superconductivity up to the paramagnetic metal $K_xNi_{2-\delta}Se_2$.

Chapter 7

Spin glass behavior in semiconducting $K_{1.03(3)}Fe_{1.05(4)}Ag_{0.88(5)}Te_{2.00(4)}$ single crystals

7.1 Introduction

Recently, new family of iron-based superconductors $A_xFe_{2-y}Se_2$ (A = K, Rb, Cs, and Tl) has been intensively studied after the first discovery in 2010 [1, 142–144]. Unlike other iron-based superconductors which have both hole and electron Fermi surfaces, the hole Fermi surfaces are absent for $A_xFe_{2-y}Se_2$, indicating pairing symmetry other than s± [37, 145–147]. Also, antiferromagnetic order is present around T_N = 560 K induced by the vacancies in the Fe plane that order around T = 580 K [136].

Chemical substitution can introduce various type of changes such as changing the local environment of FeSe tetrahedra, producing extra carriers, inducing vacancies, or decreasing dimensionality of conducting bands. These changes influence the magnetic and transport properties. For instance, $K_xFe_{2-y}S_2$ is a semiconductor with spin-glass transition while $KFe_{0.85}Ag_{1.15}Te_2$ is a semiconductor with antiferromagnetic transition [64, 148]. Moreover, in $K_xFe_{2-y}Se_2$, the existence of superconductivity is controlled by vacancies [121].

In this work, we have investigated $K_{1.03(3)}Fe_{1.05(4)}Ag_{0.88(5)}Te_{2.00(4)}$ single crystals. The structure, transport, and magnetic properties of this single crystal indicate that it shows semiconducting behavior with spin glass property below ∼53 K.

7.2 Experiment

Single crystals of $K_{1.03(3)}Fe_{1.05(4)}Ag_{0.88(5)}Te_{2.00(4)}$ were synthesized by a self-fulx method with nominal composition $KFe_{1.25}Ag_{0.75}Te_2$. Prereacted $Fe_{1.25}Ag_{0.75}Te_2$ and K pieces (Purity 99.999%, Alfa Aesar) were placed in the alumina crucible and sealed with quartz tube under partial pressure of argon. Sealed tube was heated up to 1030°C, kept at this temperature for 3 h, and slowly cooled down to 730°C with a rate of 5°C/h. Single crystals with typical size $2 \times 2 \times 0.5$ mm^3 were grown. Powder x-ray diffraction (XRD) spectra were taken with Cu K_α radiation ($\lambda = 0.15418$ nm) by a Rigaku Miniflex X-ray machine. The lattice parameters were obtained by refining XRD spectra using the Rietica software [58]. The element analysis was performed using an

energy-dispersive x-ray spectroscopy (EDX) in JOEL LSM-6500 scanning electron microscope. Room temperature Fe-57 Mossbauer spectra were measured on a constant-acceleration spectrometer using a rhodium matrix Co-57 source. The spectrometer was calibrated at 295 K with a 10 μm α-Fe foil and isomer shifts reported are relative to α-Fe. Magnetization measurements, electrical transport, and heat capacity were carried out in Quantum Design MPMS-XL5 and PPMS-9. The in-plane resistivity $\rho_{ab}(T)$ was measured by a four-probe configuration on cleaved rectangular shape single crystals.

7.3 Results and Discussion

Fig. 7.1 (a) shows powder XRD results the structural refinement of $K_{1.03(3)}Fe_{1.05(4)}Ag_{0.88(5)}Te_{2.00(4}$ can be fitted by I4/mmm space group. The refined lattice parameters are a = 4.336(2) $\mathring{A}$ and c = 15.019(2) $\mathring{A}$. The value of a axis parameter is smaller while c axis lattice parameter is larger when compared to $K_{1.00(3)}Fe_{0.85(2)}Ag_{1.15(2)}Te_{2.00(1)}$ (a = 4.371(2) $\mathring{A}$ and c = 14.954(2) $\mathring{A}$) [148]. Also, both lattice parameters are smaller than the lattice parameter of $CsFe_xAg_{2-x}Te_2$ [149], while larger than those of $K_xFe_{2-y}Se_2$ and $K_xFe_{2-y}S_2$ [1, 120], since ionic size of K^+ is smaller than that of Cs^+, and ionic size of Ag^+ and Te^{2-} are larger than ionic size of Fe^{2+} and $Se^{2-}(S^{2-})$. EDX spectrum of single crystals shown on Fig. 7.1 (b) proves the existence of K, Fe, Ag, and Te. The average stoichiometry was determined by EDX for several single crystals with multiple measuring points denote that the crystals are homogeneous and the determined stoichiometries are K:Fe:Ag:Te=1.03(3):1.05(4):0.88(5):2.00(4) when fixing Se

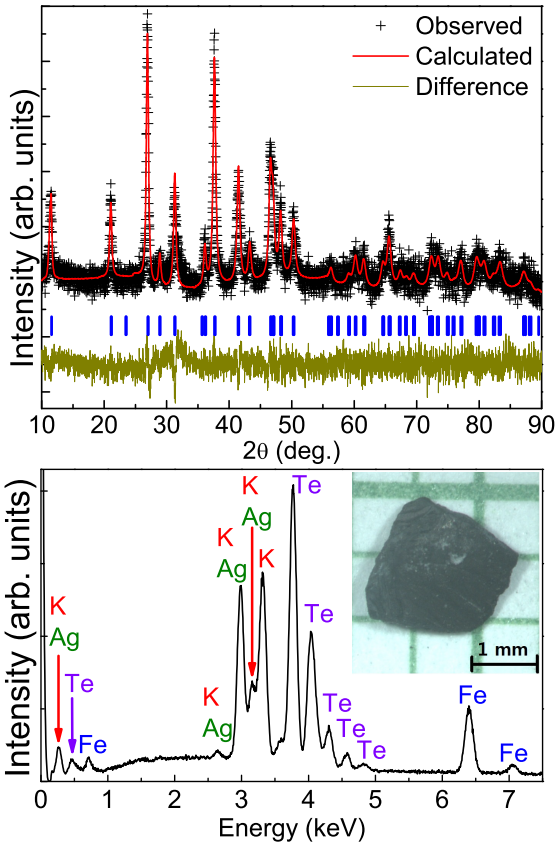

Figure 7.1: (a) Powder XRD patterns of $K_{1.03(3)}Fe_{1.05(4)}Ag_{0.88(5)}Te_{2.00(4)}$. (b) The EDX spectrum of $K_{1.03(3)}Fe_{1.05(4)}Ag_{0.88(5)}Te_{2.00(4)}$. The inset shows a photo of typical single crystal of $K_{1.03(3)}Fe_{1.05(4)}Ag_{0.88(5)}Te_{2.00(4)}$.

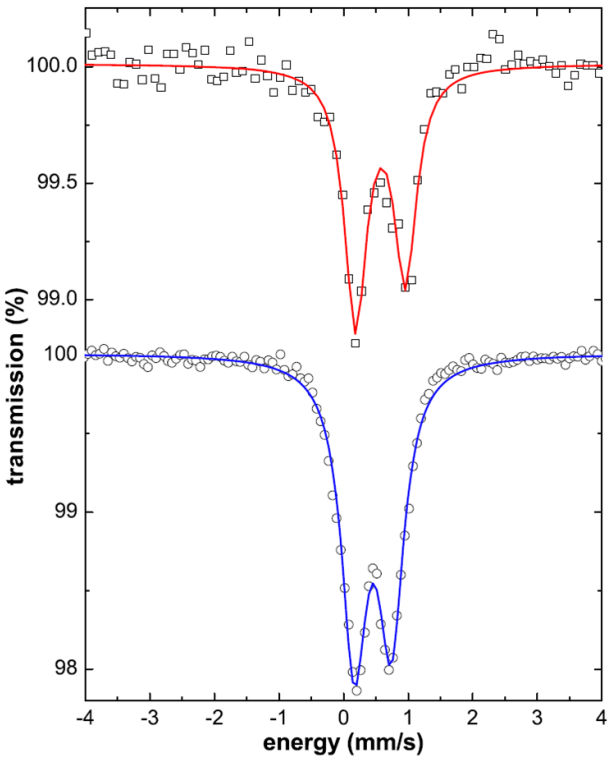

Figure 7.2: Mössbauer spectrum of $K_{1.03(3)}Fe_{1.05(4)}Ag_{0.88(5)}Te_{2.00(4)}$ (open squares) and $K_{1.00(3)}Fe_{0.85(2)}Ag_{1.15(2)}Te_{2.00(1)}$ (open circles) at room temperature.

stoichiometry to be 2. This compound shows vacancies on Fe/Ag whereas $K_{1.00(3)}Fe_{0.85(2)}Ag_{1.15(2)}Te_{2.00(1)}$ does not show any vacancies which implies different magnetic ground state between these two crystals [64].

Room temperature Mössbauer spectra of both $K_{1.03(3)}Fe_{1.05(4)}Ag_{0.88(5)}Te_{2.00(4)}$ and $K_{1.00(3)}Fe_{0.85(2)}Ag_{1.15(2)}Te_{2.00(1)}$ exhibit a doublet and are shown in Fig. 7.2. The unequal line intensities are due to preferred grain orientation in the powderized samples, as was verified by a measurement at a different angle, which yields different relative intensities. The spectral parameters are summarized in Table 7.1.

Table 7.1: Isomer shift relative to α-Fe δ, quadruple splitting ΔE_Q, and linewidth Γ for $K_{1.03(3)}Fe_{1.05(4)}Ag_{0.88(5)}Te_{2.00(4)}$ and $K_{1.00(3)}Fe_{0.85(2)}Ag_{1.15(2)}Te_{2.00(1)}$.

	δ (nm/s)	ΔE_Q (nm/s)	Γ (nm/s)
$K_{1.03(3)}Fe_{1.05(4)}Ag_{0.88(5)}Te_{2.00(4)}$	0.572(6)	0.771(11)	0.414(16)
$K_{1.00(3)}Fe_{0.85(2)}Ag_{1.15(2)}Te_{2.00(1)}$	0.451(3)	0.573(4)	0.476(6)

The isomer shifts are slightly higher than those reported for metallic $ThCr_2Si_2$ type compounds [150, 151], but still confirm the divalent nature of Fe in these cases. The large linewidth as compared to 0.25 mm/s obtained for the α-Fe calibrant foil is an indication of distribution of spectral parameters. No secondary Fe species could be detected.

Temperature dependence of the in-plane resistivity of $K_{1.03(3)}Fe_{1.05(4)}Ag_{0.88(5)}Te_{2.00(4)}$ single crystal shown on Fig. 7.3. As temperature decreases, $\rho_{ab}(T)$ increases with shoulder appearing around 140 K which is shifted to a little higher temperature compared to $K_{1.00(3)}Fe_{0.85(2)}Ag_{1.15(2)}Te_{2.00(1)}$ [148]. The room temperature $\rho_{ab}(T)$ is around 1 Ωcm which is similar to $K_{1.00(3)}Fe_{0.85(2)}Ag_{1.15(2)}Te_{2.00(1)}$ and about one order of magnitude smaller than $K_xFe_{2-y}Se_2$ and $K_xFe_{2-y}S_2$ [120, 148]. $\rho_{ab}(T)$ at high temperature can be fitted by thermal activation model $\rho = \rho_0 exp(E_a/k_BT)$, where ρ_0 is a prefactor, E_a is an activation energy, and k_B is Boltzmann's constant (Inset (a) of Fig. 7.3). The obtained values from the fitting are $\rho_0 = 0.19(2)$ Ωcm which is larger than the value of $K_xFe_{2-y}Se_2$ and $K_xFe_{2-y}S_2$ and $E_a = 43(2)$ meV in temperature range above 200 K which is smaller than the values of $K_xFe_{2-y}Se_2$ and $K_xFe_{2-y}S_2$ [64, 148]. $K_{1.03(3)}Fe_{1.05(4)}Ag_{0.88(5)}Te_{2.00(4)}$ single crystal shows large MR (Inset of Fig. 7.3 (b)) especially below 140 K where the shoulder appears similar to $K_{1.00(3)}Fe_{0.85(2)}Ag_{1.15(2)}Te_{2.00(1)}$ [64].

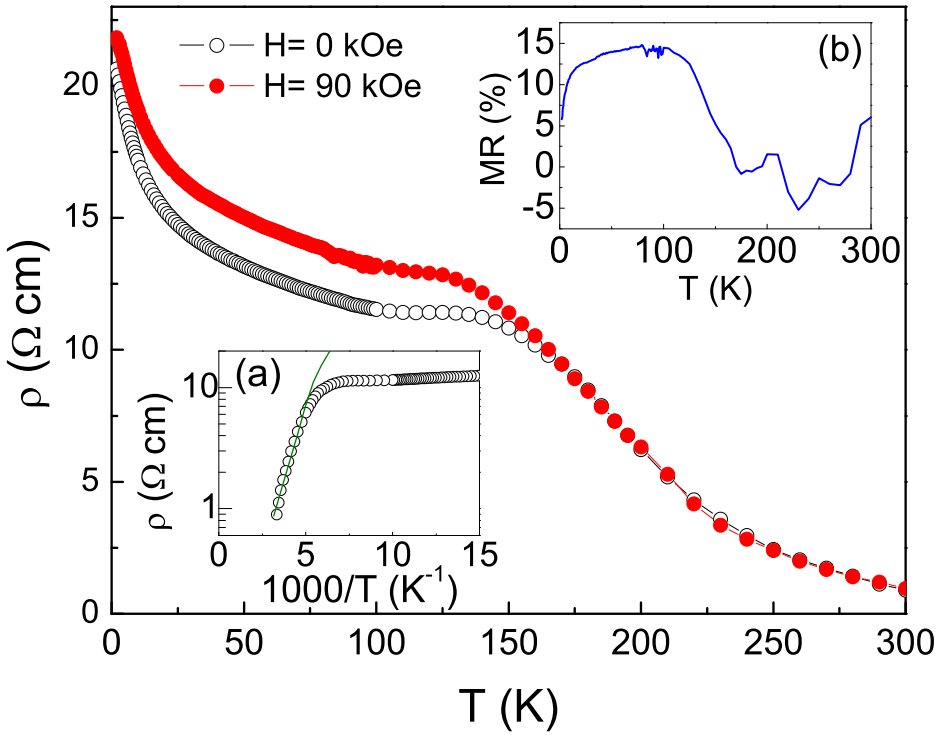

Figure 7.3: Temperature dependence of the in-plane resistivity of $K_{1.03(3)}Fe_{1.05(4)}Ag_{0.88(5)}Te_{2.00(4)}$ with H = 0 kOe (open black circle) and 90 kOe (closed red circle) for H||c direction. Inset (a) exhibits thermal activation model fitting (green solid line) for $\rho_{ab}(T)$ at H= 0 kOe. Inset (b) shows temperature dependence magnetoresistance.

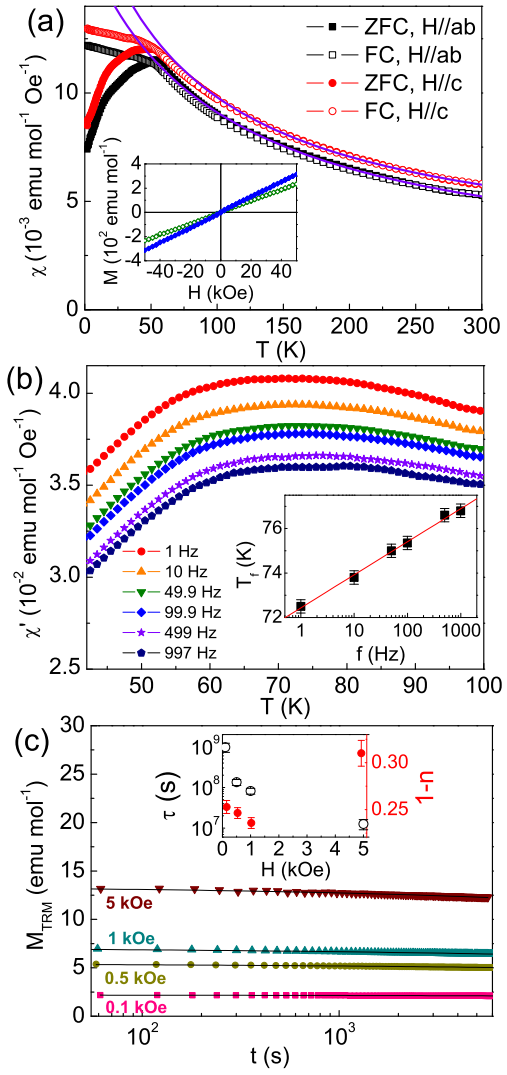

Figure 7.4: Temperature dependence of dc magnetic susceptibilities for $K_{1.03(3)}Fe_{1.05(4)}Ag_{0.88(5)}Te_{2.00(4)}$ single crystal for H$\|$ab and H$\|$c at H=1 kOe in ZFC and FC. The solid lines are Curie-Weiss fitting. Inset figure of (a) is M-H loops for H$\|$ab at 1.8 K (filled diamond) and 300 K (open diamond). (b) Temperature dependence of $\chi'(T)$ measured at several fixed frequencies for $K_{1.03(3)}Fe_{1.05(4)}Ag_{0.88(5)}Te_{2.00(4)}$. Inset is the frequency dependence of T_f with the linear fitting (solid line). (c) Temperature dependence thermoremanent magnetization (TRM) for $K_{1.03(3)}Fe_{1.05(4)}Ag_{0.88(5)}Te_{2.00(4)}$ at 10 K and $t_w = 100s$ with different dc field with fitting (solid lines). Inset is H-field dependence $\tau(s)$ (open circles) and 1-n (filled circles).

Magnetic susceptibility with H||c is slightly larger than H||ab as shown on Fig. 7.4 (a). Both follow Curie-Weiss law $\chi(T) = \chi_0 + C/(T-\theta)$, where χ_0 includes core diamagnetism, van Vleck and Pauli paramagnetism, C is the Curie constant, and θ is the Curie-Weiss temperature. The obtained values are χ_0 = 1.4(2)× 10^{-3} emu mol^{-1} Oe^{-1}, C = 1.55(9) emu mol^{-1} Oe^{-1} K, and θ = -100(9) K for H||ab, and χ_0 = 2.1(1)× 10^{-3} emu mol^{-1} Oe^{-1}, C = 1.38(7) emu mol^{-1} Oe^{-1} K, and θ = -80(7) K for H||c. The effective moment obtained from the above values are $\mu_{eff} = 1.57(2)\mu_B$/Fe for H||ab and $\mu_{eff} = 1.50(4)\mu_B$/Fe for H||c which is smaller than for free Fe^{2+} ions in $K_{1.00(3)}Fe_{0.85(2)}Ag_{1.15(2)}Te_{2.00(1)}$ [64]. The irreversible behavior of $\chi(T)$ below 53 K implies ferromagnetic contribution or glassy transition. Similar behavior has been reported in $KFeCuS_2$, KFe_2Se_2, and $TlFe_{2-x}Se_2$ [124, 125, 148]. The magnetization loop is linear at 300 K while it is slightly curved like s-shape at 1.8 K which is typical behavior of spin glass system [124].

As frequency increases, the peak of real part of the magnetic susceptibility $\chi'(T)$ shift to the higher temperature while the magnitude of $\chi'(T)$ decreases implying typical behavior of spin glass [126]. The frequency dependence peak position (T_f) shown on Fig. 7.4 (b) is fitted by $K=\Delta T_f/(T_f \Delta \log f)$, and the obtained K value is 0.0201(2). This is in agreement with the values ($0.0045 \leq K \leq 0.08$) for a canonical spin glass [126]. Fig. 7.4 (c) shows thermoremanent magnetization (TRM). The sample was cooled down from 100 K (above T_f) to 10 K (below T_f) in different magnetic fields, and kept there for $t_w = 100s$. Then, magnetic field turned off and magnetization decay $M_{TRM}(t)$ was measured. At T = 10 K, $M_{TRM}(t)$ shows slow decay, so $M_{TRM}(t)$ has non-zero values even after several hours which denotes another

typical property of magnetic spin glass [126]. This behaviors are fitted by stretched exponential function, $M_{TRM}(t) = M_0 exp[-(t/\tau)^{1-n}]$, where M_0, τ, and 1-n are the glassy component, the relaxation characteristic time, and the critical exponent, respectively. The obtained τ is deceases up to 1 kOe and increase suddenly at 5 kOe, whereas 1-n value keeps decreasing as H increases (Inset of Fig. 7.4.) The attained 1-n value is around 1/3, which is consistent value with the typical spin glass system [127, 128]. This spin glass behavior could be interpreted by magnetic cluster due to the Fe vacancies and disorder similar to $TlFe_{2-x}Se_2$ when x≥0.3 and KFe_2S_2 [120, 124]. This opinion is also supported by the fact that $K_{1.00(3)}Fe_{0.85(2)}Ag_{1.15(2)}Te_{2.00(1)}$ single crystal show antiferromagnetic behavior since it does not have any vacancies [148].

Fig. 7.5 shows the temperature dependence of heat capacity measured from T = 1.9 K to T = 300 K in zero magnetic field which approaches the Dulong-Petit value of 3NR = 150 (J/mol K) at high temperature. N is the atomic number and R is the gas constant. Low temperature heat capacity is fitted by $C/T=\gamma_{SG}+\beta T^2$ (inset (a) of Fig. 7.5) which provides values of $\gamma_{SG} = 0.88(6)$ mJ mol^{-1} K^{-2} and $\beta = 3.20(5)$ mJ mol^{-1} K^{-4}. The Debye temperature can be estimated by $\Theta_D = (12\pi^4 NR/5\beta)^{1/3}$, where N is the atomic number in the chemical formula and R is the gas constant which results in $\Theta_D = 144.9(5)$ K. This is almost same as the estimate Θ_D of $K_{1.00(3)}Fe_{0.85(2)}Ag_{1.15(2)}Te_{2.00(1)}$ single crystal and much smaller than Θ_D of $K_xFe_{2-y}Se_2$ and $K_xFe_{2-y}S_2$ possibly due to the larger atomic mass of Ag and Te.

Compared to $K_{1.00(3)}Fe_{0.85(2)}Ag_{1.15(2)}Te_{2.00(1)}$, $K_{1.03(3)}Fe_{1.05(4)}Ag_{0.88(5)}Te_{2.00(4)}$ shows more than twice larger room temperature resistivity. This might be due to the increased disorder by the vacancies of Fe and Ag sites [148]. Both single

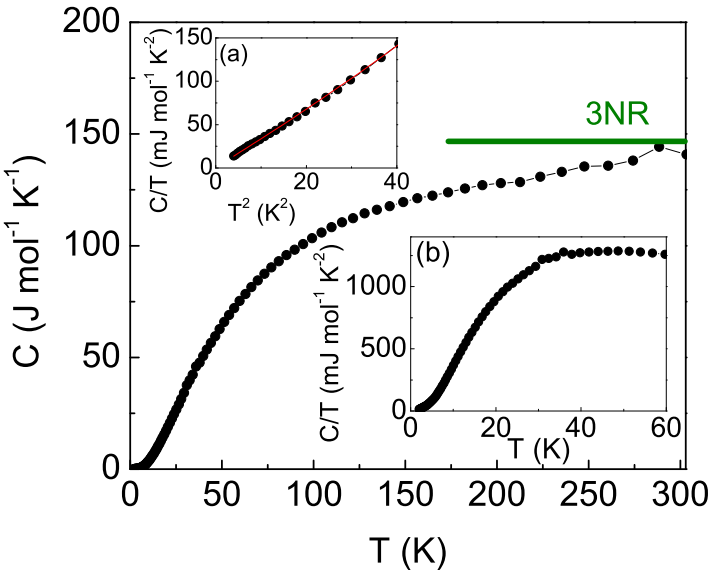

Figure 7.5: Temperature dependence of specific heat for $K_{1.03(3)}Fe_{1.05(4)}Ag_{0.88(5)}Te_{2.00(4)}$ single crystal. Inset (a) shows the relation between C/T and T^2 at low temperature. The solid line represent fits by the equation $C/T=\gamma_{SG}+\beta T^2$. Inset (b) shows C/T vs. T relation at low temperature.

crystals follows Curie-Weiss law above ∼50 K and Curie-Weiss temperatures are very similar to each other. Also, both show magnetic transition around similar temperature (∼32 K for $K_{1.00(3)}Fe_{0.85(2)}Ag_{1.15(2)}Te_{2.00(1)}$ and ∼53 K for $K_{1.03(3)}Fe_{1.05(4)}Ag_{0.88(5)}Te_{2.00(4)}$). However, $K_{1.00(3)}Fe_{0.85(2)}Ag_{1.15(2)}Te_{2.00(1)}$ exhibits long range antiferromagnetic order while $K_{1.03(3)}Fe_{1.05(4)}Ag_{0.88(5)}Te_{2.00(4)}$ shows spin glasslike behavior. The lattice constant a of $K_{1.03(3)}Fe_{1.05(4)}Ag_{0.88(5)}Te_{2.00(4)}$ is smaller than $K_{1.00(3)}Fe_{0.85(2)}Ag_{1.15(2)}Te_{2.00(1)}$ while the case of the lattice constant c is vice versa. This implies the unit cells become elongated along c-axis and Fe plane is contracted which can cause glassy behavior. $ACuFeS_2$ (A=Cs, Rb, K) compounds also behave like spin-glass which indicates the distribution of Ag in $K_{1.03(3)}Fe_{1.05(4)}Ag_{0.88(5)}Te_{2.00(4)}$ might be similar to Cu in $ACuFeS_2$ (A=Cs, Rb, K) [125].

7.4 Conclusion

We have investigated $K_{1.03(3)}Fe_{1.05(4)}Ag_{0.88(5)}Te_{2.00(4)}$ single crystal. Composition and structure analysis implies the existence of vacancies which causes the difference between $K_{1.03(3)}Fe_{1.05(4)}Ag_{0.88(5)}Te_{2.00(4)}$ and $K_{1.00(3)}Fe_{0.85(2)}Ag_{1.15(2)}Te_{2.00(1)}$. Semiconducting behavior with positive magnetoresistance and spin glass behavior below ∼53 K was observed by transport and magnetic measurement.

Chapter 8

Conclusion

In this dissertation, we discussed phase separation and neighboring ground states of superconductivity in $K_xFe_{2-y}Se_2$ single crystal. Iron-based superconductor $K_xFe_{2-y}Se_2$ has generated considerable attention having higher critical temperature ($\sim$ 31 K) than previously reported FeSe series ($\sim$ 8 K). It also shows a unique real space phase separation with Fe vacancy order.

We found by SEM measurement $K_xFe_{2-y}Se_2$ single crystal shows two different phases which are separated spatially. Superconducting granular phases are embedded in insulating AFM matrix phases. Magnetic moment of $K_xFe_{2-y}Se_2$ single crystal was significantly enhanced by applying post annealing and fast quenching process which implying the increasing of the insulating AFM matrix phase which has higher magnetic moment after the post annealing and fast quenching. In addition, static disorder of $K_{0.50}Na_{0.24}Fe_{2-y}Se_2$ decreased after the post annealing and fast quenching. This indicates the overall phases are more ordered when they change into many pieces and rearrange to make the well connected network by the post annealing and fast quenching process.

We investigated the effect of the chemical substitution and report various insulating ground states, for example superconductor-insulator transition (SIT) in high-magnetic field by substitution of Na on $K_xFe_{2-y}Se_2$ and magnetic spin glass by substituting Ni or Ag and Te on $K_xFe_{2-y}Se_2$ single crystal.

The normal state in-plane resistivity below T_c and the upper critical field $\mu_0 H_{c2}(T)$ for $K_{0.50}Na_{0.24}Fe_{2-y}Se_2$ are measured by suppressing superconductivity in pulsed magnetic fields. The normal-state resistivity ρ_{ab} is found to increase logarithmically as $T/T_c \to 0$ with decreasing temperature similar to granular superconductors and Cu-based high-T_c superconductors. Our results suggest that SIT may be induced by the granularity in inhomogeneous superconductors, which is related to the intrinsic real space phase separation.

We also present a ground state change of $K_xFe_{2-\delta-y}Ni_ySe_2$ ($0.06 \leq y \leq 1.44$) single crystal compound. Small amount of Ni ($\sim 4\%$) substitution suppresses superconductivity below 1.8 K and for higher Ni content insulating spin glass magnetic ground state is induced. Also, $K_{1.03(3)}Fe_{1.05(4)}Ag_{0.88(5)}Te_{2.00(4)}$ single crystal shows insulating spin glass behavior. The similar phenomena occurs in cuprate superconductors indicating the spin glass is found in proximity to superconducting state in all known high-T_c superconductors.

Bibliography

[1] Jiangang Guo, Shifeng Jin, Gang Wang, Shunchong Wang, Kaixing Zhu, Tingting Zhou, Meng He, and Xiaolong Chen. Superconductivity in the iron selenide $K_xFe_2Se_2$ ($0 \leq x \leq 1.0$). *Physical Review B*, 82(18):180520, 2010.

[2] Hiroyuki Shibata. Superconducting single-photon detectors. *NTT Technical Review*, 9:9, 2011.

[3] Hideo Hosono. Layered Iron Pnictide Supercondctors: discovery and current status. *J. Phys. Soc. Jpn. Suppl. C*, 77:1, 2008.

[4] Wei Bao, Guan-Nan Li, Qing-Zhen Huang, Gen-Fu Chen, Jun-Bao He, Du-Ming Wang, M. A. Green, Yi-Ming Qiu, Jian-Lin Luo, and Mei-Mei Wu. Superconductivity tuned by the iron vacancy order in $K_xFe_{2-y}Se_2$. *Chinese Physics Letters*, 30(2):027402, 2013.

[5] F. Chen, M. Xu, Q. Q. Ge, Y. Zhang, Z. R. Ye, L. X. Yang, Juan Jiang, B. P. Xie, R. C. Che, M. Zhang, A. F. Wang, X. H. Chen, D. W. Shen, J. P. Hu, and D. L. Feng. Electronic identification of the parental phases and mesoscopic phase separation of $K_xFe_{2-y}Se_2$ superconductors. *Physical Review X*, 1(2):021020, 2011.

[6] Xiaxin Ding, Delong Fang, Zhenyu Wang, Huan Yang, Jianzhong Liu, Qiang Deng, Guobin Ma, Chong Meng, Yuhui Hu, and Hai-Hu Wen. Influence of microstructure on superconductivity in $K_xFe_{2-y}Se_2$ and evidence for a new parent phase $K_2Fe_7Se_8$. *Nat Commun*, 4:1897, 2013.

[7] Z. Wang, Y. J. Song, H. L. Shi, Z. W. Wang, Z. Chen, H. F. Tian, G. F. Chen, J. G. Guo, H. X. Yang, and J. Q. Li. Microstructure and ordering of iron vacancies in the superconductor system $K_yFe_xSe_2$ as seen via transmission electron microscopy. *Physical Review B*, 83(14): 140505, 2011.

[8] Wikipedia. Meissner effect. 2014. URL http://en.wikipedia.org/wiki/Meissner_effect. [Online; accessed 27-August-2014].

[9] Wikipedia. Magnetisation and superconductors. 2008. URL http://commons.wikimedia.org/wiki/File:Magnetisation_and_superconductors.png. [Online; accessed 22-May-2008].

[10] Quantum Design. *Physical Property Measurement System: Heat Capacity Option User's Manual*, 2010.

[11] Mike McElfresh. Fundamentals of magnetism and magnetic measurements. *Quantum Design*, 1994.

[12] N. Xu. Spectroscopic and solution chemistry studies of cobalt (ii) absorption mechanisms at the calcite-water interface. *Ph.D. Dissertation, Stanford University*, 1993.

[13] H Kamerlingh Onnes. The resistance of pure mercury at helium temperatures. *Commun. Phys. Lab. Univ. Leiden*, 12:120, 1911.

[14] J.P. Carbotte F. Marsiglio. Electron - phonon superconductivity. *arXiv:cond-mat/0106143*, 2001.

[15] J. G. Bednorz and K. A. Müller. Possible high T_c superconductivity in the Ba-La-Cu-O system. *Z. Phys. B*, 64 (2):189, 1986.

[16] M. K. Wu, J. R. Ashburn, C. J. Torng, P. H. Hor, R. L. Meng, L. Gao, Z. J. Huang, Y. Q. Wang, and C. W. Chu. Superconductivity at 93 K in a new mixed-phase Y-Ba-Cu-O compound system at ambient pressure. *Physical Review Letters*, 58(9):908–910, 1987.

[17] Maeda Hiroshi, Tanaka Yoshiaki, Fukutomi Masao, and Asano Toshihisa. A new high- T_c oxide superconductor without a rare earth element. *Japanese Journal of Applied Physics*, 27(2A):L209, 1988.

[18] Z. Z. Sheng and A. M. Hermann. Bulk superconductivity at 120 K in the Tl-Ca/Ba-Cu-O system. *Nature*, 332(6160):138–139, 1988.

[19] J.D. Guo A. Schilling, M. Cantoni and H. R. Ott. Superconductivity above 130 K in the Hg-Ba-Ca-C-O system. *Nature*, 363:56, 1993.

[20] P. Dai, B. C. Chakoumakos, G. F. Sun, K. W. Wong, Y. Xin, and D. F. Lu. Synthesis and neutron powder diffraction study of the superconductor $HgBa_2Ca_2Cu_3O_{8+\delta}$ by Tl substitution. *Physica C: Superconductivity*, 243(3-4):201–206, 1995.

[21] L. Gao, Y. Y. Xue, F. Chen, Q. Xiong, R. L. Meng, D. Ramirez, C. W. Chu, J. H. Eggert, and H. K. Mao. Superconductivity up to 164 K in $HgBa_2Ca_{m-1}Cu_mO_{2m+2+\delta}$ under quasihydrostatic pressures. *Physical Review B*, 50(6):4260–4263, 1994.

[22] Yoichi Kamihara, Takumi Watanabe, Masahiro Hirano, and Hideo Hosono. Iron-based layered superconductor $La[O_{1-x}F_x]FeAs$ (x = 0.05-0.12) with T_c = 26 K. *Journal of the American Chemical Society*, 130(11):3296–3297, 2008.

[23] B. S. Chandrasekhar and J. K. Hulm. The electrical resistivity and super-conductivity of some uranium alloys and compounds. *Journal of Physics and Chemistry of Solids*, 7(2-3):259–267, 1958.

[24] Hans F. Braun. Superconductivity of rare earth-iron silicides. *Physics Letters A*, 75(5):386–388, 1980.

[25] Hiroki Takahashi, Kazumi Igawa, Kazunobu Arii, Yoichi Kamihara, Masahiro Hirano, and Hideo Hosono. Superconductivity at 43 K in an iron-based layered compound $LaO_{1-x}F_xFeAs$. *Nature*, 453(7193):376–378, 2008.

[26] Gen-Fu Chen, Zheng Li, Gang Li, Wan-Zheng Hu, Jing Dong, Jun Zhou, Xiao-Dong Zhang, Ping Zheng, Nan-Lin Wang, and Jian-Lin Luo. Superconductivity in hole-doped $(Sr_{1-x}K_x)Fe_2As_2$. *Chinese Physics Letters*, 25(9):3403, 2008.

[27] Z. A. Ren, J. Yang, W. Lu, W. Yi, G. C. Che, X. L. Dong, L. L. Sun, and Z. X. Zhao. Superconductivity at 52 K in iron based f doped layered quaternary compound $Pr[O_{1-x}F_x]FeAs$. *Materials Research Innovations*, 12(3):105–106, 2008.

[28] Marianne Rotter, Marcus Tegel, and Dirk Johrendt. Superconductivity at 38 K in the iron arsenide $(Ba_{1-x}K_x)Fe_2As_2$. *Physical Review Letters*, 101(10):107006, 2008.

[29] X. C. Wang, Q. Q. Liu, Y. X. Lv, W. B. Gao, L. X. Yang, R. C. Yu, F. Y. Li, and C. Q. Jin. The superconductivity at 18 K in LiFeAs system. *Solid State Communications*, 148(11-12):538–540, 2008.

[30] R. Mittal, Y. Su, S. Rols, M. Tegel, S. L. Chaplot, H. Schober, T. Chatterji, D. Johrendt, and Th Brueckel. Phonon dynamics in $Sr_{0.6}K_{0.4}Fe_2As_2$ and $Ca_{0.6}Na_{0.4}Fe_2As_2$ from neutron scattering and lattice-dynamical calculations. *Physical Review B*, 78(22):224518, 2008.

[31] Raquel Cortes-Gil and Simon J. Clarke. Structure, magnetism, and superconductivity of the layered iron arsenides $Sr_{1-x}Na_xFe_2As_2$. *Chemistry of Materials*, 23(4):1009–1016, 2011.

[32] Fong-Chi Hsu, Jiu-Yong Luo, Kuo-Wei Yeh, Ta-Kun Chen, Tzu-Wen Huang, Phillip M. Wu, Yong-Chi Lee, Yi-Lin Huang, Yan-Yi Chu, Der-Chung Yan, and Maw-Kuen Wu. Superconductivity in the PbO-type structure α-FeSe. *Proceedings of the National Academy of Sciences*, 105 (38):14262–14264, 2008.

[33] S. Medvedev, T. M. McQueen, I. A. Troyan, T. Palasyuk, M. I. Eremets, R. J. Cava, S. Naghavi, F. Casper, V. Ksenofontov, G. Wortmann, and C. Felser. Electronic and magnetic phase diagram of β-$Fe_{1.01}Se$ with superconductivity at 36.7 K under pressure. *Nat Mater*, 8(8):630–633, 2009.

[34] Rongwei Hu, Emil S. Bozin, J. B. Warren, and C. Petrovic. Superconductivity, magnetism, and stoichiometry of single crystals of $Fe_{1+y}(Te_{1-x}S_x)_z$. *Phys. Rev. B*, 80:214514, 2009.

[35] Yoshikazu Mizuguchi, Fumiaki Tomioka, Shunsuke Tsuda, Takahide Yamaguchi, and Yoshihiko Takano. Superconductivity in S-substituted FeTe. *Applied Physics Letters*, 94(1):012503, 2009.

[36] B. C. Sales, A. S. Sefat, M. A. McGuire, R. Y. Jin, D. Mandrus, and Y. Mozharivskyj. Bulk superconductivity at 14 k in single crystals of $Fe_{1+y}Te_xSe_{1-x}$. *Phys. Rev. B*, 79:094521, 2009.

[37] I. I. Mazin, D. J. Singh, M. D. Johannes, and M. H. Du. Unconventional superconductivity with a sign reversal in the order parameter of $LaFeAsO_{1-x}F_x$. *Physical Review Letters*, 101(5):057003, 2008.

[38] Kazuhiko Kuroki, Seiichiro Onari, Ryotaro Arita, Hidetomo Usui, Yukio Tanaka, Hiroshi Kontani, and Hideo Aoki. Unconventional pairing originating from the disconnected Fermi surfaces of superconducting $LaFeAsO_{1-x}F_x$. *Physical Review Letters*, 101(8):087004, 2008.

[39] Yoshikazu Mizuguchi, Hiroyuki Takeya, Yasuna Kawasaki, Toshinori Ozaki, Shunsuke Tsuda, Takahide Yamaguchi, and Yoshihiko Takano. Transport properties of the new Fe-based superconductor $K_xFe_2Se_2$(T_c=33 K). *Applied Physics Letters*, 98(4):042511, 2011.

[40] R. H. Liu, X. G. Luo, M. Zhang, A. F. Wang, J. J. Ying, X. F. Wang, Y. J. Yan, Z. J. Xiang, P. Cheng, G. J. Ye, Z. Y. Li, and X. H. Chen. Coexistence of superconductivity and antiferromagnetism in single crystals $A_{0.8}Fe_{2-y}Se_2$ (A=K, Rb, Cs, Tl/K and Tl/Rb): Evidence from magnetization and resistivity. *EPL (Europhysics Letters)*, 94(2):27008, 2011.

[41] Z. Shermadini, A. Krzton-Maziopa, M. Bendele, R. Khasanov, H. Luetkens, K. Conder, E. Pomjakushina, S. Weyeneth, V. Pomjakushin, O. Bossen, and A. Amato. Coexistence of magnetism and superconductivity in the iron-based compound $Cs_{0.8}(FeSe_{0.98})_2$. *Physical Review Letters*, 106(11):117602, 2011.

[42] Z. Shermadini, H. Luetkens, R. Khasanov, A. Krzton-Maziopa, K. Conder, E. Pomjakushina, H. H. Klauss, and A. Amato. Superconducting properties of single-crystalline $A_xFe_{2-y}Se_2$ studied using muon spin spectroscopy. *Physical Review B*, 85(10):100501, 2012.

[43] J. Maletz, V. B. Zabolotnyy, D. V. Evtushinsky, A. N. Yaresko, A. A. Kordyuk, Z. Shermadini, H. Luetkens, K. Sedlak, R. Khasanov, A. Amato, A. Krzton-Maziopa, K. Conder, E. Pomjakushina, H. H. Klauss, E. D. L. Rienks, B. Büchner, and S. V. Borisenko. Photoemission and muon spin relaxation spectroscopy of the iron-based $Rb_{0.77}Fe_{1.61}Se_2$ superconductor: Crucial role of the cigar-shaped Fermi surface. *Physical Review B*, 88(13):134501, 2013.

[44] N. Lazarević, M. Abeykoon, P. W. Stephens, Hechang Lei, E. S. Bozin, C. Petrovic, and Z. V. Popović. Vacancy-induced nanoscale phase separation in $K_xFe_{2-y}Se_2$ single crystals evidenced by raman scattering and powder x-ray diffraction. *Physical Review B*, 86(5):054503, 2012.

[45] A. M. Zhang, K. Liu, J. H. Xiao, J. B. He, D. M. Wang, G. F. Chen, B. Normand, and Q. M. Zhang. Vacancy ordering and phonon spectrum of the iron-based superconductor $K_{0.8}Fe_{1.6}Se_2$. *Physical Review B*, 85(2): 024518, 2012.

[46] A. M. Zhang, J. H. Xiao, Y. S. Li, J. B. He, D. M. Wang, G. F. Chen, B. Normand, Q. M. Zhang, and T. Xiang. Two-magnon raman scattering in $A_{0.8}Fe_{1.6}Se_2$ systems (A = K, Rb, Cs, and Tl): Competition between superconductivity and antiferromagnetic order. *Physical Review B*, 85 (21):214508, 2012.

[47] B. Shen, B. Zeng, G. F. Chen, J. B. He, D. M. Wang, H. Yang, and H. H. Wen. Intrinsic percolative superconductivity in $K_xFe_{2-y}Se_2$ single crystals. *EPL (Europhysics Letters)*, 96(3):37010, 2011.

[48] Zhi-Wei Wang, Zhen Wang, Yuan-Jun Song, Chao Ma, Yao Cai, Zhen Chen, Huan-Fang Tian, Huai-Xin Yang, Gen-Fu Chen, and Jian-Qi Li. Structural phase separation in $K_{0.8}Fe_{1.6+x}Se_2$ superconductors. *The Journal of Physical Chemistry C*, 116(33):17847–17852, 2012.

[49] W. Meissner and R. Ochsenfeld. Ein neuer effekt bei eintritt der supraleitfähigkeit. *Naturwissenschaften*, 21:787, 1933.

[50] V. L. Ginzburg and L. D. Landau. On the theory of superconductivity. *Zh. Eksp. Teor. Fiz.*, 20:1064, 1950.

[51] V. V. Schmidt. The physics of superconductors. *Springer*, 1997.

[52] L. Pitaevskii. Superconductivity: Conventional and unconventional superconductors. *Springer*, 1, 2008.

[53] L. N. Cooper. Bound electron pairs in a degenerate Fermi gas. *Phys. Rev.*, 104:1189, 1956.

[54] P. J. Hirschfeld S. Graser, T. A. Maier and D. J. Scalapino. Near-degeneracy of several pairing channels in multiorbital models for the Fe pnictides. *New J. Phys.*, 11:025016, 2009.

[55] Ying Ran Ashvin Vishwanath Fa Wang, Hui Zhai and Dung-Hai Lee. Functional renormalization-group study of the pairing symmetry and pairing mechanism of the FeAs-based high-temperature superconductor. *Phys. Rev. Lett.*, 102:047005, 2009.

[56] P. C. Canfield and Z. Fisk. Growth of single crystals from metallic fluxes. *Phil. Magaz. B*, 65:1117, 1992.

[57] Z. Fisk and J. P. Remeika. Handbook on the physics and chemistry of rare earths. *Elsevier, Amsterdam*, 12, 1989.

[58] B. Hunter. International union of crystallography commission on powder diffraction newsletter. *http://www.rietica.org*, 20, 1998.

[59] Jih Shang Hwang, Kai Jan Lin, and Cheng Tien. Measurement of heat capacity by fitting the whole temperature response of a heat-pulse calorimeter. *Review of Scientific Instruments*, 68(1):94–101, 1997.

[60] E. A. Stern. Theory of the extended x-ray-absorption fine structure. *Phys. Rev. B*, 10:3027, 1974.

[61] B. Ravel and M. Newville. ATHENA, ARTEMIS, HEPHAESTUS: data analysis for x-ray absorption spectroscopy using IFEFFIT. *Journal of Synchrotron Radiation*, 12(4):537–541, 2005.

[62] Fei Han, Huan Yang, Bing Shen, Zhen-Yu Wang, Chun-Hong Li, and Hai-Hu Wen. Metastable superconducting state in quenched $K_xFe_{2-y}Se_2$. *Philosophical Magazine*, 92(19-21):2553–2562, 2012.

[63] Hechang Lei and C. Petrovic. Anisotropy in transport and magnetic properties of $K_{0.64}Fe_{1.44}Se_2$. *Physical Review B*, 83(18):184504, 2011.

[64] Hechang Lei, Milinda Abeykoon, Emil S. Bozin, Kefeng Wang, J. B. Warren, and C. Petrovic. Phase diagram of $K_xFe_{2-y}Se_{2-z}S_z$ and the suppression of its superconducting state by an Fe2-Se/S tetrahedron distortion. *Physical Review Letters*, 107(13):137002, 2011.

[65] R. Prins and D. C. Koningsberg. X-ray absorption: Principles, applications, techniques of EXAFS, SEXAFS, XANES. *Wiley, New York*, 1988.

[66] B. Joseph, A. Iadecola, L. Malavasi, and N. L. Saini. Temperature-dependent local structure of $NdFeAsO_{1-x}F_x$ system using arsenic K-edge extended x-ray absorption fine structure. *Journal of Physics: Condensed Matter*, 23(26):265701, 2011.

[67] P. Zavalij, Wei Bao, X. F. Wang, J. J. Ying, X. H. Chen, D. M. Wang, J. B. He, X. Q. Wang, G. F. Chen, P. Y. Hsieh, Q. Huang, and M. A. Green. Structure of vacancy-ordered single-crystalline superconducting potassium iron selenide. *Physical Review B*, 83(13):132509, 2011.

[68] Shin-Ming Huang, Chung-Yu Mou, and Ting-Kuo Lee. Intrinsic high-temperature superconductivity in ternary iron selenides. *Physical Review B*, 88(17):174510, 2013.

[69] A. Ricci, N. Poccia, G. Campi, B. Joseph, G. Arrighetti, L. Barba, M. Reynolds, M. Burghammer, H. Takeya, Y. Mizuguchi, Y. Takano, M. Colapietro, N. L. Saini, and A. Bianconi. Nanoscale phase separation in the iron chalcogenide superconductor $K_{0.8}Fe_{1.6}Se_2$ as seen via scanning nanofocused x-ray diffraction. *Physical Review B*, 84(6):060511, 2011.

[70] Ricci Alessandro, Poccia Nicola, Joseph Boby, Arrighetti Gianmichele, Barba Luisa, Plaisier Jasper, Campi Gaetano, Mizuguchi Yoshikazu, Takeya Hiroyuki, Takano Yoshihiko, Saini Naurang Lal, and Bianconi Antonio. Intrinsic phase separation in superconducting $K_{0.8}Fe_{1.6}Se_2$ (T_c

= 31.8 K) single crystals. *Superconductor Science and Technology*, 24 (8):082002, 2011.

[71] Y. J. Yan, M. Zhang, A. F. Wang, J. J. Ying, Z. Y. Li, W. Qin, X. G. Luo, J. Q. Li, Jiangping Hu, and X. H. Chen. Electronic and magnetic phase diagram in $K_xFe_{2-y}Se_2$ superconductors. *Sci. Rep.*, 2, 2012.

[72] Y. J. Song, Z. Wang, Z. W. Wang, H. L. Shi, Z. Chen, H. F. Tian, G. F. Chen, H. X. Yang, and J. Q. Li. Phase transition, superstructure and physical properties of $K_2Fe_4Se_5$. *EPL (Europhysics Letters)*, 95(3): 37007, 2011.

[73] Hechang Lei, Rongwei Hu, E. S. Choi, J. B. Warren, and C. Petrovic. Pauli-limited upper critical field of $Fe_{1+y}Te_{1-x}Se_x$. *Physical Review B*, 81(9):094518, 2010.

[74] Hechang Lei, Rongwei Hu, E. S. Choi, J. B. Warren, and C. Petrovic. Effects of excess Fe on upper critical field and magnetotransport in $Fe_{1+y}(Te_{1-x}Se_x)_z$. *Physical Review B*, 81(18):184522, 2010.

[75] G. Fuchs, S. L. Drechsler, N. Kozlova, G. Behr, A. Köhler, J. Werner, K. Nenkov, R. Klingeler, J. Hamann-Borrero, C. Hess, A. Kondrat, M. Grobosch, A. Narduzzo, M. Knupfer, J. Freudenberger, B. Büchner, and L. Schultz. High-field Pauli-limiting behavior and strongly enhanced upper critical magnetic fields near the transition temperature of an arsenic-deficient $LaO_{0.9}F_{0.1}FeAs_{1-\delta}$ superconductor. *Physical Review Letters*, 101(23):237003, 2008.

[76] Takanori Kida, Takahiro Matsunaga, Masayuki Hagiwara, Yoshikazu Mizuguchi, Yoshihiko Takano, and Koichi Kindo. Upper critical fields of the 11-system iron-chalcogenide superconductor $FeSe_{0.25}Te_{0.75}$. *Journal of the Physical Society of Japan*, 78(11):113701, 2009.

[77] F. Hunte, J. Jaroszynski, A. Gurevich, D. C. Larbalestier, R. Jin, A. S. Sefat, M. A. McGuire, B. C. Sales, D. K. Christen, and D. Mandrus. Two-band superconductivity in $LaFeAsO_{0.89}F_{0.11}$ at very high magnetic fields. *Nature*, 453(7197):903–905, 2008.

[78] J. Jaroszynski, F. Hunte, L. Balicas, Youn-jung Jo, I. Raičević, A. Gurevich, D. C. Larbalestier, F. F. Balakirev, L. Fang, P. Cheng, Y. Jia, and H. H. Wen. Upper critical fields and thermally-activated transport of $NdFeAsO_{0.7}F_{0.3}$ single crystal. *Physical Review B*, 78(17):174523, 2008.

[79] S. A. Baily, Y. Kohama, H. Hiramatsu, B. Maiorov, F. F. Balakirev, M. Hirano, and H. Hosono. Pseudoisotropic upper critical field in cobalt-doped $SrFe_2As_2$ epitaxial films. *Physical Review Letters*, 102(11):117004, 2009.

[80] E. D. Mun, M. M. Altarawneh, C. H. Mielke, V. S. Zapf, R. Hu, S. L. Bud'ko, and P. C. Canfield. Anisotropic H_{c2} of $K_{0.8}Fe_{1.76}Se_2$ determined up to 60 T. *Physical Review B*, 83(10):100514, 2011.

[81] Yoichi Ando, G. S. Boebinger, A. Passner, Tsuyoshi Kimura, and Kohji Kishio. Logarithmic divergence of both in-plane and out-of-plane normal-state resistivities of superconducting $La_{2-x}Sr_xCuO_4$ in the zero-temperature limit. *Physical Review Letters*, 75(25):4662–4665, 1995.

[82] G. S. Boebinger, Yoichi Ando, A. Passner, T. Kimura, M. Okuya, J. Shimoyama, K. Kishio, K. Tamasaku, N. Ichikawa, and S. Uchida. Insulator-to-metal crossover in the normal state of $La_{2-x}Sr_xCuO_4$ near optimum doping. *Physical Review Letters*, 77(27):5417–5420, 1996.

[83] S. Ono, Yoichi Ando, T. Murayama, F. F. Balakirev, J. B. Betts, and G. S. Boebinger. Metal-to-insulator crossover in the low-temperature normal state of $Bi_2Sr_{2-x}La_xCuO_{6+\delta}$. *Physical Review Letters*, 85(3): 638–641, 2000.

[84] Hechang Lei and C. Petrovic. Giant increase in critical current density of $K_xFe_{2-y}Se_2$ single crystals. *Physical Review B*, 84(21):212502, 2011.

[85] Hyejin Ryu, Hechang Lei, A. I. Frenkel, and C. Petrovic. Local structural disorder and superconductivity in $K_xFe_{2-y}Se_2$. *Physical Review B*, 85 (22):224515, 2012.

[86] D. H. Ryan, W. N. Rowan-Weetaluktuk, J. M. Cadogan, R. Hu, W. E. Straszheim, S. L. Bud'ko, and P. C. Canfield. ^{57}Fe Mössbauer study of magnetic ordering in superconducting $K_{0.80}Fe_{1.76}Se_{2.00}$ single crystals. *Physical Review B*, 83(10):104526, 2011.

[87] Y. Liu, Q. Xing, K. W. Dennis, R. W. McCallum, and T. A. Lograsso. Evolution of precipitate morphology during heat treatment and its implications for the superconductivity in $K_xFe_{1.6+y}Se_2$ single crystals. *Physical Review B*, 86(14):144507, 2012.

[88] Wei Li, Hao Ding, Peng Deng, Kai Chang, Canli Song, Ke He, Lili Wang, Xucun Ma, Jiang-Ping Hu, Xi Chen, and Qi-Kun Xue. Phase separation

and magnetic order in K-doped iron selenide superconductor. *Nat Phys*, 8(2):126–130, 2012.

[89] T. P. Ying, X. L. Chen, G. Wang, S. F. Jin, T. T. Zhou, X. F. Lai, H. Zhang, and W. Y. Wang. Observation of superconductivity at 30∼46K in $A_xFe_2Se_2$ (A = Li, Na, Ba, Sr, Ca, Yb, and Eu). *Sci. Rep.*, 2, 2012.

[90] Hechang Lei and C. Petrovic. Anisotropy of upper critical fields and thermally-activated flux flow of quenched $K_xFe_{2-y}Se_2$ single crystals. *arXiv:1110.5316*, 2011.

[91] C. P. Bean. Magnetization of hard superconductors. *Physical Review Letters*, 8(6):250–253, 1962.

[92] E. M. Gyorgy, R. B. van Dover, K. A. Jackson, L. F. Schneemeyer, and J. V. Waszczak. Anisotropic critical currents in $Ba_2YCu_3O_7$ analyzed using an extended bean model. *Applied Physics Letters*, 55(3):283–285, 1989.

[93] Daniel P. Shoemaker, Duck Young Chung, Helmut Claus, Melanie C. Francisco, Sevda Avci, Anna Llobet, and Mercouri G. Kanatzidis. Phase relations in $K_xFe_{2-y}Se_2$ and the structure of superconducting $K_xFe_2Se_2$ via high-resolution synchrotron diffraction. *Physical Review B*, 86(18): 184511, 2012.

[94] M. Yi, D. H. Lu, R. Yu, S. C. Riggs, J. H. Chu, B. Lv, Z. K. Liu, M. Lu, Y. T. Cui, M. Hashimoto, S. K. Mo, Z. Hussain, C. W. Chu, I. R. Fisher, Q. Si, and Z. X. Shen. Observation of temperature-induced crossover to an orbital-selective mott phase in $A_xFe_{2-y}Se_2$ (A=K, Rb) superconductors. *Physical Review Letters*, 110(6):067003, 2013.

[95] N. R. Werthamer, E. Helfand, and P. C. Hohenberg. Temperature and purity dependence of the superconducting critical field, H_{c2}. iii. electron spin and spin-orbit effects. *Physical Review*, 147(1):295–302, 1966.

[96] T. P. Orlando, E. J. McNiff, S. Foner, and M. R. Beasley. Critical fields, Pauli paramagnetic limiting, and material parameters of Nb_3Sn and V_3Si. *Physical Review B*, 19(9):4545–4561, 1979.

[97] P. B. Allen. Handbook of superconductivity. *Academic Press, New York*, page 478, 1999.

[98] A. Gurevich. Enhancement of the upper critical field by nonmagnetic impurities in dirty two-gap superconductors. *Physical Review B*, 67(18): 184515, 2003.

[99] H. Q. Yuan, J. Singleton, F. F. Balakirev, S. A. Baily, G. F. Chen, J. L. Luo, and N. L. Wang. Nearly isotropic superconductivity in (Ba,K)Fe_2As_2. *Nature*, 457(7229):565–568, 2009.

[100] N. F. Mott. Conduction in non-crystalline materials. *Philosophical Magazine*, 19(160):835–852, 1969.

[101] E. Abrahams, P. W. Anderson, D. C. Licciardello, and T. V. Ramakrishnan. Scaling theory of localization: Absence of quantum diffusion in two dimensions. *Physical Review Letters*, 42(10):673–676, 1979.

[102] Khmel'nitskii D.E. Gor'kov L.P., Larkin A.I. Particle conductivity in a two-dimensional random potential. *JETP Lett.*, 30:228, 1979.

[103] F. Gantmakher Vsevolod and T. Dolgopolov Valery. Superconductor-insulator quantum phase transition. *Physics-Uspekhi*, 53(1):1, 2010.

[104] I. S. Beloborodov, A. V. Lopatin, V. M. Vinokur, and K. B. Efetov. Granular electronic systems. *Reviews of Modern Physics*, 79(2):469–518, 2007.

[105] Myron Strongin, R. S. Thompson, O. F. Kammerer, and J. E. Crow. Destruction of superconductivity in disordered near-monolayer films. *Physical Review B*, 1(3):1078–1091, 1970.

[106] Yoseph Imry and Myron Strongin. Destruction of superconductivity in granular and highly disordered metals. *Physical Review B*, 24(11):6353–6360, 1981.

[107] K. M. Lang, V. Madhavan, J. E. Hoffman, E. W. Hudson, H. Eisaki, S. Uchida, and J. C. Davis. Imaging the granular structure of high-tc superconductivity in underdoped $Bi_2Sr_2CaCu_2O_{8+\delta}$. *Nature*, 415(6870): 412–416, 2002.

[108] Ilija Zeljkovic, Zhijun Xu, Jinsheng Wen, Genda Gu, Robert S. Markiewicz, and Jennifer E. Hoffman. Imaging the impact of single oxygen atoms on superconducting $Bi_{2+y}Sr_{2-y}CaCu_2O_{8+x}$. *Science*, 337 (6092):320–323, 2012.

[109] Y. Fukuzumi, K. Mizuhashi, K. Takenaka, and S. Uchida. Universal superconductor-insulator transition and T_c depression in zn-substituted high- T_c cuprates in the underdoped regime. *Physical Review Letters*, 76(4):684–687, 1996.

[110] V. J. Emery, S. A. Kivelson, and O. Zachar. Spin-gap proximity effect mechanism of high-temperature superconductivity. *Physical Review B*, 56(10):6120–6147, 1997.

[111] A. Leithe-Jasper, W. Schnelle, C. Geibel, and H. Rosner. Superconducting state in $SrFe_{2-x}Co_xAs_2$ by internal doping of the iron arsenide layers. *Physical Review Letters*, 101(20):207004, 2008.

[112] Athena S. Sefat, Ashfia Huq, Michael A. McGuire, Rongying Jin, Brian C. Sales, David Mandrus, Lachlan M. D. Cranswick, Peter W. Stephens, and Kevin H. Stone. Superconductivity in $LaFe_{1-x}Co_xAsO$. *Physical Review B*, 78(10):104505, 2008.

[113] Satoru Matsuishi, Yasunori Inoue, Takatoshi Nomura, Hiroshi Yanagi, Masahiro Hirano, and Hideo Hosono. Superconductivity induced by co-doping in quaternary fluoroarsenide CaFeAsF. *Journal of the American Chemical Society*, 130(44):14428–14429, 2008.

[114] Athena S. Sefat, Rongying Jin, Michael A. McGuire, Brian C. Sales, David J. Singh, and David Mandrus. Superconductivity at 22 K in Co-doped $BaFe_2As_2$ crystals. *Physical Review Letters*, 101(11):117004, 2008.

[115] L. J. Li, Y. K. Luo, Q. B. Wang, H. Chen, Z. Ren, Q. Tao, Y. K. Li, X. Lin, M. He, Z. W. Zhu, G. H. Cao, and Z. A. Xu. Superconductivity induced by ni doping in $BaFe_2As_2$ single crystals. *New Journal of Physics*, 11(2):025008, 2009.

[116] Lei Hechang, Abeykoon Milinda, Wang Kefeng, S. Bozin Emil, Ryu Hyejin, D. Graf, J. B. Warren, and C. Petrovic. Physical properties of $K_xNi_{2-y}Se_2$ single crystals. *Journal of Physics: Condensed Matter*, 26 (1):015701, 2014.

[117] A. P. Hammersley, S. O. Svensson, M. Hanfland, A. N. Fitch, and D. Hausermann. Two-dimensional detector software: From real detector to idealised image or two-theta scan. *High Pressure Research*, 14(4-6): 235–248, 1996.

[118] A.C. Larson and R.B. Von Dreele. General structure analysis system. *Los Alamos National Laboratory, Report No. LAUR*, 86:748, 1994.

[119] Brian Toby. EXPGUI, a graphical user interface for GSAS. *Journal of Applied Crystallography*, 34(2):210–213, 2001.

[120] Hechang Lei, Milinda Abeykoon, Emil S. Bozin, and C. Petrovic. Spin-glass behavior of semiconducting $K_xFe_{2-y}S_2$. *Physical Review B*, 83(18): 180503, 2011.

[121] D. M. Wang, J. B. He, T. L. Xia, and G. F. Chen. Effect of varying iron content on the transport properties of the potassium-intercalated iron selenide $K_xFe_{2-y}Se_2$. *Physical Review B*, 83(13):132502, 2011.

[122] James R. Neilson, Anna Llobet, Andreas V. Stier, Liang Wu, Jiajia Wen, Jing Tao, Yimei Zhu, Zlatko B. Tesanovic, N. P. Armitage, and Tyrel M. McQueen. Mixed-valence-driven heavy-fermion behavior and superconductivity in KNi_2Se_2. *Physical Review B*, 86(5):054512, 2012.

[123] Kefeng Wang, Hechang Lei, and C. Petrovic. Thermoelectric studies of $K_xFe_{2-y}Se_2$ indicating a weakly correlated superconductor. *Physical Review B*, 83(17):174503, 2011.

[124] J. J. Ying, A. F. Wang, Z. J. Xiang, X. G. Luo, R. H. Liu, X. F. Wang, Y. J. Yan, M. Zhang, G. J. Ye, P. Cheng, and X. H. Chen. Reentrant spin-glass behavior in $TlFe_{2-x}Se_2$ with the $ThCr_2Si_2$-type structure. *arXiv:1012.2929*, 2010.

[125] M. Oledzka, K. V. Ramanujachary, and M. Greenblatt. Physical properties of quaternary mixed transition metal sulfides: $ACuFeS_2$ (A = K, Rb, Cs). *Materials Research Bulletin*, 31(12):1491–1499, 1996.

[126] J. A. Mydosh. *Spin glasses : an experimental introduction.* Taylor & Francis, London; Washington, DC, 1993.

[127] I. A. Campbell. Critical exponents of spin-galss systems. *Physical Review B*, 37(16):9800–9801, 1988.

[128] D. Chu, G. G. Kenning, and R. Orbach. Dynamic measurements in a Heisenberg spin glass: CuMn. *Physical Review Letters*, 72(20):3270–3273, 1994.

[129] N. Lazarević, M. Radonjić, M. Šepanović, Hechang Lei, D. Tanasković, C. Petrovic, and Z. V. Popović. Lattice dynamics of KNi_2Se_2. *Physical Review B*, 87(14):144305, 2013.

[130] Jing Guo, Xiao-Jia Chen, Jianhui Dai, Chao Zhang, Jiangang Guo, Xiaolong Chen, Qi Wu, Dachun Gu, Peiwen Gao, Lihong Yang, Ke Yang, Xi Dai, Ho-kwang Mao, Liling Sun, and Zhongxian Zhao. Pressure-driven quantum criticality in iron-selenide superconductors. *Physical Review Letters*, 108(19):197001, 2012.

[131] I. Raičević, J. Jaroszyński, Dragana Popović, C. Panagopoulos, and T. Sasagawa. Evidence for charge glasslike behavior in lightly doped $La_{2-x}Sr_xCuO_4$ at low temperatures. *Physical Review Letters*, 101(17): 177004, 2008.

[132] Xiaoyan Shi, G. Logvenov, A. T. Bollinger, I. Božović, C. Panagopoulos, and Dragana Popović. Emergence of superconductivity from the dynamically heterogeneous insulating state in $La_{2-x}Sr_xCuO_4$. *Nat Mater*, 12 (1):47–51, 2013.

[133] Z. P. Yin, K. Haule, and G. Kotliar. Kinetic frustration and the nature of the magnetic and paramagnetic states in iron pnictides and iron chalcogenides. *Nat Mater*, 10(12):932–935, 2011.

[134] Pengcheng Dai, Jiangping Hu, and Elbio Dagotto. Magnetism and its microscopic origin in iron-based high-temperature superconductors. *Nat Phys*, 8(10):709–718, 2012.

[135] S. Mukherjee, M. N. Gastiasoro, P. J. Hirschfeld, and B. M. Andersen. Low-energy bound states at interfaces between superconducting and block antiferromagnetic regions in $K_xFe_{2-y}Se_2$. *Physical Review B*, 88(1):014519, 2013.

[136] Wei Bao, Qing-Zhen Huang, Gen-Fu Chen, M. A. Green, Du-Ming Wang, Jun-Bao He, and Yi-Ming Qiu. A novel large moment antiferromagnetic order in $K_{0.8}Fe_{1.6}Se_2$ superconductor. *Chinese Physics Letters*, 28(8):086104, 2011.

[137] Rong Yu and Qimiao Si. Orbital-selective mott phase in multiorbital models for alkaline iron selenides $K_{1-x}Fe_{2-y}Se_2$. *Physical Review Letters*, 110(14):146402, 2013.

[138] Rong Yu, Jian-Xin Zhu, and Qimiao Si. Mott transition in modulated lattices and parent insulator of $(K, Tl)_yFe_xSe_2$ superconductors. *Physical Review Letters*, 106(18):186401, 2011.

[139] Tom Berlijn, P. J. Hirschfeld, and Wei Ku. Effective doping and suppression of Fermi surface reconstruction via fe vacancy disorder in $K_xFe_{2-y}Se_2$. *Physical Review Letters*, 109(14):147003, 2012.

[140] L. Craco, M. S. Laad, and S. Leoni. Unconventional mott transition in $K_xFe_{2-y}Se_2$. *Physical Review B*, 84(22):224520, 2011.

[141] Lu Feng, Zhao Jian Zhou, and Wang Wei-Hua. Electronic structure of the new ni-based superconductor KNi_2Se_2. *Journal of Physics: Condensed Matter*, 24(49):495501, 2012.

[142] A. F. Wang, J. J. Ying, Y. J. Yan, R. H. Liu, X. G. Luo, Z. Y. Li, X. F. Wang, M. Zhang, G. J. Ye, P. Cheng, Z. J. Xiang, and X. H. Chen. Superconductivity at 32 K in single-crystalline $Rb_xFe_{2-y}Se_2$. *Physical Review B*, 83(6):060512, 2011.

[143] A. Krzton-Maziopa, Z. Shermadini, E. Pomjakushina, V. Pomjakushin, M. Bendele, A. Amato, R. Khasanov, H. Luetkens, and K. Conder. Synthesis and crystal growth of $Cs_{0.8}(FeSe_{0.98})_2$: a new iron-based superconductor with $T_c = 27$ K. *Journal of Physics: Condensed Matter*, 23 (5):052203, 2011.

[144] Wang Hang-Dong, Dong Chi-Heng, Li Zu-Juan, Mao Qian-Hui, Zhu Sha-Sha, Feng Chun-Mu, H. Q. Yuan, and Fang Ming-Hu. Superconductivity at 32K and anisotropy in $Tl_{0.58}Rb_{0.42}Fe_{1.72}Se_2$ crystals. *EPL (Europhysics Letters)*, 93(4):47004, 2011.

[145] I. R. Shein and A. L. Ivanovskii. Electronic structure and fermi surface of new K intercalated iron selenide superconductor $K_xFe_2Se_2$. *Physics Letters A*, 375(6):1028–1031, 2011.

[146] Y. Zhang, L. X. Yang, M. Xu, Z. R. Ye, F. Chen, C. He, H. C. Xu, J. Jiang, B. P. Xie, J. J. Ying, X. F. Wang, X. H. Chen, J. P. Hu, M. Matsunami, S. Kimura, and D. L. Feng. Nodeless superconducting gap in $A_xFe_2Se_2$ (A=K,Cs) revealed by angle-resolved photoemission spectroscopy. *Nat Mater*, 10(4):273–277, 2011.

[147] H. Ding, P. Richard, K. Nakayama, K. Sugawara, T. Arakane, Y. Sekiba, A. Takayama, S. Souma, T. Sato, T. Takahashi, Z. Wang, X. Dai, Z. Fang, G. F. Chen, J. L. Luo, and N. L. Wang. Observation of Fermi-surface-dependent nodeless superconducting gaps in $Ba_{0.6}K_{0.4}Fe_2As_2$. *EPL (Europhysics Letters)*, 83(4):47001, 2008.

[148] Hechang Lei, Emil S. Bozin, Kefeng Wang, and C. Petrovic. Antiferromagnetism in semiconducting $KFe_{0.85}Ag_{1.15}Te_2$ single crystals. *Physical Review B*, 84(6):060506, 2011.

[149] Jing Li, Hong-You Guo, Ricardo A. Yglesias, and Thomas J. Emge. $CsFe_xAg_{2-x}Te_2$ (x = 0.72): The first quaternary iron telluride synthesized from molten salt. *Chemistry of Materials*, 7(4):599–601, 1995.

[150] H. Raffius, E. Mörsen, B. D. Mosel, W. Müller-Warmuth, T. Hilbich, M. Reehuis, T. Vomhof, and W. Jeitschko. ^{57}Fe Mössbauer spectroscopy and some complementary measurements of various ternary iron phosphides. *Journal of Physics and Chemistry of Solids*, 52(6):787–795, 1991.

[151] Nowik Israel, Felner Israel, Ni Ni, L. Bud'ko Sergey, and C. Canfield Paul. Mössbauer studies of $Ba(Fe_{1-x}Ni_x)_2As_2$. *Journal of Physics: Condensed Matter*, 22(35):355701, 2010.